

REPORT DOCUMENTATION PAGE				Form Approved OMB No. 0704-0188	
Public reporting burden for this collection of information is estimated to average 1 hour per response, including the time for reviewing instructions, searching existing data sources, gathering and maintaining the data needed, and completing and reviewing this collection of information. Send comments regarding this burden estimate or any other aspect of this collection of information, including suggestions for reducing this burden to Department of Defense, Washington Headquarters Services, Directorate for Information Operations and Reports (0704-0188), 1215 Jefferson Davis Highway, Suite 1204, Arlington, VA 22202-4302. Respondents should be aware that notwithstanding any other provision of law, no person shall be subject to any penalty for failing to comply with a collection of information if it does not display a currently valid OMB control number. PLEASE DO NOT RETURN YOUR FORM TO THE ABOVE ADDRESS.					
1. REPORT DATE (DD-MM-YYYY) 1 July 2015		2. REPORT TYPE Journal Article		3. DATES COVERED (From - To) 2 June 2015 – 1 July 2015	
4. TITLE AND SUBTITLE Rapid Aluminum Nanoparticle Production by Milling in NH ₃ and CH ₃ NH ₂ Atmospheres: An Experimental and Theoretical Study				5a. CONTRACT NUMBER	
				5b. GRANT NUMBER	
				5c. PROGRAM ELEMENT NUMBER	
6. AUTHOR(S) Brandon W. McMahon, Jiang Yu, Jerry A. Boatz, Scott L. Anderson				5d. PROJECT NUMBER	
				5e. TASK NUMBER	
				5f. WORK UNIT NUMBER Q188	
7. PERFORMING ORGANIZATION NAME(S) AND ADDRESS(ES) Air Force Research Laboratory (AFMC) AFRL/RQRP 10 E. Saturn Blvd Edwards AFB, CA 93524-7680				8. PERFORMING ORGANIZATION REPORT NO.	
9. SPONSORING / MONITORING AGENCY NAME(S) AND ADDRESS(ES) Air Force Research Laboratory (AFMC) AFRL/RQR 5 Pollux Drive Edwards AFB, CA 93524-7048				10. SPONSOR/MONITOR'S ACRONYM(S)	
				11. SPONSOR/MONITOR'S REPORT NUMBER(S) AFRL-RQ-ED-JA-2015-253	
12. DISTRIBUTION / AVAILABILITY STATEMENT Approved for public release; distribution unlimited					
13. SUPPLEMENTARY NOTES Journal article published in ACS Applied Materials & Interfaces, 1 July 2015. pp 16101-16116 PA Case Number: #15340; Clearance Date: 6/24/2015 Copyright © 2015 American Chemical Society The U.S. Government is joint author of the work and has the right to use, modify, reproduce, release, perform, display, or disclose the work.					
14. ABSTRACT Ball milling of aluminum in gaseous atmospheres of ammonia and monomethylamine (MMA) was found to produce particles in the 100 nm size range with high efficiency. A combination of mass spectrometry, X-ray photoelectron spectroscopy (XPS), thermogravimetric analysis with mass spectrometric product analysis (TGA-MS), scanning electron microscopy (SEM), infrared spectroscopy, and dynamic light scattering (DLS) was used to study the particles and the chemical interactions responsible for particle production. To help understand the nature of the surface chemistry, high level quantum chemical calculations were performed to predict the structures and energetics for binding and reactions of NH ₃ and MMA on aluminum surfaces. Both NH ₃ and MMA react with aluminum under milling conditions, producing H ₂ and other gaseous products, and leaving the surfaces functionalized. The surface functionalization enhances size reduction by reducing the surface free energy and the tendency toward mechanochemical welding. For both NH ₃ and MMA, the particle cores are metallic aluminum, but the surface chemical properties are quite different. The ammonia-milled particles are capped by an AlN _x O _y H _z layer ~10 nm thick, which passivates the particles. The MMA-milled particles are capped with a thinner passivating layer, such that they are pyrophoric in air and react with N ₂ at elevated temperatures.					
15. SUBJECT TERMS milling; nanoparticle synthesis; aluminum; ammonia; monomethylamine					
16. SECURITY CLASSIFICATION OF:			17. LIMITATION OF ABSTRACT	18. NUMBER OF PAGES	19a. NAME OF RESPONSIBLE PERSON
a. REPORT	b. ABSTRACT	c. THIS PAGE			J. Boatz
Unclassified	Unclassified	Unclassified	SAR	105	19b. TELEPHONE NO (include area code) N/A

**Rapid Aluminum Nanoparticle Production by Milling in NH₃ and CH₃NH₂ Atmospheres:
An Experimental and Theoretical Study**

Brandon W. McMahon,^a Jiang Yu,^a Jerry A. Boatz,^b and Scott L. Anderson^{a*}

^aDepartment of Chemistry, University of Utah, 315 S. 1400 E., Salt Lake City, UT 84112

^b Propellants Branch, Rocket Propulsion Division, Aerospace Systems Directorate, Air Force Research Laboratory, AFMC AFRL/RQRP, 10 East Saturn Boulevard, Edwards AFB, CA 93524

Abstract

Ball milling of aluminum in gaseous atmospheres of ammonia and monomethylamine (MMA) was found to produce nanoparticles with high efficiency. A combination of mass spectrometry, X-ray photoelectron spectroscopy (XPS), thermogravimetric analysis with mass spectrometric product analysis (TGA-MS), scanning electron microscopy (SEM), infrared spectroscopy, and dynamic light scattering (DLS) was used to study the particles and the chemical interactions responsible for particle production. To help understand the nature of the surface chemistry, high level quantum chemical calculations were performed to predict the structures and energetics for binding and reactions of NH₃ and MMA on aluminum surfaces. Both are shown to react with fresh aluminum surfaces generated by fracturing, producing H₂ and other gaseous products, and leaving the surfaces functionalized. The surface functionalization enhances size reduction by reducing the surface free energy and the tendency toward mechanochemical welding. For both NH₃ and MMA, the particle cores are metallic aluminum, but the surface chemical properties are quite different. The ammonia-milled particles are capped by an AlN_xO_yH_z layer several nanometers thick, which passivates the particles. The MMA-milled particles are capped with a thinner passivating layer, such that they are pyrophoric in air and react with N₂ at elevated temperatures.

I. Introduction

Aluminum powder in the micron size range has been extensively used as a high energy density fuel and fuel additive in propulsion and pyrotechnic applications.¹⁻⁵ Reducing the particle size reduces the ignition and combustion times,⁶⁻¹² but the presence of a native oxide layer on the particles means that the oxide becomes a significant portion of the particle mass for particle diameters less than 100 nm.¹⁰ Therefore, methods for production of aluminum nanoparticles capped by a layer that minimizes oxide layer formation during air exposure are potentially useful, particularly if the method is inexpensive and can be scaled to generate quantities needed for practical applications. Here, we present a method, based on ball milling in reactive atmospheres, which generates nanoparticles efficiently, capping them *in situ* with an amine or nitride-like layer. The particles can be further functionalized after production to aid in separation, improve dispersibility in media such as hydrocarbon or other fuels, and improve stability on air exposure.

High energy ball milling typically involves milling feedstock of the material of interest, together with balls or other media of some hard, dense material, such that feedstock particles are crushed during media-media and media-wall collisions. The efficiency of size reduction depends on a number of factors.¹³⁻¹⁷ Brittle materials tend to fracture under mechanical stress, whereas ductile/malleable materials can also undergo plastic deformation. Size reduction by fracturing is counteracted by mechanochemical (cold) welding, which tends to result in particle aggregation and fusion. Production of nanoscale powder results in an enormous increase in surface area, thus one critical factor is the free energy associated with the creation of new surface area. Almost 90 years ago, Rehbinder noted that adsorption of surface-active agents lowers the surface free energy,¹⁸ and as a result, the energy required for crack formation and propagation is lowered, embrittling the material, and enhancing size reduction.¹⁹⁻²⁰ The same effect can reduce the tendency toward particle welding.

Typically, agents used in ball milling are liquids, and can be present either to simply disperse particles, or to bind to, and modify the properties of the particle surfaces. The use of liquid

reagents to enhance reactions and improve the efficiency of mechanochemical syntheses is also a well-established practice.²¹⁻²⁵ We recently reported²⁶ a study of the effects of a variety of liquid reactants and solutions on production of nanoparticles by milling aluminum, iron, and copper, under conditions where no nanoparticles are produced by milling in non-reactive liquids (e.g. hexane). For the two softer metals (Cu and Al), this approach produced mixtures of nano and micron size particles, with nanoparticles making up less than 50% of the product mass under the best conditions. Although it is straightforward to separate the nano and micro particles by sedimentation, it would clearly be better to generate only the desired nanoparticles.

Understanding the mechanism for size reduction in surface-active liquids is complex, because the liquids can affect both mechanical and chemical aspects of the process, lubricating interfaces, dissipating local heating by vaporization, and affecting transport to and from the particle surfaces.

Here we discuss production of aluminum nanoparticles by dry milling in several different gaseous atmospheres. Milling in reactive gases has been investigated in the context of mechanochemical production of hydrogen storage materials.²⁷⁻²⁸ For example, Wang *et al.*²⁹ and Perez *et al.*³⁰ investigated the effects of milling boron in an H₂ atmosphere, and reported substantial hydrogen uptake. Theoretical work by Perez *et al.* suggested that H₂ was dissociatively chemisorbing to the boron surfaces, producing particles with borane-like B-H surface functionality, and the high hydrogen loadings achieved implied that the surface area was large, i.e., the primary particle size was substantially smaller than could be achieved by milling in inert liquids or gases. Furthermore, it was subsequently shown that the H₂-milled particles could be capped and protected against air oxidation by reaction of the B-H bonds with alkenes.³¹ As reported below, milling aluminum in H₂ generates no nanoparticles.

Here, we report a study of nanoparticle production by milling aluminum in gaseous NH₃ and monomethylamine (MMA), which were chosen because amines are known to bind to and react with aluminum surfaces.^{25, 32-37} For example, Davies and Newton³⁸ reported that under ultra-high vacuum conditions, ammonia spontaneously decomposes on aluminum surfaces to form stable

amide and nitride products. As shown below, nanoparticle production is more efficient in these gases than in reactive liquid milling agents, including alkylamines. Furthermore, the particle size distributions are narrower, without the large concentrations of micron scale particles seen for liquid agents. Particles were characterized by a combination of dynamic light scattering, electron microscopy, infrared spectroscopy, and X-ray photoelectron spectroscopy. In addition, chemistry during and after milling was characterized by a combination of mass spectrometry (MS) of the milling atmospheres, thermal desorption MS, and thermogravimetric analysis with MS of the evolved gases (TGA-MS). To help interpret the surface chemistry, detailed density functional theory calculations were carried out, in which atomically rough Al surfaces were modeled using an Al₈₀ cluster that has a variety of surface sites, and is large enough to have a core of bulk-like atoms as well.

II. Experimental and Theoretical Methodology

Particle Production.

Particles were produced by milling aluminum flakes in a Retsch PM 400 planetary ball mill, using Retsch 250 ml tungsten carbide jars, and ~3 mm diameter tungsten carbide milling media. As described previously,²⁶ the original jar lids were replaced with 316 stainless steel lids that have valved ports, which can be used for evacuation, reactant introduction, and headspace sampling, via a vacuum/pressure manifold located inside an N₂-filled glove box.

Approximately 2 g of 1 mm aluminum flakes (Sigma-Aldrich: 518573-500G) and ~200 g of tungsten carbide milling media were added to the jar. The jar was sealed in the glove box, evacuated, and then pumped and backfilled three times with the gas of interest to insure that there was no significant contribution from N₂ to the nitrogen content of the products. For milling in ammonia, the jar was filled to a pressure of ~3.7 atm (~55 psia). Because the vapor pressure of monomethylamine (MMA) is lower, the maximum fill pressure was ~2.2 atm (~32 psia), with some variability from run to run due to the effects of evaporative cooling on the MMA tank pressure. To compensate for the lower initial MMA pressure, the headspace was evacuated and

re-pressurized after each hour of milling. For both gases, the mill was operated with a sun wheel rotational frequency of 350 RPM (relative centrifugal force of ~20 g) for 5 hours.

Safety and Handling Considerations

Unpassivated aluminum nanopowder is violently reactive with oxidizers such as O₂ and H₂O, and spontaneously ignites upon air exposure. Solvent-wetted particles may undergo delayed ignition. Samples were handled and stored in a N₂-filled glove box, however, note that O₂ contamination, even at levels well below 1 ppm, is sufficient to oxidize the sample surface layer in a few seconds, if reaction is efficient. Samples were stored inside sealed vials in the glove box, to minimize exposure to contaminants. To passivate particles under controlled conditions, we simply exposed a thin layer of the Al nanopowder to the glove box atmosphere for a few hours, resulting in passivation to the point where the particles no longer would ignite spontaneously when brought into contact with air.

Particle Analysis

Scanning electron microscopy (SEM) was done using an FEI Nova Nano 600 instrument. Samples were prepared by ultrasonication in acetonitrile and diluting until only slightly turbid, followed by drop casting on lacey carbon transmission electron microscopy (TEM) grids. Dynamic light scattering (DLS) analyses were performed using a NICOMP 380 ZLS instrument to analyze samples dispersed in acetonitrile, and diluted until only slightly turbid. Samples prepared with NH₃ or MMA milling were somewhat prone to aggregation, and suspensions were only stable for 15 – 30 minutes. To minimize aggregation, the DLS samples were ultrasonicated just prior to analysis.

A Kratos Axis Ultra instrument was used for X-ray photoelectron spectroscopy (XPS), using monochromatic Al K α radiation (1486.6 eV), and 300 x 700 micron analysis area. Sample charging was compensated using a low energy electron flood gun. The NH₃-milled samples were prepared for XPS by pressing the powders directly onto carbon tape on a stainless steel sample holder. For both samples, transfers from the glove box to the XPS instrument were made using a

Kratos inert atmosphere transfer device, however, for the much more reactive MMA sample, the device was modified to allow the internal volume to be evacuated, leak-checked, and pressurized with 99.9999% argon to minimize air intrusion in case of leaks. As noted above, however, even samples handled and transferred in “inert” atmospheres inevitably received significant oxygen exposures.

Mass spectrometry was used to analyze the headspace of the milling jars at intervals during the milling process, in order to probe reactions of NH_3 or CH_3NH_2 with aluminum under milling conditions. For gas sampling, jars were transferred into the glove box and connected to the vacuum/pressure manifold, which was used to leak a small amount of headspace gas into a sampling vial. The sampling vial was then connected to the inlet of a quadrupole mass spectrometer, with a base pressure below 5×10^{-9} Torr. Gases were leaked into the mass spectrometer at a source pressure of $\sim 1 \times 10^{-7}$ Torr.

Thermogravimetric analysis (TGA) was used to determine the mass loss from samples during heating from 25 °C to 800 °C at a rate of 10 °C /min. The TA Model Q500 Thermogravimetric Analyzer is housed in an N_2 -filled glove box so that samples were not exposed to air during transfer to, or measurement in the TGA instrument. Separate experiments were done using N_2 and Ar to purge the TGA furnace and balance, to examine possible reactions with N_2 . Gases evolved from the samples during TGA were analyzed by a sampling mass spectrometer (ThermoStar GSD301T3, Pfeiffer Vacuum), which monitored multiple mass channels as a function of time, allowing them to be correlated with the TGA temperature ramp.

Because the TGA-MS allowed monitoring of a limited number of masses, for the MMA-milled material, we first studied the desorption mass spectrum as a function of temperature, using the same mass spectrometer used for headspace analysis. A powder sample was collected after the completion of milling, using an Ar-filled glove box for sample collection to avoid any possibility of reaction of the aluminum nanopowder with N_2 . Approximately 200 mg of powder was transferred to a glass vial which was sealed in the argon-filled glove box, and then attached

to the mass spectrometer. The gas line between the sample vial and mass spectrometer leak valve was evacuated, and then gas from the vial was leaked into the mass spectrometer at a pressure of $\sim 1 \times 10^{-7}$ Torr. An initial mass spectrum was measured, and then the sample temperature (measured by a K-type thermocouple) was increased in a series of steps, using a tube furnace, and waiting 10 minutes for the temperature to equilibrate before taking mass spectra. The sample vial was sealed during heating, and only opened to allow mass spectral measurements after temperature equilibration. As a result, the mass spectra are for gas that evolved from the powder during heating to each temperature.

Infrared spectroscopy was attempted for both the ammonia- and MMA-milled samples. Both specular reflectance and diffuse reflectance were attempted using an instrument at Utah, and although it was used successfully for analysis of both boron¹⁶ and aluminum particles capped with oleic acid,²⁶ no significant absorption features were observed for aluminum produced by milling in NH_3 or CH_3NH_2 . Diffuse reflectance and attenuated total reflection experiments were also attempted using an instrument at Argonne National Lab, which is housed in an inert atmosphere glove box to minimize exposure to air. Again, however, no significant absorption features were observed in the 4000 cm^{-1} to 800 cm^{-1} spectral range. The lack of signal is tentatively attributed to a combination of low reflectivity of the nano-aluminum samples, together with a relatively low concentration of IR chromophores on the particle surfaces.

Density Functional Theory (DFT) calculations.

To help understand the reactions of NH_3 and MMA with aluminum surfaces, DFT was used to probe the interactions between a large aluminum cluster, and molecules of NH_3 or CH_3NH_2 . Structures and energetics were computed using the M06 hybrid meta-generalized gradient approximation (GGA) exchange-correlation functional of Zhao and Truhlar³⁹ and a Lebedev quadrature grid with 99 radial and 590 angular points. The McLean-Chandler (12s,9p)/[6s,5p] contracted basis set,⁴⁰ augmented with a d-type polarization function⁴¹ and diffuse s+p shell,⁴² was used for aluminum and the 6-311++G(d,p) basis set⁴²⁻⁴³ was used for carbon, nitrogen, and

hydrogen. This combination of functional and basis sets is henceforth denoted simply as M06/6-311++G(d,p). A cluster of eighty aluminum atoms was used as a model for the surface of the aluminum nanoparticles. Its geometry was optimized from a previously reported³⁰ calculated geometry for an 80 atom boron cluster, and it exposes a variety of surface sites, while being large enough to have a bulk-like core. All structures reported herein were fully optimized and, unless stated otherwise, have been verified as local minima or first order transition states via diagonalization of the hessian matrix; i.e., the mass-weighted energy second derivatives with respect to nuclear displacements. The minimum energy path, also known as the intrinsic reaction coordinate (IRC), connecting each transition state to reactants and products has been traced using the Gonzales-Schlegel second order method.⁴⁴ Relative energies include zero point vibrational energy (ZPE) corrections, obtained from the calculated harmonic vibrational frequencies which have been scaled by a factor of 0.983.³⁹ All calculations were performed using the GAMESS⁴⁵⁻⁴⁶ quantum chemistry program.

The primary purpose of these computations is to determine which species may be present on the surface of aluminum nanoparticles and the reactions leading to their formation. Such reactions should be consistent, in the case of NH_3 for example, with the observed formation of H_2 during milling, and also account for the absence of other stable product molecules such as N_2 , N_2H_2 , and N_2H_4 . The approach taken is to first consider the decomposition reactions of a single NH_3 chemisorbed on the surface of an Al_{80} cluster, followed by consideration of “bimolecular” reactions involving two neighboring chemisorbed ammonia molecules. A similar approach is applied to methylamine to determine which products may form on the nanoparticle surface from CH_3NH_2 , and to identify the reactions leading to their formation. Such reactions must be consistent with the experimental observation of H_2 , CH_2NH , and CH_3NHCH_3 products, as well as the absence of other stable species such as NH_3 , CH_4 , or CH_3CH_3 .

III. Results and Discussion

A. Aluminum nanoparticles from milling with NH_3

To track the progress from millimeter Al flakes to nanoparticles, in one experiment the jar was opened to allow particle sampling after each hour of milling, for a total of five hours. The jar was refilled with NH_3 after each particle sampling operation, and this was the only NH_3 milling experiment where additional NH_3 was added during the milling process. After milling one hour in 3.7 atm of ammonia, the initial 2 grams of aluminum flakes was reduced to a homogeneous, gray, metallic-looking powder. After a second hour of milling the material appeared homogeneously black, with no visible metallic luster, suggesting that the particle size had been reduced small enough to absorb light efficiently. Examination after 3, 4, and 5 hours of milling showed no further visible changes in the milling products.

For comparison, the 1 mm Al flake starting material was also milled in neat argon (99.9999%), nitrogen, and hydrogen gases. In all three experiments, the initial aluminum flakes were formed into 1 to 2 mm diameter aluminum spheres with no evidence of smaller particles. Because the mass of a ~1 mm sphere is much larger than that of a ~1 mm flake, it is clear that cold welding of the aluminum flakes to form larger particles was efficient in these gases. Given that Ar certainly does not bind to aluminum, the fact that the three gases had similar effects suggests that N_2 and H_2 also do not bind to aluminum under milling conditions.

Another qualitative indication that NH_3 binds to, or reacts with the aluminum surfaces is the effects on subsequent reactivity of the particles with air and water. Al nanoparticles are pyrophoric in air, and also react violently with liquid water unless their surfaces are passivated. Particles milled in ammonia and brought immediately out into the laboratory were not pyrophoric, and did not visibly react with liquid water (i.e., no H_2 gas generation), indicating the presence of a stable passivating layer. This passivating layer was not completely inert, however, because upon exposure to air, the particles, which were a free-flowing powder under inert atmosphere, rapidly caked and adhered strongly to the walls of the glass vial used to remove them from the glove box. As shown below, the passivating layer contains NH_x functionality, thus it is not surprising that the material is hygroscopic.

Particle sizes were analyzed using dynamic light scattering (DLS) to probe suspensions prepared by ultrasonication of a small sample of the particles in acetonitrile. The particle suspensions were stable for 15- 30 minutes, suggesting that the surfaces were functionalized such that they had at least some compatibility with the polar solvent. Figure 1 shows the bimodal mass-weighted size distribution measured for the ammonia-milled particles. The mode between 40 and 100 nm represents ~ 85% of the particle mass (~1.7 g), as reported by the instrument software, with the balance of the 2 gram batch consisting of particles in the ~250 – 600 nm range, which could either be large particles or aggregates of smaller primary particles. SEM analysis (insets to Fig 1) showed primary particles in the size range from ~75 to ~250 nm. This is somewhat larger than the 40-100 nm size mode that dominates the DLS distribution, but the discrepancy may simply reflect the effects of particle shape, which is not taken into account in the DLS analysis. Unlike the large aluminum particles produced by milling in liquid milling agents, which had flattened, plate-like shapes,²⁶ the nanoparticles produced by NH_3 -milling appear three dimensional, although they certainly are not spherical.

While we were unable to obtain IR spectra showing structure associated with the particle surfaces, two types of mass spectrometric analyses provide insight into the reactions of NH_3 with the aluminum particles, and the nature of species present on the surfaces after milling. The headspace gas for NH_3 milling was analyzed before starting milling and after one and two hours, with the results shown in Figure 2. Headspace gas sampling was done on separate milling runs to minimize perturbations to the jar atmosphere. Intensities were corrected for variation of sensitivity with mass, based on experiments where H_2 , NH_3 , and N_2 were leaked into the instrument at known pressures. The mass spectrum prior to milling, i.e., the spectrum of NH_3 , is dominated by peaks at masses 17 and 16. After one hour of milling, the ammonia peaks are substantially attenuated, strong signal is observed for H_2 (mass 2), and there is a weak feature at mass 28 indicating N_2 production. If ammonia were simply dissociating to form H_2 and N_2 , then the H_2 : N_2 peak ratio would be 3:1, rather than the 18:1 ratio observed. This result indicates that

ammonia reacts under milling conditions, with most of the nitrogen binding in some form to the aluminum, eliminating hydrogen, and generating a small amount of N_2 . After 2 hours of milling, there is no significant ammonia left in the headspace. Interestingly, the N_2 peak also disappears, indicating that under the late-stage milling conditions, i.e., in an atmosphere of mostly H_2 , the aluminum surfaces can also react with or bind N_2 in some fashion.

The fact that no NH_3 is left in the headspace after ≥ 2 hours of milling allows us to calculate the mass fraction of nitrogen in the final particles. From the jar volume (250 ml) and masses of aluminum and WC used, we can estimate the headspace volume at ~ 235 ml, thus 3.7 atm of NH_3 corresponds to ~ 0.5 grams of nitrogen. Assuming that all the nitrogen is bound to the 2 grams of nanoparticles formed, nitrogen is seen to make up $\sim 20\%$ of the particle mass. If this nitrogen were all in form of an AlN layer, and we approximate the actual particles by 75 nm diameter spherical particles, the AlN layer would be 10 nm thick. Such a thick layer would certainly account for the fact that these particles are not pyrophoric or reactive with water at room temperature.

TGA-MS was performed to look at desorption of products from the samples as a function of temperature. Separate experiments were done using nitrogen and argon as the furnace purge gas, to examine the possibility that aluminum might react with N_2 at elevated temperatures. Figure 3 shows the mass-loss curves for ammonia-milled aluminum nanoparticles in both argon and nitrogen gas flows. The particles heated in argon begin to lose mass at ~ 60 C, and then gradually lose up to $\sim 11\%$ of their mass as the temperature is ramped to 750 °C. The curve for heating in nitrogen is similar, and although there is slightly less net mass loss, there is no obvious signature of nitrogen uptake (see below). The lack of nitrogen uptake indicates that the as-milled particles are passivated with respect to reaction with N_2 , even when heated above the bulk aluminum melting point (660°C).⁴⁷

The other obvious question is what species desorb to account for the relatively large mass losses. The TGA curves show no sharp desorption features, and desorption occurs over a broad

temperature range, suggesting that the desorbing species have a wide range of binding energies, or that they form by decomposition of the thick capping layer on the particles. The temperature dependences of eight masses monitored during TGA are shown in Figure S1 of the supporting information. The only signals that increase significantly in the temperature range where mass loss is observed are for masses 16, 17, and 18. There is a small desorption feature for mass 18 in the temperature range between ~ 50 °C and ~ 100 °C, and a much larger feature in the $\sim 250 - 600$ °C range, both attributed to desorption of water. As shown in Figure 2, the mass spectrum for NH_3 is dominated by signals for masses 17 and 16, thus those TGA-MS signals are attributed to desorption of NH_3 , which shows a sharp onset at 100 °C and continues out to ~ 650 °C. Dissociative ionization of water would contribute $\sim 6\%$ of the mass 17 signal and $\sim 1\%$ of the mass 16 signal in the range between 250 and 650 °C. Taking dissociative ionization into account, we can estimate that the $\sim 11\%$ total mass loss results from loss of water amounting to $\sim 2\%$ of the particle mass, with NH_3 accounting for the remaining $\sim 9\%$ mass loss.

For both H_2O and NH_3 , desorption observed at low temperatures may result from molecularly adsorbed species, however, it is not likely that molecular species would bind strongly enough to persist at high temperatures.⁴⁸ Therefore, we attribute the high temperature desorption of these species to recombination reactions of surface functional groups such as $\text{OH}_{(\text{ads})}$, $\text{O}_{(\text{ads})}$, $\text{H}_{(\text{ads})}$, and $\text{NH}_{x(\text{ads})}$ in or on the capping layer. There are several likely sources of the oxygen in the NH_3 -milled samples, including the oxide layer present on the aluminum feedstock, and reactions with trace O_2 and H_2O in the atmosphere of the glove boxes used to handle and analyze the particles. Given that milling in NH_3 produces copious hydrogen, it is not unlikely some $\text{OH}_{(\text{ads})}$ and $\text{H}_2\text{O}_{(\text{ads})}$ is produced by reaction of H or H_2 with surface oxygen species.

It is useful to consider what the 11% mass loss during TGA implies about structure of the particle capping layer. If we, again, assume the particles can be represented by 75 nm spherical particles with bulk Al density, there would be an average of $\sim 1.3 \times 10^7$ atoms/particle, with $\sim 2\%$ ($\sim 2.7 \times 10^5$ atoms) in the surface layer. 11% mass loss in the form of ammonia and water from

such a particle corresponds to roughly 8.5 molecules *per* Al surface site. Even given the uncertainties introduced by distribution of particle size and shape, it is clear that considerably more than a monolayer's worth of NH_3 and H_2O desorbs from the particles.

It is also interesting to compare the nitrogen loss in TGA with the nitrogen content (20% by mass) implied by the NH_3 consumption during milling. NH_3 desorption (9% mass loss, of which 14/17th is N) removes less than 40% of this initial nitrogen content. As noted above, 20% N content would imply a ~10 nm capping layer if the capping layer were AlN , however, it is clear that the capping layer contains OH, NH_x , and other groups, i.e., that the layer has $\text{AlN}_x\text{O}_y\text{H}_z$ composition. Upon heating, this layer decomposes to generate NH_3 and H_2O that desorb, leaving behind ~60% of the initial nitrogen content in some non-volatile form (e.g. AlN_nO_m).

XPS was used to probe the chemical state of both the nitrogen and aluminum in the capping layer. A sample of the NH_3 -milled aluminum particles was transferred to the XPS instrument in an N_2 atmosphere using the manufacturer's inert transfer device, and a survey scan is given in Figure S2, showing the presence of aluminum, nitrogen, oxygen, and carbon. The sensitivity factors for Al, N, O, and C are 0.193, 0.477, 0.711, and 0.296,⁴⁹ thus the O and N signals are significantly exaggerated relative to those for Al in the raw spectrum. Carbon originates from adventitious adsorbates, probably mostly due to the presence of various solvent vapors in our glove box atmosphere. The signal for oxygen reflects all the sources of oxygen in this experiment, including the oxide layer present on the aluminum feed stock and reaction with contaminants in the glove box and inert transfer device atmospheres.

High resolution region scans of the Al 2p region are shown in Figure 4 both as-introduced into the XPS vacuum system, and after light sputtering done in an attempt to reduce the contributions from adventitious adsorbates. Analogous scans over the N 1s region are shown in Figure 5. The energy scale was corrected for shifts due to sample charging based on the O 1s peak, assumed to be due to aluminum oxide with binding energy of ~531.6 eV. The effective attenuation length⁵⁰ for Al photoelectrons in aluminum oxide or aluminum nitride is ~3.2 nm,

thus most of the XPS signal originates from the top 6 to 8 nm of the surface layer. The Al 2p spectrum is much broader than the instrumental resolution (~ 1 eV fwhm), suggesting that Al is present in a range of chemical states. As indicated on the figure, reported Al 2p binding energies range from 76.7 – 74.1 eV for aluminum oxides and hydroxides,^{49, 51-58, 59} from ~ 75 to 73.1 eV for aluminum nitrides,^{55, 57, 60-62} and from ~ 73 to ~ 72 eV for metallic Al (Al^0).^{38, 49, 54, 57-58, 61, 63} For the un-sputtered sample, the aluminum in the XPS-accessible surface layer is mostly oxidized, with binding energies in the range expected for nitrides and oxides/hydroxides, with a tail extending into the range expected for metallic Al. The weakness of the metallic Al signal is not surprising, given the results discussed above, which suggest that the $\text{AlN}_x\text{O}_y\text{H}_z$ capping layer is ~ 10 nm thick – enough to almost completely attenuate signal from the underlying Al particle core. After light sputtering, the metallic Al increased slightly, as might be expected due to sputtering of the surface layer, however, because the sample has many layers of particles present, additional $\text{AlN}_x\text{O}_y\text{H}_z$ is exposed as the top layer of particles is sputtered away.

Figure 5 shows the corresponding N 1s region scans with, and without light sputtering. The spectra are broad, again suggesting heterogeneity. The peak value at ~ 397 eV is consistent with nitride-like nitrogen,^{32, 49, 32, 38, 64-65} and the tail to high binding energy is consistent with NH_x -like nitrogen.⁴⁹ There is a small shift to lower binding energy after light sputtering, possibly indicating Ar^+ impact-induced conversion of NH_x -like nitrogen to more nitride-like bonding. The C 1s and O 1s high resolution spectra are not particularly informative, but are presented, with associated discussion, in the supporting information (Figures S3 and S4).

The above results indicate that the NH_3 -milled particles are capped with a ~ 10 nm thick $\text{AlN}_x\text{O}_y\text{H}_z$ layer in which nitrogen is present in both nitride and amine-like states. Amine-like nitrogen on the surface would explain the hygroscopic nature of the particles, by providing sites where water can hydrogen bond to the surface. Because we were unable to observe the IR fingerprint of the particles, we tested for amine-like NH_x surface functionality by reacting the particles with ketones, which might be expected to bind via Schiff base-like chemistry. Particles

were added to neat 3-pentanone or acetophenone and ultrasonicated for one hour.⁶⁶⁻⁶⁷ The excess ketone was rinsed away by repeatedly (three times) suspending the material in acetone, centrifuging particles out of suspension, and discarding the supernatant. As shown Figure S5, ammonia-milled particles exposed to 3-pentanone or acetophenone were dispersible in n-hexane (samples a and d), as would be expected if the ketone complexed with the surface. In contrast, the as-milled particles are incompatible with n-hexane, forming a globular mass of precipitate (sample b). For comparison, we also tried interacting the NH₃-milled particles with oleic acid by simply adding a drop of oleic acid to a vial containing as-milled particles and n-hexane (like sample b), then ultrasonicated for 5 minutes, resulting in a stable suspension, as might be expected if the acid were hydrogen bonding to the surface. XPS was used to look for evidence of acetophenone binding to the acetone-washed particle surfaces, and Figure S6 shows that acetophenone binding resulted in a substantial increase in C 1s signal, and substantial attenuations of the N, O, and Al signals, consistent with the presence of a carbonaceous overlayer attenuating signal from the underlying particles. The high resolution Al 2p, N 1s, O 1s, and C 1s spectra for the acetophenone-capped particles are given as Figures S7-S10. For these spectra, the energy scale was corrected for possible charging using the sp² hybridized C 1s signal at 284.8 eV. The Al 2p spectrum shows a strong peak for oxidized aluminum (AlN_xO_yH_z), with a small but distinct peak for metallic aluminum.

B. DFT results for NH₃ interactions with Al₈₀:

The structures and energetics of species formed by interaction of NH₃ with aluminum were probed via calculations for an Al₈₀ cluster with one or more NH₃ molecules present. Ammonia forms a weak dative bond to the surface of the Al₈₀ cluster, henceforth denoted as H₃N:Al₈₀. In order to assess the variability of the dative binding energies as a function of specific binding site, four distinct configurations of NH₃ chemisorbed to Al₈₀ were computed. These local minima have binding energies ranging from 8 to 16 kcal mol⁻¹, relative to separated Al₈₀ + NH₃, and are shown in Figure S11 in the ESI, along with additional description of the results.

Fragmentation of NH₃: As an initial investigation into the potential chemical reactivity of H₃N:Al₈₀, the energetics were computed for N-H bond dissociation and subsequent covalent binding of the resulting NH₂ and H fragments to Al₈₀, denoted as H₂N-Al₈₀-H. Several local minima of this type were found (Figure S12), bound by 17 to 30 kcal mol⁻¹ relative to separated NH₃ + Al₈₀. The greater stability of H₂N-Al₈₀-H (17 to 30 kcal mol⁻¹) relative to H₃N:Al₈₀ (8 to 16 kcal mol⁻¹) indicates that dissociation of chemisorbed NH₃ to form adsorbed H₂N and H is thermodynamically favored. The products of further N-H fragmentation, leading to chemisorbed NH and N species, are shown in Figures S13 and S14, respectively. As shown, a number of minima were found for NH_{ads} + 2 H_{ads} products with energies 10.6 to 35.4 kcal mol⁻¹ below the reactant energy – in the same energy range as those found for NH_{2ads} + H_{ads}. Two minima were found for N_{ads} + 3 H_{ads} with energies of 12.6 and 14.5 kcal mol⁻¹ with respect to reactants, i.e., complete dissociation is energetically uphill compared to NH_{2ads} + H and NH_{ads} + 2H_{ads}.

Since N-H bond dissociation in H₃N:Al₈₀ to form H₂N-Al₈₀-H is exothermic, calculations were performed to locate a transition state for this reaction. A saddle point for this reaction was located at 17 kcal mol⁻¹ above the NH₃ + Al₈₀ reactants, and the reaction path (IRC) is shown in Figures 6 and S15a. The IRC is not corrected for zero-point energy, but for the reactants, transition state, and products, both uncorrected and corrected values are given. Note that the reaction is exothermic by 2 kcal mol⁻¹ but that the barrier (31 kcal mol⁻¹ with respect to H₃N:Al₈₀) is higher than the barrier for simple desorption of ammonia from H₃N:Al₈₀ (14 kcal mol⁻¹). Therefore, desorption of NH₃ has a significantly lower activation energy than N-H dissociation via this saddle point. Note, however, that during milling collisions, adsorbed NH₃ may be trapped and unable to desorb. Furthermore, instantaneous temperatures during energetic collisions can reach 2000 K,⁶⁸ driving reactions that would be unlikely under purely thermal conditions. A similar conclusion can be drawn regarding dissociation of adsorbed NH₃ via a structurally distinct, but energetically similar saddle point which is shown in Figure S15b, where the reaction is 5 kcal mol⁻¹ exothermic, but crosses a 30 kcal mol⁻¹ barrier.

The reaction enthalpies and barriers for subsequent N-H fragmentation of chemisorbed $\text{NH}_2\text{-Al}_{80}\text{-H}$ to form $\text{NH-Al}_{80}\text{-2H}$, as well as the final N-H fragmentation step leading to chemisorbed $\text{N-Al}_{80}\text{-3H}$, were also calculated and are described in Figures S16-S18. The barrier heights for these fragmentation reactions, which range from 39 to 62 kcal mol^{-1} , are larger than the 33-35 kcal mol^{-1} barrier for the reverse of the initial fragmentation step ($\text{H}_2\text{N-Al}_{80}\text{-H} \rightarrow \text{H}_3\text{N:Al}_{80}$) and are not considered further.

Formation of H_2 :

H_2 is produced by milling Al in NH_3 (Fig. 2), and several elementary reactions leading to the formation of H_2 were considered. Although we were unable to find a reaction pathway leading to the formation of chemisorbed hydrogen atoms with a barrier less than the energy required for ammonia desorption, it is, nonetheless, possible that such a channel exists. For example, it may be that at the high NH_3 coverages that undoubtedly form during milling under several atmospheres of NH_3 , there are lower energy NH_3 dissociation pathways. Therefore, the reaction enthalpy and barrier for recombination of two chemisorbed H atoms to form H_2 were calculated, with the saddle point and IRC shown in Figure S19. This reaction is endothermic by 4 kcal mol^{-1} and has a barrier of 25 kcal mol^{-1} . To assess the mobility of chemisorbed hydrogen atoms on the cluster surface, reaction paths and barriers for migration of a hydrogen atom between aluminum atom binding sites were computed and are shown in Figure S20. The barrier for H atom migration, which ranges from 2 to 17 kcal mol^{-1} , is less than the barrier for recombination (25 kcal mol^{-1}), i.e., migration should be facile compared to recombinative desorption of H_2 .

The second pathway to H_2 considered is 1,1 elimination of H_2 from the amino group in chemisorbed ammonia, resulting in formation of $\text{HN-Al}_{80} + \text{H}_2$. Several unsuccessful attempts were made to locate the saddle point for this process. However, three distinct local minima corresponding to the products formed via this process ($\text{HN-Al}_{80} + \text{H}_2$) were located, with binding energies ranging from 7 to 24 kcal mol^{-1} relative to $\text{NH}_3 + \text{Al}_{80}$ (see Figure S21.) Therefore, with

respect to $\text{H}_3\text{N}:\text{Al}_{80}$, both endothermic and exothermic pathways for 1,1 elimination of H_2 are possible, although the barriers are unknown.

Another possible pathway to H_2 might involve reaction of neighboring chemisorbed H and NH_3 (Figure S22) which was found to be endothermic by 1 kcal mol⁻¹ with a small barrier of 12 kcal mol⁻¹. A fourth H_2 formation mechanism might involve “bimolecular” elimination of H_2 from adjacent chemisorbed ammonia molecules ($\text{H}_3\text{N}:\text{Al}_{80}:\text{NH}_3 \rightarrow \text{H}_2\text{N}-\text{Al}_{80}-\text{NH}_2 + \text{H}_2$). As seen in Figure S23, this reaction is exothermic by 18 kcal mol⁻¹, however, the saddle point located for this reaction lies 28 kcal mol⁻¹ above the $2\text{NH}_3 + \text{Al}_{80}$ asymptote, or more than 50 kcal mol⁻¹ above the $\text{H}_3\text{N}:\text{Al}_{80}:\text{NH}_3$ energy. It is, therefore, more energetically favorable for NH_3 to simply desorb, and because H_2 formation via this saddle point is unlikely, the IRC calculations to confirm the corresponding reactants and products were not performed. The final pathway considered is bimolecular H_2 elimination from two chemisorbed NH_2 moieties; i.e., $\text{H}_2\text{N}-\text{Al}_{80}-\text{NH}_2 \rightarrow \text{HN}-\text{Al}_{80}-\text{NH} + \text{H}_2$, which was found to be endothermic by 10 kcal mol⁻¹ and for which transition state searches were unsuccessful.

It is important to note that our DFT calculations were limited to a simplified model of the experiments: Al_{80} under conditions of low adsorbate coverage, i.e., at most a few NH_x or H adsorbates/cluster. Given that NH_3 binding to Al_{80} is found to be energetically favorable, it is almost certain that in the experiments, freshly exposed aluminum surfaces are saturated with NH_3 (or fragments thereof) which may significantly change the energetics for NH_3 adsorption, dissociative chemisorption, and for bimolecular reactions between neighboring adsorbates. In addition, it is clear that as milling continues, a relatively thick $\text{AlN}_x\text{O}_y\text{H}_z$ layer forms, indicating that reactions continue well beyond the point of simply producing a saturated monolayer on the Al surface. While it is impractical to include high coverages, impurities, etc. in the DFT model, the results, nonetheless, provide insight into the initial reactions of NH_3 on aluminum surfaces.

The DFT calculations show (Figure S18) that adsorption of NH_3 on aluminum is energetically favorable, and that dissociation to chemisorbed $\text{NH}_2 + \text{H}$ or $\text{NH} + 2\text{H}$ can be exothermic,

although we were not able to find transition states with energies below the desorption energy of $\text{H}_3\text{N-Al}_{80}$. Similarly reaction pathways for H_2 formation were found that are exothermic (i.e., 1,1 elimination from chemisorbed NH_3 and bimolecular elimination from two NH_3 molecules) or which have a modest barrier (recombination of two chemisorbed H atoms or elimination from co-adsorbed H and NH_3). Although the complexity of the system precludes exhaustive searches of the large number of potential adsorption geometries and reaction paths, consideration of the DFT and experimental results suggests that the initial species formed in interaction of NH_3 with aluminum are chemisorbed NH_3 , NH_2 , and H. In addition, as discussed further in the supporting information, formation of N_2 , N_2H_2 , and N_2H_4 via the recombination of chemisorbed species such as H, N, NH, and NH_2 , are highly endothermic processes ($\sim +42$, $+103$, and $+80 \text{ kcal mol}^{-1}$, respectively, as shown in Figure S24.) This finding is consistent with the experimental observation of H_2 as the predominant gaseous product, with minimal N_2 production in the ball milling experiments.

C. Aluminum nanoparticles produced by milling in MMA.

While the fact that ammonia serves as an efficient size-reduction agent in aluminum ball milling is interesting, the observation that the resulting particles are heavily passivated by a thick $\text{AlN}_x\text{O}_y\text{H}_z$ layer makes the particles less interesting from the fuels perspective. Particles produced in monomethylamine (MMA) atmospheres are more promising. As noted, the MMA vapor pressure is only $\sim 2 \text{ atm}$, and to compensate for the lower initial concentration of reactive gas present, the jar was evacuated and refilled with fresh MMA after each hour of milling. After 4 hours, the result was conversion of the initial ~ 2 grams of millimeter aluminum flakes to a homogeneous dark black powder that resembled the ammonia-milled particles. Unlike the ammonia-milled samples, however, these particles were pyrophoric, autoigniting within a few seconds upon air exposure. Higher reactivity could result from several factors. MMA milling might result in less thoroughly passivated particles, but it is also possible that smaller particle sizes might contribute to the higher reactivity, because small particles have less bulk to dissipate

heat generated by surface reactions, and thus are more prone to autoignition.

The particle size distribution was measured by DLS, after dispersing the particles in acetonitrile, and the result is shown in Figure 7. The size distribution was bimodal, with a “small particle” mode in the 100 to 200 nm range accounting for ~63% of the particle mass, with the balance in a mode ranging from ~450 to 900 nm. SEM of these particles (Figure 7, inset) shows what appear to be primary particles in the size range between ~60 nm to ~300 nm, with a few ranging up to ~500nm in size. The particles look relatively smooth, but are elongated and appear somewhat flattened. Given the lack of shape sensitivity of DLS, the agreement with SEM is reasonable, and suggests that ~450-900 nm mode seen in DLS consists of aggregates. Both SEM and DLS measurements indicate that the particles produced by MMA milling are somewhat larger than those produced in NH_3 . We, therefore, conclude that the substantially higher reactivity observed for MMA-milled particles is a result of less passivated surfaces, compared to particles produced by NH_3 -milling.

Headspace analysis was performed after each hour of milling in MMA, and the results are presented in Figure 8. The MMA molecular mass is 31, however, the largest peak in the mass spectrum is mass 30, and to account for fill-to-fill variation in the MMA pressure, each spectrum was normalized to constant mass 30 intensity. The “initial” mass spectrum is for MMA prior to milling, and is in good agreement with the literature spectrum for MMA,⁶⁹ with the exception that there are a number of barely detectable peaks in the mass 40 to 45 range (see inset), which match reasonably well to the expected intensity pattern for dimethylamine.⁷⁰ Apparently the MMA gas either had dimethylamine contamination on the order of 1%, or reacted upon introduction to the milling jar to produce it.

After one hour of milling, the spectrum is dominated by mass 2, indicating significant production of H_2 , and by peaks due to residual MMA in the milling atmosphere (recall that the spectra are normalized to constant mass 30 intensity). During the second hour of milling (after evacuating the jar, and refilling with fresh MMA), H_2 was again the major gaseous product.

Indeed, the only significant signals in the 2nd hour spectrum were for H₂ and residual MMA (the mass 15 peak is from dissociative ionization of MMA). The amount of H₂ produced during each hour of milling clearly declined with time, such that by the fourth hour, there is little evidence of reaction, and only unreacted MMA is present. Given that MMA appears to react with fresh aluminum surfaces generated during size reduction, the implication is that the net production of new surface area declines after 2 to 3 hours of milling.

In addition to H₂ and residual MMA, the 1st hour spectrum shows evidence of a number of other gaseous species. The fact that these peaks are absent in later spectra suggest that their source is contaminants, or reaction products of contaminants introduced on the surfaces of the aluminum feedstock or milling media, such that they are lost when the jar is evacuated and refilled after the 1st hour. While these are minor products, considering their origins provides some insight into the chemistry occurring during milling. Mass 46 almost has to be either C₂H₆O⁺ or N₂O⁺, and in the former case there would also be a contribution to mass 45. The high intensity at 44 suggests CO₂. Hydrocarbon contaminants (e.g. hexane used for media and jar cleaning) would crack to give a variety of C_nH_m⁺ ions, although it should be noted that cracking of higher hydrocarbons cannot account for the enhanced signal at masses 44 and 28, or the peaks at masses 16 through 18. The increase, compared to the MMA spectrum, in the relative intensity of mass 28 in the 1st hour spectrum is too large to explain as CO⁺ from CO₂, and thus production of a small amount of N₂, as was seen after the first hour of NH₃ milling. The small peaks at masses 12 - 18 are partly attributable to dissociative ionization of MMA and dimethylamine, however, there also appears to be some production of methane and water. Methane formation might be expected to accompany N₂ production, and as shown next, both methane and water desorb from the MMA-milled particles when they are heated.

As with the ammonia-milled samples, mass spectrometry was used to probe gases desorbing from a particle sample as it was heated. Because the number of potential products is higher for MMA, and the TGA-MS instrument only allows a limited number peaks to be monitored, we first

examined full desorption mass spectra for temperatures up to 300 °C, in order to identify products via fragmentation patterns, and to choose peaks for TGA-MS analysis. For this measurement, ~250 mg of particles were collected from the jar after the 4th milling hour, and transferred to a vial in the glove box. The vial was attached to the inlet of the same mass spectrometer used for the headspace analysis, evacuated to remove the glove box N₂, resealed, and then stepped through a series of temperatures, taking a mass spectrum of the desorbed gasses after temperature equilibration (Figure 9). For reference, the spectrum of neat MMA is shown at the bottom of the figure. At 50 °C, there is already significant signal for products desorbing from the sample. The mass 28 peak, which was allowed to go off scale, is attributed mostly to residual glove box N₂, which also contributes to mass 14. Those peaks aside, the mass pattern can be assigned to the following desorbing species, in descending order of importance: MMA, H₂, water, methane, and dimethylamine. There is also a peak at mass 32, only a few percent of which can be attributed to ¹³CH₃NH₂, suggesting the presence of O₂. Given that these particles are reactive enough with oxygen to be pyrophoric in air, it would be surprising if free O₂ could exist in the sample. More likely, O₂ may have outgassed from the gas line connecting the sample vial to the mass spectrometer inlet. The H₂ signal peaks at 100 °C, and by that point, the water, O₂, N₂, methane, and dimethylamine signals decrease substantially. The H₂ signal decreases sharply at 200 °C and above, such that the dominant desorption signal is for MMA, with only small amounts of H₂, water, and methane remaining at 300 °C.

The TGA results for MMA-milled aluminum particles in both N₂ and Ar purge gases are shown in Figure 10. Mass loss begins at ~60 °C and reaches ~13% by ~500 °C, compared to ~11% mass loss by ~650 °C for NH₃-milled particles (Figure 3). While the results are superficially similar for the NH₃- and MMA-milled particles, it is important to note that 80% of the mass loss for the MMA-milled particles occurs below 250 °C, compared to ~500 °C for the NH₃-milled particles. Clearly the capping layer is more weakly bound in the MMA case. More obviously, when N₂ is used as the purge gas, the MMA-milled particles show rapid mass gain

starting near the melting point of bulk aluminum (660 °C). The small mass gain noted for Ar furnace gas is attributed to infiltration of N₂ from the surrounding glove box into the TGA. The mass gain presumably indicates reaction to form some thermally stable aluminum-nitrogen compound.

During TGA, the intensities of the mass peaks at 2, 14, 15, 16, 17, 18, 26, 27, 28, 29, 30, 31, and 32 were monitored as a function of temperature, and this data set is given in Figures S25 and S26. Masses 30 and 31, which are major peaks for ionization of MMA (see Figure 9, bottom) show a desorption feature with onset near 50 °C, peak near 100 °C, and ending near 250 °C. As required if MMA is, indeed, the main desorption product, all the other minor peaks expected for MMA ionization (14, 15, 26, and 32 = ¹³CH₃NH₂) also show a similar desorption component. Mass 28, which is also a major MMA mass spectral peak, has such high background in the mass spectrometer, that it is impossible to observe any increase from desorbing MMA. Mass 18, which is attributed to water desorption, also shows a similar desorption feature, and the mass 16 and 17 signals, therefore, must have contributions from both MMA and water desorption.

The only mass showing a significantly different desorption temperature dependence is mass 29. This mass shows a minor feature at low temperatures, as expected from dissociative ionization of desorbing MMA, but also a major feature starting at ~375 °C, which is not seen for any of the other masses associated with MMA ionization. The mass 29 ion is almost certainly CH₂=NH⁺, suggesting that the molecule desorbing at high temperatures is methanimine, i.e., MMA which has lost H₂. This desorption channel was not seen in the mass spectra in Figure 9 because we were not able to reach high enough temperatures with the glass sample vial. It is not clear if the appearance of this mass at high temperatures results from adsorbed CH₂=NH that is bound so strongly that it only desorbs above 375 °C, or if this is the temperature where adsorbed MMA begins to dehydrogenate. Unfortunately, the high background/low sensitivity of the TGA-MS for mass 2 precludes looking for H₂ desorption coincident with methanimine desorption.

Because of the extensive fragmentation of MMA, and high background at some masses of interest, there is considerable uncertainty in the integrated desorption intensities, however, we can say that water, MMA, and methanimine are the main desorption products. MMA and water, which desorb with roughly equal intensities, mostly in the 50 – 250 °C range, account for ~90% of the total mass loss, with the balance due to methanimine desorbing above 375 °C.

As with the NH₃-milled particles, FTIR characterization failed, however, XPS provides some insight into the nature of the MMA capping layer. As might be expected from the lower desorption temperatures seen for the MMA-milled sample in TGA, this sample was found to outgas badly in the XPS instrument, and it was necessary to degas the sample before introduction into the ultra-high vacuum chamber. To avoid tying up the XPS load lock chamber for degassing, a new sample was prepared and loaded into the inert transfer device in the glove box, and then the transfer device was attached to a small vacuum chamber with a base pressure of $\sim 3 \times 10^{-8}$ Torr. The transfer device was then opened in this chamber (leading to an increase in pressure to 1×10^{-7} Torr), and allowed to pump until the pressure had decreased back to baseline, which took 2 days. At that point, the transfer device was sealed, pressurized with Ar, and transferred to the XPS instrument. XPS was obtained immediately after transfer to the instrument, and then to examine the effects of air exposure, the sample was moved into the instrument load-lock chamber, briefly exposed to laboratory air, then pumped down and then reintroduced to the XPS analysis chamber. The post exposure XPS was done using a different area on the sample to avoid potential X-ray damage artifacts. Peak energies were adjusted using the C 1s adventitious peak at 284.8 eV for the air-exposed sample.

The Al 2p spectra for this sample are presented in Figure 11. In comparison to the Al 2p spectrum for NH₃-milled aluminum, the as-transferred (“Inert”) spectrum is considerably sharper, with a distinct peak around 72 eV, attributed to Al⁰ in the particle core, and a somewhat broader peak near 74.5 eV in the range expected for aluminum oxides and nitrides.^{41, 48, 52-53} The distinct peak for Al⁰ suggests that the capping layer is thinner on the MMA-milled particles, although the

nitride/oxide component still dominates the spectrum. The effect of air exposure was modest, mostly appearing as a broadening of the metallic aluminum peak in the “Exposed” spectrum. Since we know that freshly milled samples of this material are pyrophoric, the small effect observed for air exposure in the instrument load lock probably indicates that the sample had already received significant exposure to oxidizing contaminants during preparation in the glove box and transfer to the XPS instrument, and thus was already largely passivated.

The N 1s spectra presented in Figure 12 also show signs that the MMA capping layer is quite different than that formed by NH₃ milling. The higher binding energy N 1s component, peaking near 399 eV, is in the range expected for organic nitrogen^{65, 71} and is consistent with the observation that intact MMA (and dimethylamine and CH₂NH) desorb from this material starting at quite low temperatures. For comparison, the NH₃-milled sample (Figure 5) shows no distinct feature in this high binding energy range. The lower binding energy component, peaking near 397 (~0.5 eV lower than the peak for NH₃-milled aluminum), is consistent with binding energies reported for metal nitrides.

The other major difference is that the amount of nitrogen in the surface layer of the MMA-milled particles is smaller than for the NH₃-milled sample, as can be inferred by comparing signal-to-noise ratios of the spectra in Figures 5 and 12. Integration of the background-subtracted spectra shows, in fact, that the XPS-visible N 1s signal is 6 times smaller for the MMA-milled sample. Given the estimate, from NH₃ consumption, that the capping layer on the NH₃-milled particles is ~10 nm thick, the XPS results suggest a capping layer thickness in the ~2 nm range. Furthermore, the observation that intact MMA desorbs from these particles at low temperatures suggests that a significant fraction is simply molecularly adsorbed to the surface of the particles, and this conclusion is supported by the presence of the high binding energy N 1s component in Figure 12.

After air exposure, the spectrum broadens and shifts slightly to lower binding energy, but the relative intensities of the high and low binding energy components is unchanged, presumably

reflecting the unavoidable oxygen exposure even in the inert-transferred sample. C 1s and O 1s region spectra for the as-transferred and air-exposed samples are presented Figures S27 and S28. Perhaps the only point of interest is that the O 1s intensity does not increase significantly after air exposure, again consistent with the idea that the sample was already largely passivated by reaction with oxidizing contaminants in the glove box and inert transfer device atmospheres.

D. DFT results for $\text{CH}_3\text{NH}_2 + \text{Al}_{80}$:

Similar to the case of ammonia, monomethylamine forms a weak dative bond to the surface of the Al_{80} cluster with a binding energy of 18 kcal/mol, with structure illustrated in Figure S29. Starting from this structure, three bond dissociation pathways (N-H, C-H, and C-N bond scissions) of chemisorbed monomethylamine, denoted henceforth as $\text{MMA}:\text{Al}_{80}$, were considered. The final products of these three reactions are shown in Figure 13. Dissociation of an N-H bond to form chemisorbed CH_3NH and H ($\text{CH}_3\text{NH}-\text{Al}_{80}-\text{H}$; see Figure 13a) is exothermic by 8 kcal mol⁻¹ relative to $\text{MMA}:\text{Al}_{80}$. C-H bond dissociation leading to formation of $(\text{CH}_2\text{NH}_2)-\text{Al}_{80}-\text{H}$ (Figure 13b) is endothermic by 2 kcal mol⁻¹ with respect to $\text{MMA}:\text{Al}_{80}$. In contrast, cleavage of the C-N bond to form $\text{CH}_3-\text{Al}_{80}-\text{NH}_2$ (Figure 13c) is exothermic by 26 kcal mol⁻¹ and therefore the most thermodynamically favorable of the three bond dissociation reactions. Additional isomers, with energetics, for the dissociation products $\text{CH}_3\text{NH}-\text{Al}_{80}-\text{H}$, $(\text{CH}_2\text{NH}_2)-\text{Al}_{80}-\text{H}$, and $\text{CH}_3-\text{Al}_{80}-\text{NH}_2$ are shown in Figure S30.

Saddle points were found for N-H and C-H fragmentation in $\text{MMA}:\text{Al}_{80}$, as discussed in the supporting information and shown in Figures S31 and S32. Although calculations to locate the saddle point for C-N bond fragmentation in $\text{MMA}:\text{Al}_{80}$ to produce $\text{CH}_3-\text{Al}_{80}-\text{NH}_2$ were unsuccessful, a transition state leading to formation of the latter from $(\text{CH}_2\text{NH}_2)-\text{Al}_{80}-\text{H}$ was located and is shown in Figure S33. Of these three pathways, N-H fragmentation has the lowest barrier (26 kcal mol⁻¹). Nonetheless, the corresponding saddle point is 8 kcal mol⁻¹ higher in energy than separated $\text{MMA} + \text{Al}_{80}$, indicating that simple desorption of CH_3NH_2 from $\text{MMA}:\text{Al}_{80}$ is a more favorable process than N-H fragmentation. As discussed above, however,

under the instantaneous conditions arising during milling collisions, it is not unlikely that high energy reaction channels may be significant.

Formation of H₂: As discussed in the ESI, several pathways leading to formation of H₂ were considered, including (a) H₂ elimination from chemisorbed CH₃ and NH₂, unimolecular H₂ elimination from MMA:Al₈₀, and (c) bimolecular H₂ elimination from neighboring chemisorbed MMA molecules, MMA:Al₈₀:MMA (see Figures S34-S35.) Only in the latter instance were exothermic pathways found, with the reaction CH₃NH₂:Al₈₀:NH₂CH₃ → CH₃NH-Al₈₀-NHCH₃ + H₂ having the largest exothermicity, 17 kcal mol⁻¹, and thus representing the most probable means of H₂ formation.

Formation of CH₂=NH: As shown above, there is evidence for desorption of methanimine (CH₂NH) above 375 °C, and discussed in the supporting information, the calculated reaction enthalpy to form chemisorbed CH₂=NH via a concerted 1,2 elimination of H₂ from MMA:Al₈₀ is endothermic by 28 kcal mol⁻¹, i.e., well above the desorption energy for intact MMA (see Figure S34b.) In contrast, stepwise H atom elimination, shown in Figure S36, resulting in formation of CH₂=NH:Al₈₀-2H is endothermic by only 17 kcal mol⁻¹, which is slightly less than the energy required for intact desorption of MMA (18 kcal mol⁻¹.) Regarding the two possible stepwise pathways shown in Figure S36, the one occurring via initial C-H fragmentation (panel a) must traverse a barrier of 50 kcal mol⁻¹, as illustrated in Figure S32. In contrast, the stepwise pathway via initial N-H fragmentation (panel b in Figure S36) presumably has a barrier similar to that of the reaction pathway illustrated in Figure S31 (26 kcal mol⁻¹.) The latter pathway provides an energetically reasonable mechanism for production of CH₂=NH, assuming that the unknown barrier for elimination of the second H atom (i.e., CH₃NH-Al₈₀-H → CH₂=NH:Al₈₀-2H) is not excessively large. Furthermore, the two adsorbed H atoms can undergo recombinative desorption at high temperatures, providing an additional route to the major H₂ product.

Formation of CH₃NHCH₃: Three elementary bimolecular reactions leading to the formation of chemisorbed dimethylamine (DMA:Al₈₀) were considered and are described in the

supplementary information (see Figures S37-S39.) Of these, only one is exothermic (17 kcal mol⁻¹, involving the migration of a methyl group from chemisorbed MMA to a neighboring chemisorbed -NHCH₃ group, resulting in formation of H₂N-Al₈₀:DMA.

Formation of NH₃, CH₄, and CH₃CH₃: The most direct and plausible routes to formation of NH₃ and CH₄ are via recombination of chemisorbed NH₂ + H and CH₃ + H, respectively. However, a facile pathway leading to chemisorbed NH₂ or CH₃ starting from MMA:Al₈₀ has not been found. Although formation of chemisorbed NH₂ and CH₃ could occur by the two-step process described earlier; namely, initial C-H fragmentation in MMA:Al₈₀ (Figure S32) followed by C-N fragmentation of chemisorbed CH₂NH₂ (Figure S33,) the first step in this process must traverse a large barrier of 50 kcal mol⁻¹ and therefore is unlikely to occur to a significant extent. Even if chemisorbed CH₃ were present on the aluminum surface, recombination with a chemisorbed H atom to produce CH₄ has a calculated barrier of 43 kcal mol⁻¹, as shown in Figure S40, presumably accounting for the minor amount of CH₃ observed.

Similarly, since the most straightforward route to formation of ethane is via recombination of chemisorbed CH₃ fragments, the absence of ethane as a product is likewise consistent with the unlikelihood of forming chemisorbed CH₃. Although recombination of two chemisorbed methyl groups to produce ethane is endothermic by only 7-15 kcal mol⁻¹, the barrier for this process is unknown.

In summary, the DFT calculations show that adsorption of MMA onto aluminum is energetically favorable, with little or no activation energy. Reactions leading to products such as H₂, CH₂=NH, dimethylamine, and other products were found to be exothermic, or with endothermicity in a range accessible at milling temperatures ($T_{\text{average}} < \sim 380$ K). Many of these processes were found to have high activation barriers, however, and we did not identify obvious pathways to many of the observed products. Again, however, we emphasize that the DFT calculations were done in the limit of very low adsorbate coverage. Under the experimental conditions, we expect that the surfaces should be saturated by MMA, which is likely to change

the energetics for some of the decomposition reactions, and possible open new reaction pathways. In addition, the high instantaneous temperatures reached during energetic collisions in the mill,⁶⁸ may drive reactions that would be unlikely under purely thermal conditions.

IV. Conclusions.

We previously demonstrated that aluminum nanoparticles can be produced by milling in liquid reagents or solutions thereof, which bind to newly created surfaces, lowering the free energy of surface creation, and reducing the tendency toward cold-welding.²⁶ Milling in liquids that do not bind strongly to aluminum (e.g. alkanes) resulted in no particle production. The best liquid milling agent found was neat acetonitrile, which resulted in efficient particle production, but with roughly equal masses of nanoparticles and micron scale particles. We also examined milling with oleic acid and solutions thereof, and in liquid amines (oleylamine and benzylamine), and found that while there was efficient production of particles, at most 10% of the product mass was nanoparticles. In contrast, we have shown above that milling in gaseous amines results in rapid and exclusive production of nanoparticles, mostly in the 40-100 nm range for NH₃, and in the 100-250 nm range for MMA. As also discussed above, milling in H₂, Ar, or N₂ atmospheres resulted in no particle production, but rather lead to cold welding of the aluminum flake feedstock to form 1 to 2 mm diameter spheres.

The much more efficient size reduction in gaseous amines, compared to liquid milling agents, may be influenced by effects such as surface lubrication and evaporative cooling by the liquids, however, we propose that the much faster molecular velocities and low viscosity of gaseous reactants are also quite important. Their high diffusion speeds means that a high density of reactant molecules is present at internal surfaces of cracks formed by milling impacts, adsorbing and thereby reducing the energy required to propagate the cracks (*vide infra*). For viscous liquids or liquid solutions, delivery of the surface-active molecules to the crack tip may be slow, and for bulky molecules (e.g. oleic acid), steric effects will also limit the coverage. Its small size may explain why neat acetonitrile was the best liquid agent found for Al nanoparticle production.

Consider the equilibrium for molecularly adsorbed NH₃ and MMA on aluminum surfaces. The collision rate for NH₃ under the conditions present as milling was started (~3 atm, 350 K) is ~10⁹ sec⁻¹ *per* surface aluminum atom, and the analogous rate for MMA is ~4x10⁸ sec⁻¹. Given the calculated binding energies (E_{des}), ranging from ~8 to ~18 kcal/mol depending on binding site, and assuming barrierless first order desorption ($k = \nu \cdot \exp\left(-\frac{E_{des}}{kT}\right)$), with $\nu \approx 10^{14}$ sec⁻¹, we can estimate that the desorption rates will range from ~10⁹ sec⁻¹ to ~10³ sec⁻¹ over the range of binding energies. The ratio of the collision and desorption rates implies that the steady state occupancy will be substantial, even for the weakest binding sites, and that the stronger binding sites will essentially be saturated within nanoseconds of their initial exposure to the milling gases.

The process of converting millimeter flakes to 100 nm particles with aspect ratios similar to those shown in Figs. 1 and 7 creates roughly ~25 m² of new surface area *per* gram of particles. The free energies of aluminum surfaces such as Al(111), Al(110), and Al(210), are reported to be in the range of 1.14 to 1.16 J/m²,⁷²⁻⁷⁴ and high index/defective surfaces produced by milling are likely to have somewhat higher energies.⁷⁵ 1.16 J/m² corresponds to ~0.55 eV/surface atom, or ~12.7 kcal/mol of surface atoms. As discussed above, the calculated energy of the NH₃:Al₈₀ dative bond varies from 8 kcal/mol to 16 kcal/mol, and the MMA:Al₈₀ bond is ~18 kcal/mol. The degree to which adsorption can compensate for the energy required to create new Al surface area depends on the coverage. The calculated structures (Figures S11, S22, S29, S35) suggest that the maximum coverage might approach ~ 0.25 to 0.5 NH₃ or MMA molecules per Al atom, and such coverages are also consistent with comparison of the effective van der Waals diameter of NH₃ (~4 Å),⁷⁶ and the Al-Al spacings, which are 2.86 Å and 4.04 Å for the (110) surface,⁷⁷ for example. In addition to adsorption of intact NH₃ and MMA, however, the production of H₂ and other minor gaseous products during milling suggest that dissociative adsorption must also occur, and this process should result in not only higher coverage but also higher binding energy. For example, our calculations show that NH₂ and H adsorb to neighboring Al atoms with net binding energy of

up to ~30 kcal/mol – enough to essentially cancel the energy cost of creating new surface area. The high adsorption energies, and the fact that both NH_3 and MMA are gases able to rapidly penetrate small cracks, presumably accounts for why both are such effective milling agents.

The DFT calculations found that adsorption of intact NH_3 and MMA is exoergic, and that a variety of dissociative adsorption processes are also exoergic, however, we were unable to find low energy transition states leading these adsorbed decomposition products. Nonetheless, it is clear that there is substantial decomposition of the adsorbed reactants, as shown by copious production of H_2 during milling, and XPS and TGA results showing that the particles are capped with a few nanometers of some material containing aluminum with nitride-like Al 2p binding energy, and nitrogen with both nitride and organic nitrogen-like N1s binding energies. Under the high coverages and extreme instantaneous temperature conditions generated in milling, there evidently are efficient decomposition pathways.

The mass and temperature data from TGA provide additional insight into the nature of the particle capping layers. Both NH_3 - and MMA-milled particles undergo loss of 10% - 13% of their initial masses, corresponding to a few monolayers worth of material desorbing. In both cases, the reactants themselves, i.e., NH_3 or MMA, are major desorption products, although there is also water for the ammonia-milled particles (Figs. 3 and S1), and CH_2NH , (Figs. S25-S26) and H_2 (Fig. 9) for the MMA-milled particles. H_2 may also be evolved by the NH_3 -milled sample, we were not able to monitor its mass in the TGA-MS experiment.

While the desorption behavior is superficially similar for NH_3 - and MMA- milled particles, the temperature dependence of the desorption is quite different. As shown in Figures 3 and 10, mass loss in both cases begins at 60 – 70 °C, however, for the MMA-milled particles ~80% of the mass loss occurs below ~250 °C, while for the NH_3 -milled particles, only ~27% of the mass loss occurs below 250 °C, and 80% loss requires heating to ~525 °C.

The XPS results for the two samples are also different, and suggest an explanation for the differences in desorption behavior. For the NH_3 -milled particles, there is relatively little XPS

signal arising from Al^0 in the particle cores, and there is strong N 1s signal mostly corresponding to some nitride-like state. The TGA and XPS results suggest that the particles are capped with a thick layer of some $\text{AlN}_x\text{O}_y\text{H}_z$ composition, with additional NH_3 molecularly adsorbed on the surfaces. When heated, such a layer would tend to evolve molecularly adsorbed NH_3 at low temperatures, and then produce NH_3 and H_2O by decomposition of the $\text{AlN}_x\text{O}_y\text{H}_z$ layer at high temperatures, as is observed. From the weakness of the XPS Al^0 signal, and the ~ 3.2 nm effective attenuation length⁵⁰ for Al photoelectrons in such a layer, we can estimate that the total layer thickness must be ~ 4 to 5 nm, and it is not surprising that such a thick passivating layer would render the particles inert with respect to autoignition in air and toward reaction with N_2 at high temperatures.

For the MMA-milled particles, XPS shows higher Al^0 signal from the particle cores compared to the NH_3 -milled case, and the nitrogen signal is roughly equal divided between nitride-like and amine-like binding energies. The MMA-milled particles are also moderately pyrophoric, and react with N_2 above 650°C . The total mass loss is quite similar to that of the NH_3 -milled particles, but occurs at much lower temperatures. We interpret these results to indicate the presence of a relatively thin layer of fully passivated nitride-like aluminum, with a substantial amount of MMA molecularly adsorbed on its surface. A capping layer of such structure would give rise to substantial mass loss from molecularly adsorbed MMA at low temperatures, with additional MMA and CH_2NH being produced at higher temperatures (above 350°C) from decomposition/recombination of dissociatively adsorbed species, strongly bound to Al, giving rise to nitride-like Al and N XPS binding energies. The one surprise is that H_2 is observed to desorb primarily below 100°C (Figure 9), i.e., far below the temperatures where dehydrogenation reactions of adsorbed CH_xNH_y species might be expected. We note that copious H_2 is produced during milling, and it is possible that some becomes physically trapped in the layer of MMA bound to the particles, and thus desorbs along with the MMA.

Acknowledgements: The authors acknowledge support from the Air Force Office of Scientific Research under AFOSR MURI Grant FA9550-08-1-0400 and BRI Grant FA9550-12-1-0481. This work made use of University of Utah shared facilities of the Micron Technology Foundation Inc. Microscopy Suite sponsored by the College of Engineering, Health Sciences Center, Office of the Vice President for Research, and the Utah Science Technology and Research (USTAR) initiative of the State of Utah. FTIR spectroscopy performed by Bo Hu and Tianpin Wu at the Advanced Photon Source, an Office of Science User Facility operated for the U.S. Department of Energy (DOE) Office of Science by Argonne National Laboratory, was supported by the U.S. DOE under Contract No. DE-AC02-06CH11357. A grant of computer time from the Department of Defense High Performance Computing Modernization Program on the five DoD Supercomputing Resource Centers (Air Force Research Laboratory, Army Research Laboratory, Engineer Research and Development Center, Navy, and Maui High Performance Computing Center) is gratefully acknowledged.

References

- (1) Ivanov, G. V.; Tepper, F. In *"Activated" Aluminum as a Stored Energy Source for Propellants*, Begell House: pp 636-645.
- (2) Mench, M. M.; Yeh, C. L.; Kuo, K. K., Propellant Burning Rate Enhancement And Thermal Behavior Of Ultra-Fine Aluminum Powders (Alex). *Int. Annu. Conf. ICT* **1998**, *29th*, 30.1-30.15.
- (3) MacKenzie, S., *Handbook of Aluminum*. Marcel Decker, Inc.: New York, Basel, 2003; Vol. 1, p 1309.
- (4) Galfetti, L.; Luca, L. T. D.; Severini, F.; Meda, L.; Marra, G.; Marchetti, M.; Regi, M.; Bellucci, S., Nanoparticles For Solid Rocket Propulsion. *J. Phys.: Condensed Matter* **2006**, *18*, S1991-S2005.

- (5) Armstrong, R. W.; Baschung, B.; Booth, D. W.; Samirant, M., Enhanced Propellant Combustion with Nanoparticles. *Nano Lett.* **2002**, *3*, 253-255.
- (6) Lynch, P.; Fiore, G.; Krier, H.; Glumac, N., Gas-Phase Reaction in Nanoaluminum Combustion. *Combust. Sci. Technol.* **2010**, *182*, 842-857.
- (7) Connell, T. L., Jr.; Risha, G. A.; Yetter, R. A.; Young, G.; Sundaram, D. S.; Yang, V., Combustion Of Alane And Aluminum With Water For Hydrogen And Thermal Energy Generation. *Proc. Combust. Inst.* **2011**, *33*, 1957-1965.
- (8) Allen, D.; Krier, H.; Glumac, N., Heat Transfer Effects In Nano-Aluminum Combustion At High Temperatures. *Combust. Flame* **2014**, *161*, 295-302.
- (9) Risha, G. A.; Son, S. F.; Yetter, R. A.; Yang, V.; Tappan, B. C., Combustion Of Nano-Aluminum And Liquid Water. *Proc. Combust. Inst.* **2007**, *31*, 2029-2036.
- (10) Yetter, R. A.; Risha, G. A.; Son, S. F., Metal Particle Combustion And Nanotechnology. *Proc. Combust. Inst.* **2009**, *32*, 1819-1838.
- (11) Sundaram, D. S.; Yang, V.; Huang, Y.; Risha, G. A.; Yetter, R. A., Effects Of Particle Size And Pressure On Combustion Of Nano-Aluminum Particles And Liquid Water. *Combust. Flame* **2013**, *160*, 2251-2259.
- (12) Wang, H.; Jian, G.; Yan, S.; DeLisio, J. B.; Huang, C.; Zachariah, M. R., Electrospray Formation of Gelled Nano-Aluminum Microspheres with Superior Reactivity. *ACS Appl. Mater. Interfaces* **2013**, *5*, 6797-6801.
- (13) Nabiyouni, G.; Fesharaki, M. J.; Mozafari, M.; Amighian, J., Characterization and Magnetic Properties of Nickel Ferrite Nanoparticles Prepared by Ball Milling Technique. *Chin. Phys. Lett.* **2010**, *27*, 126401.

- (14) Li, S.; Yan, W.; Zhang, W.-x., Solvent-Free Production Of Nanoscale Zero-Valent Iron (nZVI) With Precision Milling. *Green Chem.* **2009**, *11*, 1618-1626.
- (15) Oleszak, D.; Shingu, P. H., Nanocrystalline Metals Prepared By Low Energy Ball Milling. *J. Appl. Phys.* **1996**, *79*, 2975-2980.
- (16) Perez, J. P. L.; McMahon, B. W.; Schneider, S.; Boatz, J. A.; Hawkins, T. W.; McCrary, P. D.; Beasley, P. A.; Kelley, S. P.; Rogers, R. D.; Anderson, S. L., Exploring the Structure of Nitrogen-Rich Ionic Liquids and Their Binding to the Surface of Oxide-Free Boron Nanoparticles. *J. Phys. Chem. C* **2013**, *117*, 5693–5707.
- (17) Sepelak, V.; Duvel, A.; Wilkening, M.; Becker, K.-D.; Heitjans, P., Mechanochemical Reactions And Syntheses Of Oxides. *Chem. Soc. Rev.* **2013**, *42*, 7507-7520.
- (18) Rehbinder, P. A., Reports at the VI Conference of Russian Physicists. 1928
- (19) Barnoush, A.; Vehoff, H., Hydrogen Embrittlement Of Aluminum In Aqueous Environments Examined By In Situ Electrochemical Nanoindentation. *Scr. Mater.* **2008**, *58*, 747-750.
- (20) Gutman, E. M., *Mechanochemistry of Materials*. Cambridge International Science Publishing: Cambridge, 1998;
- (21) Bowmaker, G. A., Solvent-Assisted Mechanochemistry. *Chem. Commun. (Cambridge, U. K.)* **2013**, *49*, 334-348.
- (22) Frišćić, T.; Jones, W., Recent Advances in Understanding the Mechanism of Cocrystal Formation via Grinding. *Cryst. Growth Des.* **2009**, *9*, 1621-1637.

- (23) Friščić, T.; Trask, A. V.; Jones, W.; Motherwell, W. D. S., Screening For Inclusion Compounds And Systematic Construction Of Three-Component Solids By Liquid-Assisted Grinding. *Angew. Chem., Int. Ed.* **2006**, *45*, 7546-7550.
- (24) Syugaev, A. V.; Maratkanova, A. N.; Shakov, A. A.; Nelyubov, A. V.; Lomayeve, S. F., Surface Modification Of Iron Particles With Polystyrene And Surfactants Under High-Energy Ball Milling. *Surf. Coat. Technol.* **2013**, *236*, 429-437.
- (25) Wu, H.; Zhao, W.; Hu, H.; Chen, G., One-Step In Situ Ball Milling Synthesis Of Polymer-Functionalized Graphene Nanocomposites. *J. Mater. Chem.* **2011**, *21*, 8626.
- (26) McMahon, B. W.; Perez, J. P. L.; Yu, J.; Boatz, J. A.; Anderson, S. L., Synthesis of Nanoparticles from Malleable and Ductile Metals Using Powder-Free, Reactant-Assisted Mechanical Attrition. *ACS Appl. Mater. Interfaces* **2014**, *6*, 19579–19591.
- (27) Huot, J.; Ravnsbæk, D. B.; Zhang, J.; Cuevas, F.; Latroche, M.; Jensen, T. R., Mechanochemical Synthesis Of Hydrogen Storage Materials. *Prog. Mater. Sci.* **2013**, *58*, 30-75.
- (28) Leng, H. Y.; Ichikawa, T.; Isobe, S.; Hino, S.; Hanada, N.; Fujii, H., Desorption Behaviours From Metal-N-H Systems Synthesized By Ball Milling. *J. Alloys Compd.* **2005**, *404-406*, 443-447.
- (29) Wang, P.; Orimo, S.; Tanabe, K.; Fujii, H., Hydrogen In Mechanically Milled Amorphous Boron. *J. Alloys Compd.* **2003**, *350*, 218-221.
- (30) Perez, J. P. L.; McMahon, B. W.; Yu, J.; Schneider, S.; Boatz, J. A.; Hawkins, T. W.; McCrary, P. D.; Flores, L. A.; Rogers, R. D.; Anderson, S. L., Boron Nanoparticles with High Hydrogen Loading: Mechanism for B–H Binding and Potential for Improved Combustibility and Specific Impulse. *ACS Appl. Mater. Interfaces* **2014**, *6*, 8513-8525.

- (31) Perez, J. P. L.; Yu, J.; Sheppard, A. J.; Chambreau, S. D.; Vaghjiani, G. L.; Anderson, S. L., Binding of Alkenes and Ionic Liquids to B-H Functionalized Boron Nanoparticles: Creation of Particles with Controlled Dispersibility and Minimal Surface Oxidation. *ACS Appl. Mater. Interfaces* **2015**, (published on line May 2015).
- (32) Gallardo, I.; Pinson, J.; Vila, N., Spontaneous Attachment Of Amines To Carbon And Metallic Surfaces. *J. Phys. Chem. B* **2006**, *110*, 19521-10529.
- (33) Kasai, P. H.; Himmel, H. J., Insertion Of The Al Atom Into The NH₃ Molecule: Semiempirical SCF MO And Matrix Isolation ESR Study. *J. Phys. Chem. A* **2002**, *106*, 6765-6774.
- (34) Joly, H. A.; Newton, T.; Myre, M., Activation of C-Cl by Ground-State Aluminum Atoms: An EPR and DFT Investigation. *Phys. Chem. Chem. Phys.* **2012**, *14*, 367-374.
- (35) Joly, H. A.; Ashley, J.; Levesque, M. Y.; Rank, J. P., Electron Paramagnetic Resonance Study of the Mononuclear Al Species Formed in the Reaction of Al Atoms and Cyclopropylamine at 77 K in an Adamantane Matrix. *J. Phys. Chem. A* **2006**, *110*, 3911-3919.
- (36) Jones, D. E. G.; Turcotte, R.; Fouchard, R. C.; Kwok, Q. S. M.; Turcotte, A.-M.; Abdel-Qader, Z., Hazard Characterization Of Aluminum Nanopowder Compositions. *Propellants, Explos., Pyrotech.* **2003**, *28*, 120-131.
- (37) Polunina, I. A.; Roldugin, V. I.; Kolesnikova, T. P.; Buryak, A. K.; Ulyanov, A. V.; Polunin, K. E., Interaction Between Carboxylic Modifiers And Nanodispersed Aluminium. *Colloids Surf., A* **2004**, *239*, 85-93.

- (38) Davies, P. R.; Newton, N. G., The Chemisorption And Decomposition Of Pyridine And Ammonia At Clean And Oxidised Al(111) Surfaces. *Surf. Sci.* **2003**, *546*, 149-158.
- (39) Zhao, Y.; Truhlar, D. G., The M06 Suite of Density Functionals for Main Group Thermochemistry, Thermochemical Kinetics, Noncovalent Interactions, Excited States, and Transition Elements: Two New Functionals and Systematic Testing of Four M06-Class Functionals and 12 Other Functionals. *Theor. Chem. Acc.* **2008**, *120*, 215-241.
- (40) McLean, A. D.; Chandler, G. S., Contracted Gaussian Basis Sets For Molecular Calculations. I. Second Row Atoms, Z=11-18. *J. Chem. Phys.* **1980**, *72*, 5639-5648.
- (41) Francl, M. M.; Pietro, W. J.; Hehre, W. J.; Binkley, J. S.; Gordon, M. S.; DeFrees, D. J.; Pople, J. A., Self-Consistent Molecular Orbital Methods. XXIII. A Polarization-Type Basis Set For Second-Row Elements. *J. Chem. Phys.* **1982**, *77*, 3654-3665.
- (42) Clark, T.; Chandrasekhar, J.; Spitznagel, G. W.; Schleyer, P. v. R., Efficient Diffuse Function-Augmented Basis Sets For Anion Calculations. Iii. The 3-21+G Basis Set For First-Row Elements, Li-F. *J. Comput. Chem.* **1983**, *4*, 294-301.
- (43) Krishnan, R.; Binkely, J. S.; Seeger, R.; Pople, J. A., Self-Consistent Molecular Orbital Methods. Xx. A Basis Set For Correlated Wave Functions. *J. Chem. Phys.* **1980**, *72*, 650-654.
- (44) Gonzalez, C.; Schlegel, H. B., An Improved Algorithm For Reaction Path Following. *J. Chem. Phys.* **1989**, *90*, 2154-2161.
- (45) Schmidt, M. W.; Baldridge, K. K.; Boatz, J. A.; Elbert, S. T.; Gordon, M. S.; Jensen, J. H.; Koseki, S.; Matsunaga, N.; Nguyen, K. A.; Su, S.; Windus, T. L.; Dupuis,

M.; Montgomery, J., A General Atomic and Molecular Electronic Structure System. *J. Comput. Chem.* **1993**, *14*, 1347-1363.

(46) Gordon, M. S.; Schmidt, M. W., *Theory and Applications of Computational Chemistry: The First Forty Years*. Elsevier (Amsterdam): 2005;

(47) Bockmon, B. S.; Pantoya, M. L.; Son, S. F.; Asay, B. W.; Mang, J. T.,
Combustion velocities and propagation mechanisms of metastable interstitial composites. *J. Appl. Phys.* **2005**, *98*, 064903.

(48) Henderson, M. A., An HREELS and TPD Study of Water on TiO₂(110): The Extent Of Molecular Versus Dissociative Adsorption *Surf. Sci.* **1996**, *355*, 151-166.

(49) Moulder, J. F.; Stickle, W. F.; Sobol, P. E.; Bomben, K. D., *Handbook of X-Ray Photoelectron Spectroscopy*. Perkin-Elmer Corporation Eden Prairie, 1992; p 261.

(50) Powell, C. J.; Jablonski, A., *NIST Electron Effective Attenuation Length Database Version 1.3, SRD 82*. National Institute of Standards and Technology: Gaithersburg, MD, 2011;

(51) Balchev, I.; Minkovski, N.; Marinova, T.; Shipochka, M.; Sabotinov, N.,
Composition and Structure Characterization Of Aluminum After Laser Ablation. *Mater. Sci. Eng., B* **2006**, *135*, 108-112.

(52) Chenakin, S. P.; Prada Silvy, R.; Kruse, N., Effect of X-rays on the Surface Chemical State of Al₂O₃, V₂O₅, and Aluminovanadate Oxide. *J. Phys. Chem. B* **2005**, *109*, 14611-14618.

(53) Klopogge, J. T.; Duong, L. V.; Wood, B. J.; Frost, R. L., XPS Study Of The Major Minerals In Bauxite: Gibbsite, Bayerite And (Pseudo-)Boehmite. *J. Col. Interface Sci.* **2006**, *296*, 572-576.

- (54) Kwon, Y.-S.; Gromov, A. A.; Ilyin, A. P.; Rim, G.-H., Passivation Process For Superfine Aluminum Powders Obtained By Electrical Explosion Of Wires. *Appl. Sur. Sci.* **2003**, *211*, 57-67.
- (55) Laidani, N.; Vanzetti, L.; Anderle, M.; Basillais, A.; Boulmer-Leborgne, C.; Perriere, J., Chemical Structure Of Films Grown By AlN Laser Ablation: An X-Ray Photoelectron Spectroscopy Study. *Surf. Coatings Technol.* **1999**, *122*, 242-246.
- (56) Lewis, W. K.; Rosenberger, A. T.; Gord, J. R.; Crouse, C. A.; Harruff, B. A.; Fernando, K. A. S.; Smith, M. J.; Phelps, D. K.; Spowart, J. E.; Guliants, E. A.; Bunker, C. E., Multispectroscopic (FTIR, XPS, and TOFMS-TPD) Investigation of the Core-Shell Bonding in Sonochemically Prepared Aluminum Nanoparticles Capped with Oleic Acid. *J. Phys. Chem. C* **2010**, *114*, 6377–6380.
- (57) Schoser, S.; Bräuchle, G.; Forget, J.; Kohlhof, K.; Weber, T.; Voigt, J.; Rauschenbach, B., XPS Investigation Of AlN Formation In Aluminum Alloys Using Plasma Source Ion Implantation. *Surf. Coatings Technol.* **1998**, *103-104*, 222-226.
- (58) Zähr, J.; Oswald, S.; Türpe, M.; Ullrich, H. J.; Füssel, U., Characterisation Of Oxide And Hydroxide Layers On Technical Aluminum Materials Using XPS. *Vacuum* **2012**, *86*, 1216-1219.
- (59) Mullins, W. M.; Averbach, B. L., The Electronic Structure Of Anodized And Etched Aluminum Alloy Surfaces. *Surf. Sci.* **1988**, *206*, 52-60.
- (60) Taylor, J. A.; Rabalais, J. W., Reaction Of Nitrogen (N_2^+) Beams With Aluminum Surfaces. *J. Chem. Phys.* **1981**, *75*, 1735-45.
- (61) Baker, C. C.; Ceylan, A.; Shah, S. I., Reactive Gas Condensation Synthesis Of Aluminum Nitride Nanoparticles. *J. Nanosci. Nanotechnol.* **2006**, *6*, 146-150.

- (62) Affrossman, S.; MacDonald, S. M., Adsorption Modes of a Model Adhesive Resin, (Methylamino)ethanol, on Aluminum and Phosphated Aluminum Surfaces. *Langmuir* **1996**, *12*, 2090-2095.
- (63) Alexander, M. R.; Thompson, G. E.; Beamson, G., Characterization Of The Oxide/Hydroxide Surface Of Aluminium Using X-Ray Photoelectron Spectroscopy: A Procedure For Curve Fitting The O 1s Core Level. *Surf. Interface Anal.* **2000**, *29*, 468-477.
- (64) Rangan, S.; Bournel, F.; Gallet, J. J.; Kubsky, S.; Le Guen, K.; Dufour, G.; Rochet, F.; Sirotti, F.; Carniato, S.; Ilakovac, V., Experimental and Theoretical NEXAFS/XPS Study Of The Room-Temperature Adsorption Of Acetonitrile On Si(001)-2×1. *Phys. Rev. B: Condens. Matter Mater. Phys.* **2005**, *71*, 165319/1-165319/11.
- (65) Adenier, A.; Chehimi, M. M.; Gallardo, I.; Pinson, J.; Vila, N., Electrochemical Oxidation of Aliphatic Amines and Their Attachment to Carbon and Metal Surfaces. *Langmuir* **2004**, *20*, 8243-8253.
- (66) Russat, J., Characterization Of Polyamic Acid/Polyimide Films In The Nanometric Thickness Range From Spin-Deposited Polyamic Acid. *Surf. Interface Anal.* **1988**, *11*, 414-420.
- (67) Kou, J.-p.; Lu, Y.-j.; Luo, X.-y.; Li, J.-z., Michael Addition of Amines to Activated Alkenes Promoted by Zn/NH₄Cl System *Chem. Res. Chin. Univ.* **2009**, *25*, 461-464.
- (68) Baláž, P.; Achimovičová, M.; Baláž, M.; Billik, P.; Cherkezova-Zheleva, Z.; Criado, J. M.; Delogu, F.; Dutková, E.; Gaffet, E.; Gotor, F. J.; Kumar, R.; Mitov, I.; Rojac, T.; Senna, M.; Streletskiik, A.; Wieczorek-Ciurowa, K., Hallmarks Of

Mechanochemistry: From Nanoparticles To Technology. *Chem. Soc. Rev.* **2013**, *42*, 7571-7637.

(69) Trefry, J. C.; Monahan, J. L.; Weaver, K. M.; Meyerhoefer, A. J.; Markopolous, M. M.; Arnold, Z. S.; Wooley, D. P.; Pavel, I. E., Size Selection and Concentration of Silver Nanoparticles by Tangential Flow Ultrafiltration for SERS-Based Biosensors. *J. Am. Chem. Soc.* **2010**, *132*, 10970-10972.

(70) Stein, S. E., director, IR and Mass Spectra. In *NIST Chemistry WebBook*, *NIST Standard Reference Database Number 69*, Mallard, W. G.; Linstrom, P. J., Eds. NIST Mass Spec Data Center, National Institute of Standards and Technology: Gaithersburg MD 20899 (<http://webbook.nist.gov>). 2000.

(71) Cao, X.; Hamers, R. J., Molecular And Dissociative Bonding Of Amines With The Si(111)-(7×7) Surface. *Surf. Sci.* **2003**, *523*, 241-251.

(72) Hansen, U.; Vogl, P.; Fiorentini, V., Quasiharmonic Versus Exact Surface Free Energies Of Al: A Systematic Study Employing A Classical Interatomic Potential. *Phys. Rev. B Condens. Matter Mater. Phys.* **1999**, *60*, 5055-5064.

(73) Vitos, L.; Ruban, A. V.; Skriver, H. L.; Kollar, J., The Surface Energy Of Metals. *Surf. Sci.* **1998**, *411*, 186-202.

(74) Kumikov, V. K.; Khokonov, K. B., On The Measurement Of Surface Free Energy And Surface Tension Of Solid Metals. *J. Appl. Phys.* **1983**, *54*, 1346-50.

(75) Wang, X.; Jia, Y.; Yao, Q.; Wang, F.; Ma, J.; Hu, X., The Calculation Of The Surface Energy Of High-Index Surfaces In Metals At Zero Temperature. *Surf. Sci.* **2004**, *551*, 179-188.

- (76) Kammeyer, C. W.; Whitman, D. R., Quantum Mechanical Calculation of Molecular Radii. I. Hydrides of Elements of Periodic Groups IV Through VII. *J. Chem. Phys.* **1972**, *56*, 4419-4421.
- (77) Watson, P. R.; Hove, M. A. V.; Hermann, K., Atlas of Surface Structures. *J. Phys. Chem. Ref. Data* **1994**, *Monograph 5*, 1-907.

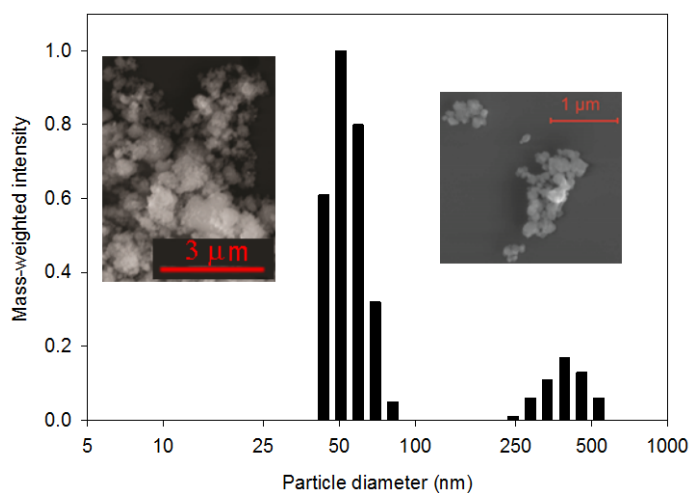


Fig. 1 Dynamic light scattering measurement for ammonia milled aluminum nanoparticles in acetonitrile suspension. Insets: SEM image of the aluminum nanoparticles.

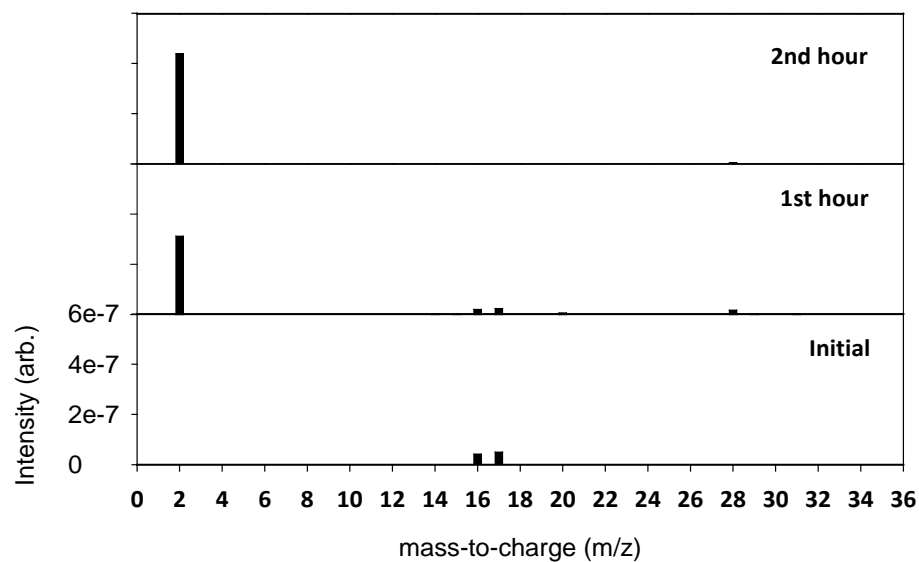


Fig. 2 Mass spectrometry of the headspace before and after one and two hours of milling aluminum in an ammonia atmosphere. Each spectrum was corrected for the instrument background, and the spectra are plotted on the same intensity scale.

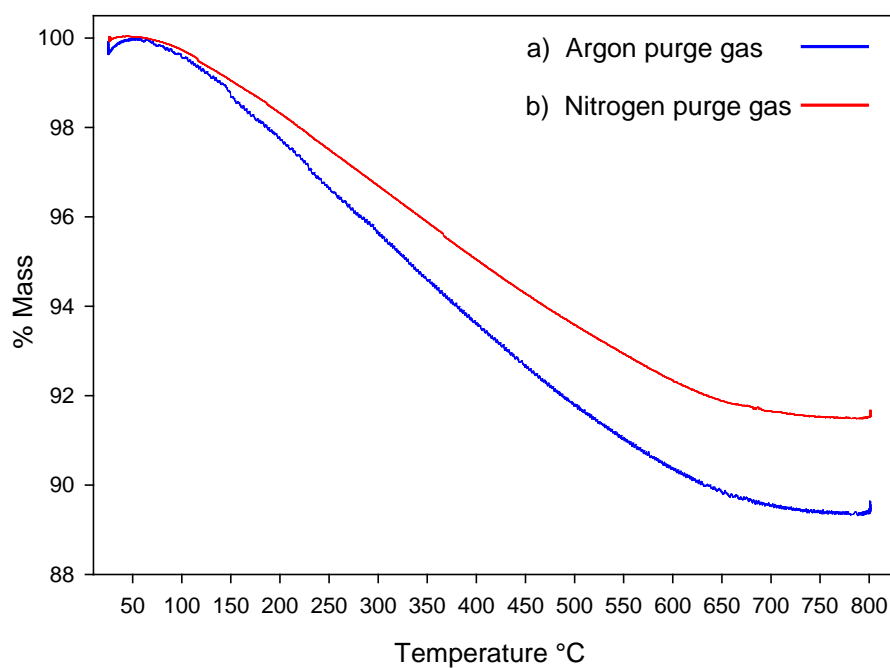


Fig. 3 Thermogravimetric analysis of ammonia milled aluminum nanoparticles transferred to a TGA housed in a N₂-filled glove box, with different exposures to air before analysis

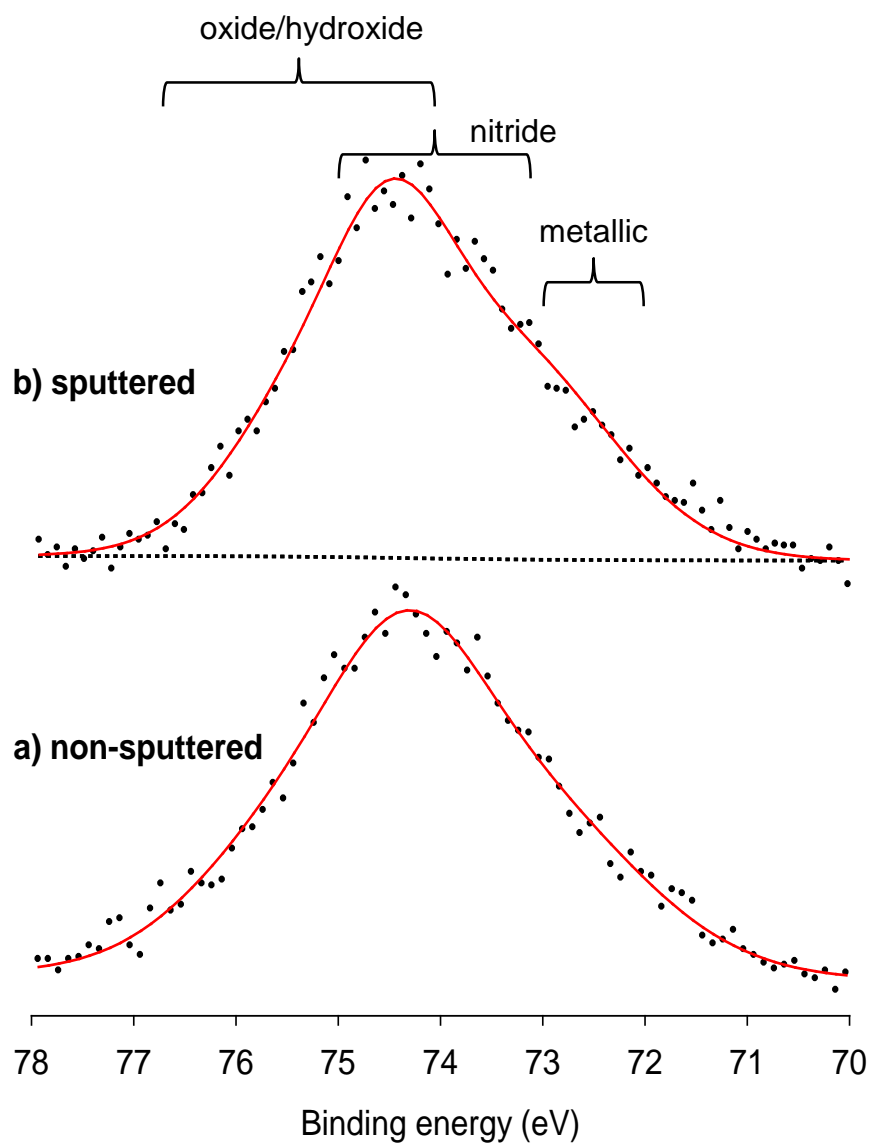


Fig. 4. High resolution XPS Al 2p region scan of aluminum nanoparticles milled for 5 hours in 55 psia of ammonia (NH_3): a) non-sputtered b) < 5 sec argon sputtering

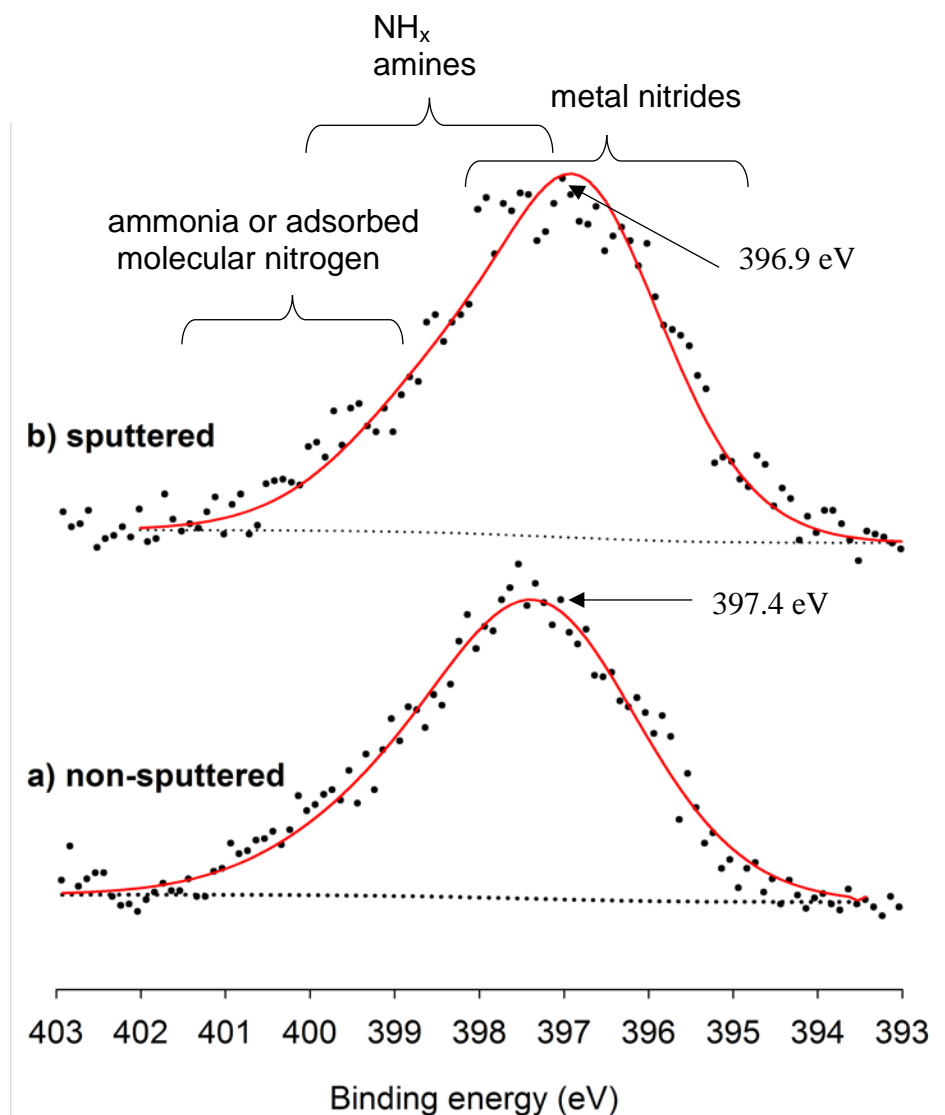


Fig. 5 High resolution XPS N 1s region scan of aluminum nanoparticles milled for 5 hours in 55 psia of ammonia (NH₃): a) non-sputtered b) < 5 sec argon sputtering Note: samples transferred to instrument under argon.

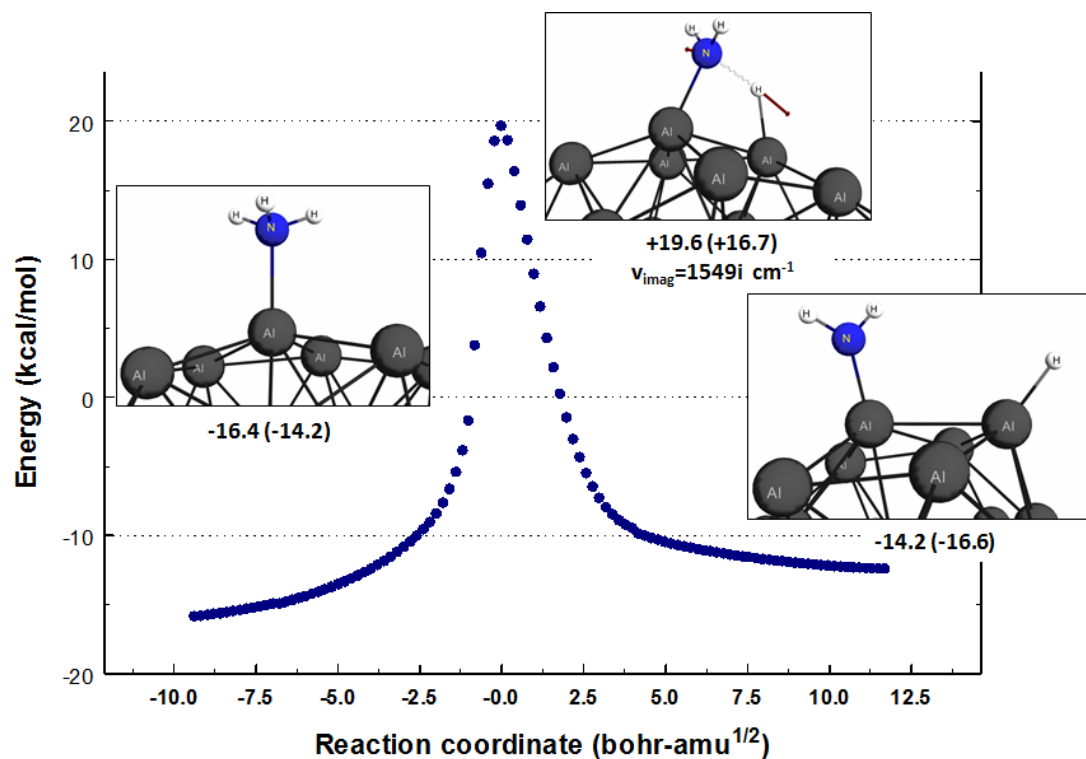


Fig. 6. IRC (blue dots) of chemisorbed NH₃ undergoing N-H fragmentation to form chemisorbed NH₂ + H, excluding zero point energy (ZPE) corrections. The energies, in kcal mol⁻¹, of the stationary points (reactant, saddle point, and product) are relative to separated NH₃ + Al₈₀. ZPE-corrected energies are given in parentheses. A portion of the Al₈₀ cluster has been cropped to show the chemisorbed fragments in greater detail.

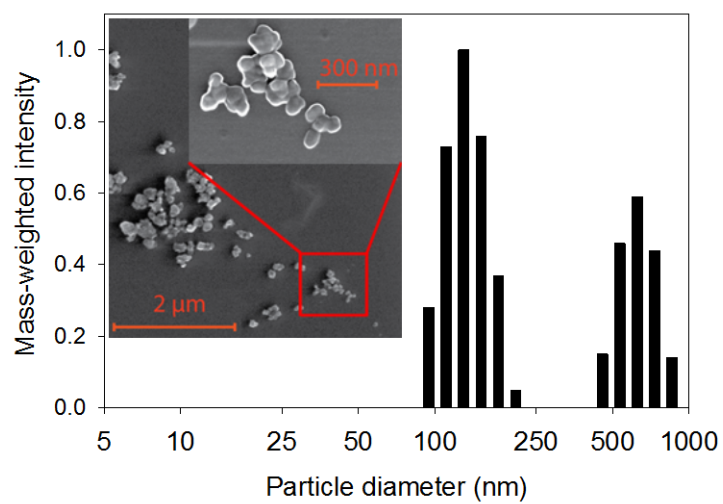


Fig. 7 Dynamic light scattering measurement for MMA-milled aluminum particles in acetonitrile suspension. Inset: SEM image of particles.

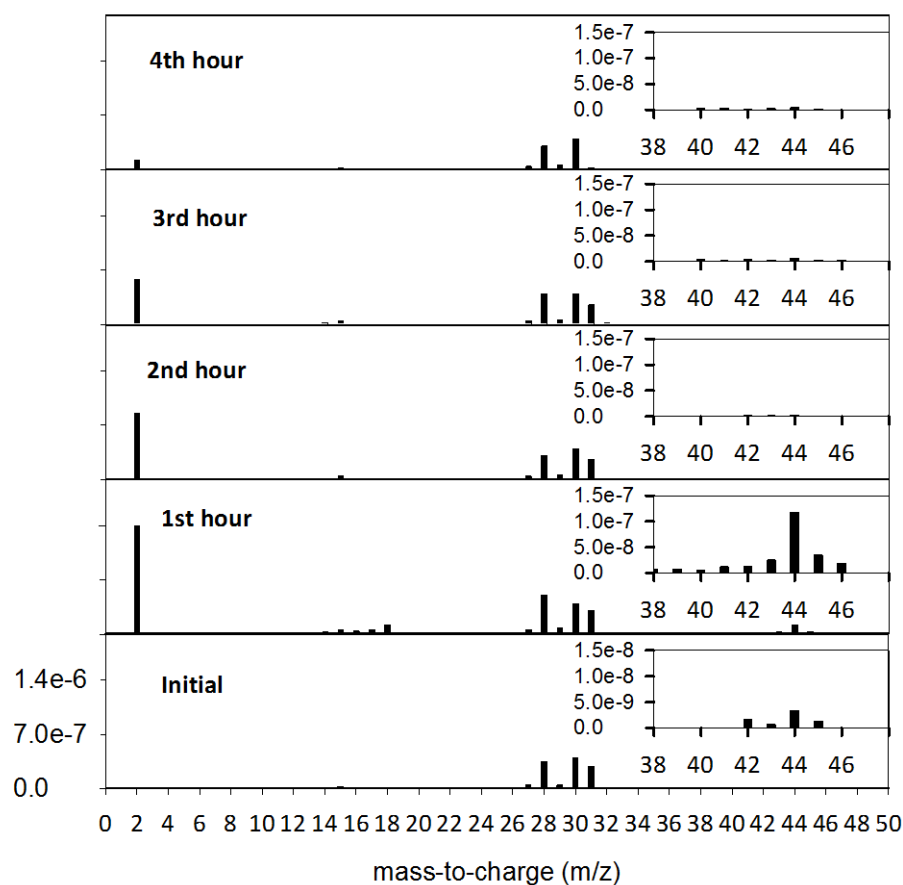


Fig. 8. Mass spectrometric analysis of the headspace during milling of aluminum in MMA. Note that the jar was evacuated and refilled with MMA prior to each hours milling. All spectra are scaled to constant intensity of $m/z = 30$

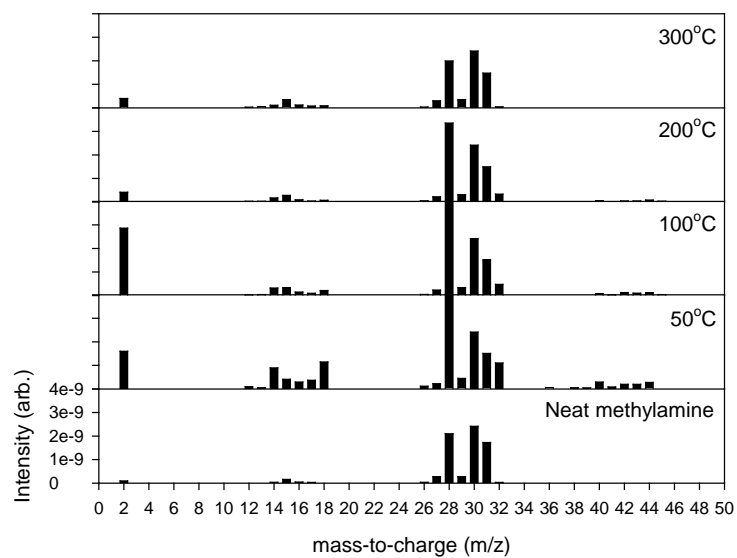


Fig. 9 Thermal desorption mass spectral analysis of MMA-milled aluminum particles

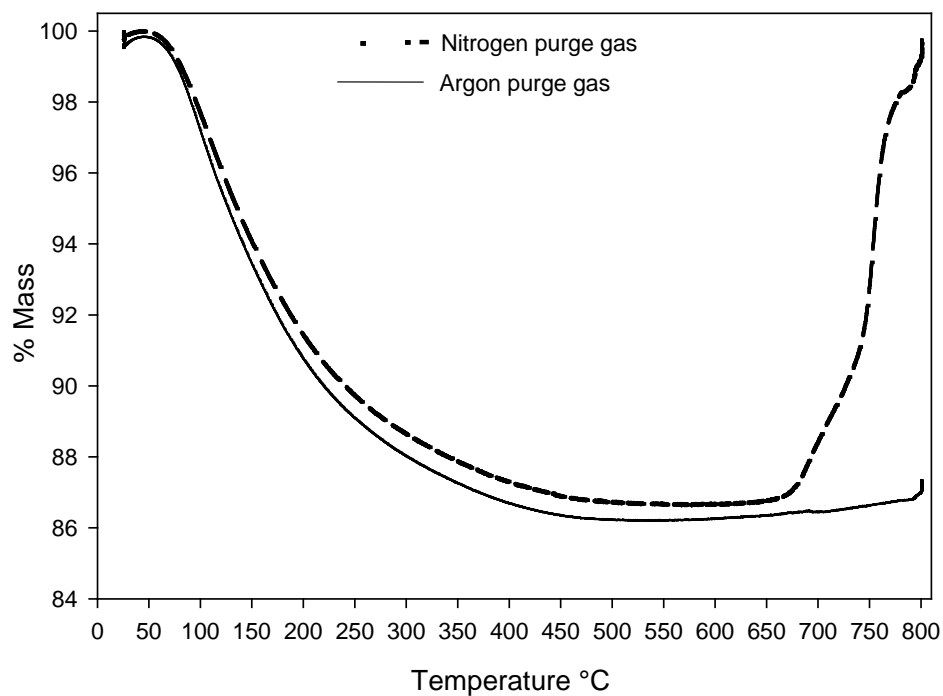


Fig. 10. Thermogravimetric analysis of methylamine milled aluminum nanoparticles transferred to a TGA housed in a N₂-filled glove box.

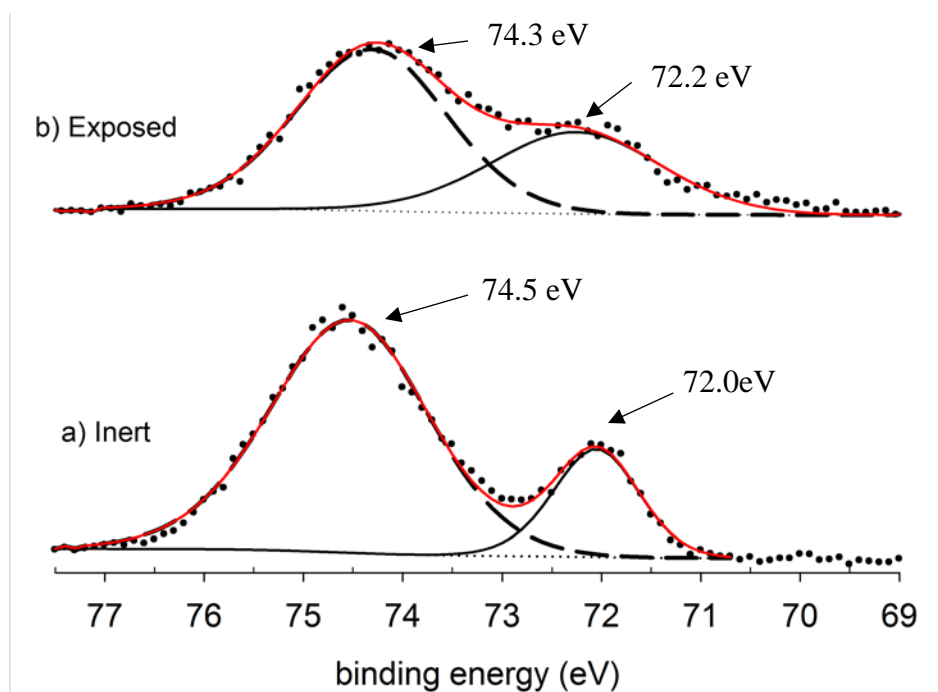


Fig. 11. High resolution X-Ray photoelectron Al 2p region scan of particles milled in methylamine for 4 hours, and transferred to the XPS instrument under argon. a) As-transfer b) exposed to air

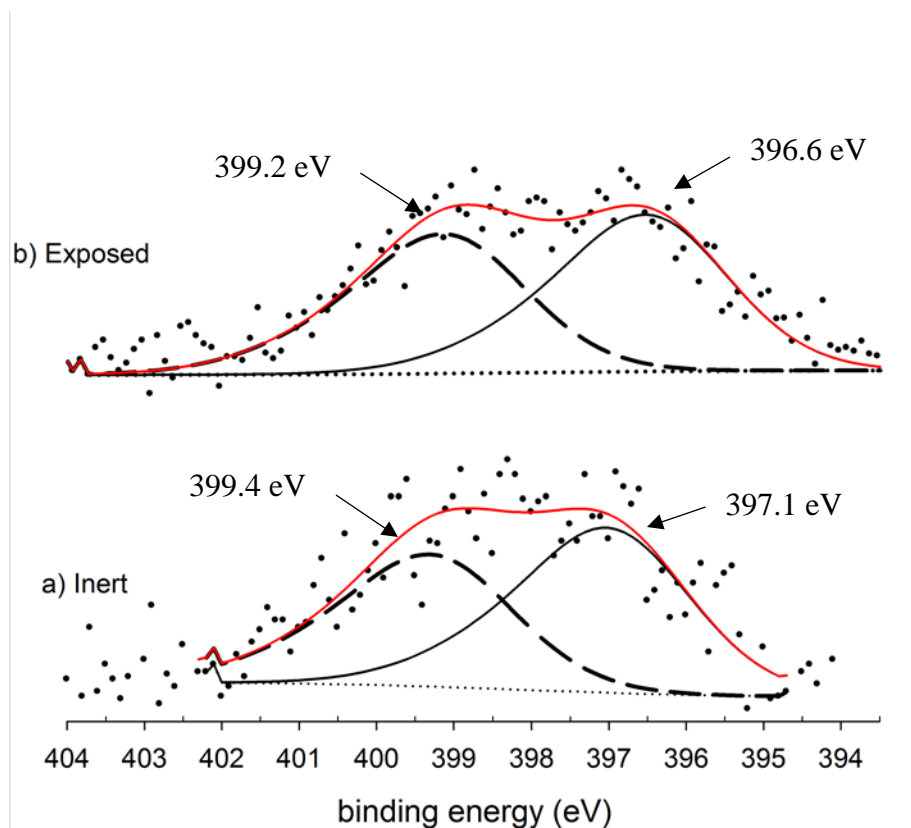


Fig. 12. High resolution X-Ray photoelectron N 1s region scan of particles milled in methylamine for 4 hours, pressed into a pellet, and transferred to the XPS instrument under argon: a) as transferred in inert atmosphere, b) exposed to air

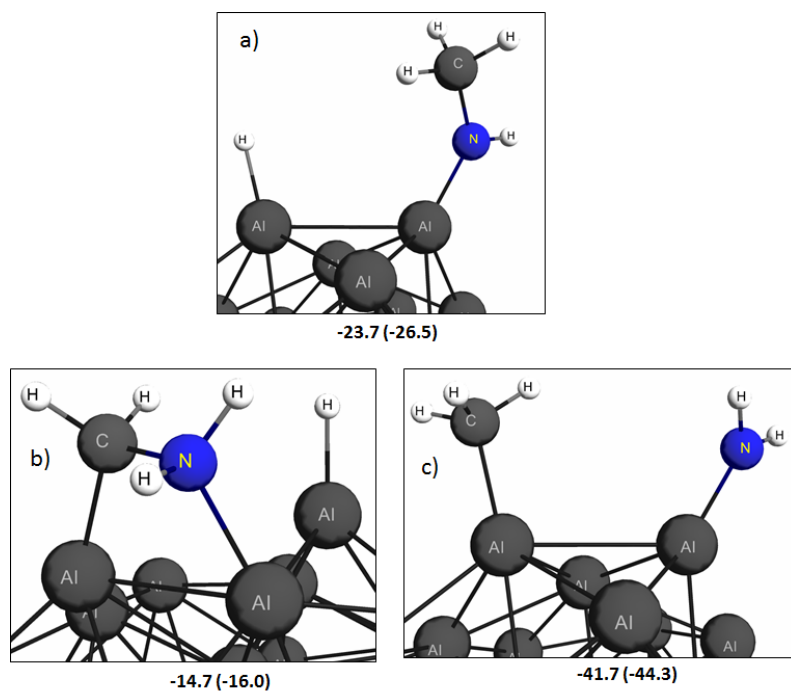


Fig. 13. DFT optimized structures of products resulting from bond dissociation of methylamine chemisorbed on Al_{80} . Chemisorbed products following N-H bond scission (panel a), C-H bond scission (panel b), and C-N bond scission (panel c.) Binding energies are relative $\text{CH}_3\text{NH}_2 + \text{Al}_{80}$. ZPE-corrected energies are given in parentheses. Portions of the Al_{80} cluster have been cropped to show the chemisorbed fragments in greater detail.

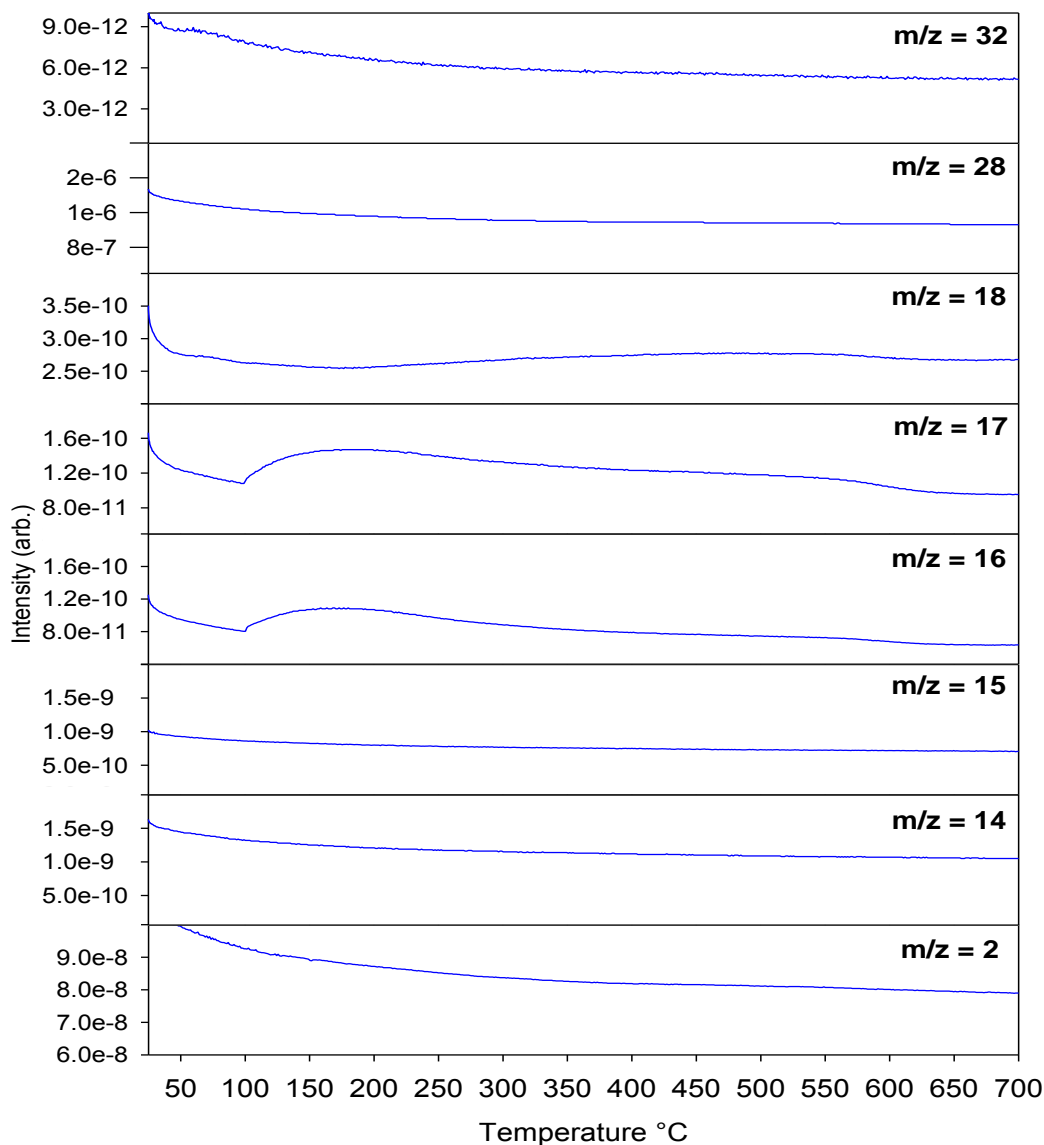


Fig. S1. Temperature dependence of the mass spectral intensities during TGA (in argon atmosphere) for NH_3 -milled aluminum nanoparticles, which were transferred under argon to a TGA instrument housed in a N_2 glove box. Due to the experimental setup, when the sampling port to the mass spectrometer is opened there is a pressure burst, and as a result all masses have a decaying baseline reflecting pump down of the ion source. Desorption signals are seen as positive excursions from this decaying baseline. Because of differences in background signal the intensity scale varies and is labeled for each spectrum. The background signal for all masses was observed to decrease slowly after the mass spectral sampling was started, however, only a few masses showed evidence for intensity increases in the 100-600 °C range where mass loss was observed (Fig. 3, main manuscript). Masses 17 and 16 both show a desorption feature between 100 and 600 °C with intensities matching those expected for ionization of ammonia. There was also a feature for mass 18 in the 250 – 600 °C range, suggesting water desorption, which would also contribute a small fraction of the mass 17 signal in this temperature range.

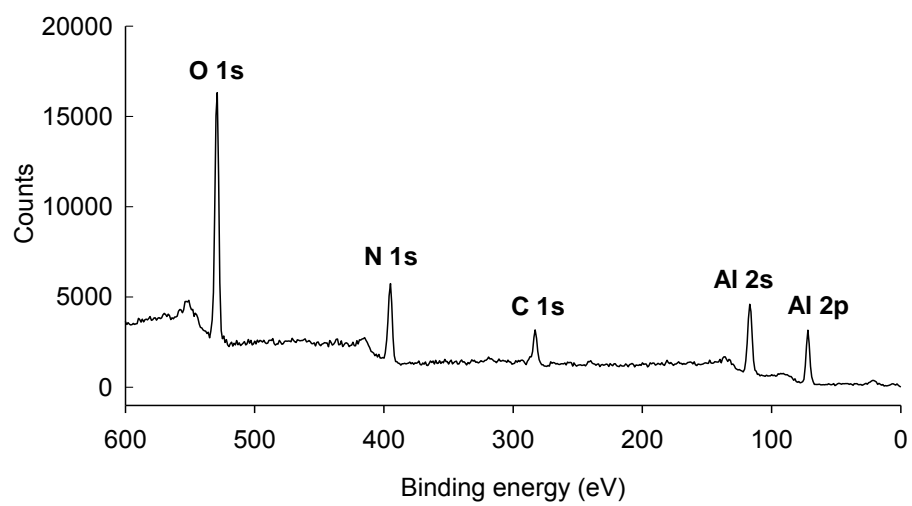


Fig. S2 XPS Survey scan of non-sputtered, ammonia-milled aluminum nanoparticles

Three peaks are fitted to this carbon 1s spectrum. Since this sample is milled in neat ammonia, the only sources for carbon are from air exposure, and contamination in the milling vessel. The lid of the milling vessel is stainless steel and the balls are tungsten carbide. There is evidence of wear on the lid of the vessel over the hundreds of hours of usage. It is reasonable that there could be a small amount of carbon contamination associated with the milling process, but there is no evidence of other likely contaminants.

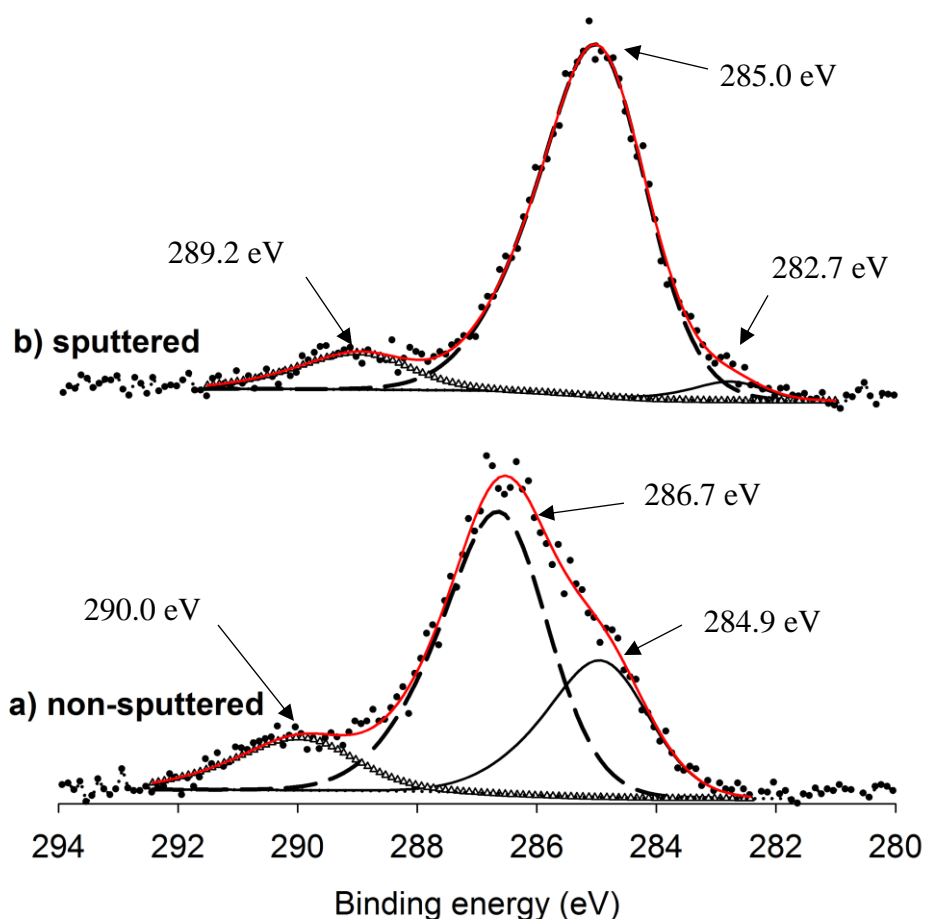


Fig. S3 High resolution XPS C 1s region scan of aluminum nanoparticles milled for 5 hours in 55 psia of ammonia (NH₃): a) non-sputtered b) < 5 sec argon sputtering Note: samples transferred to instrument under argon.

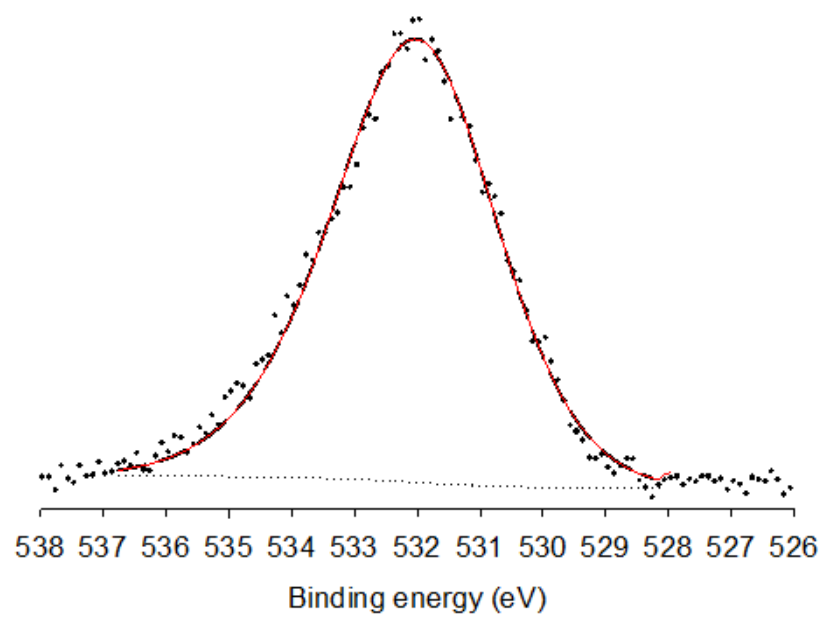


Fig. S4 High resolution XPS O 1s region scan of aluminum nanoparticles milled for 5 hours in ammonia (NH₃).

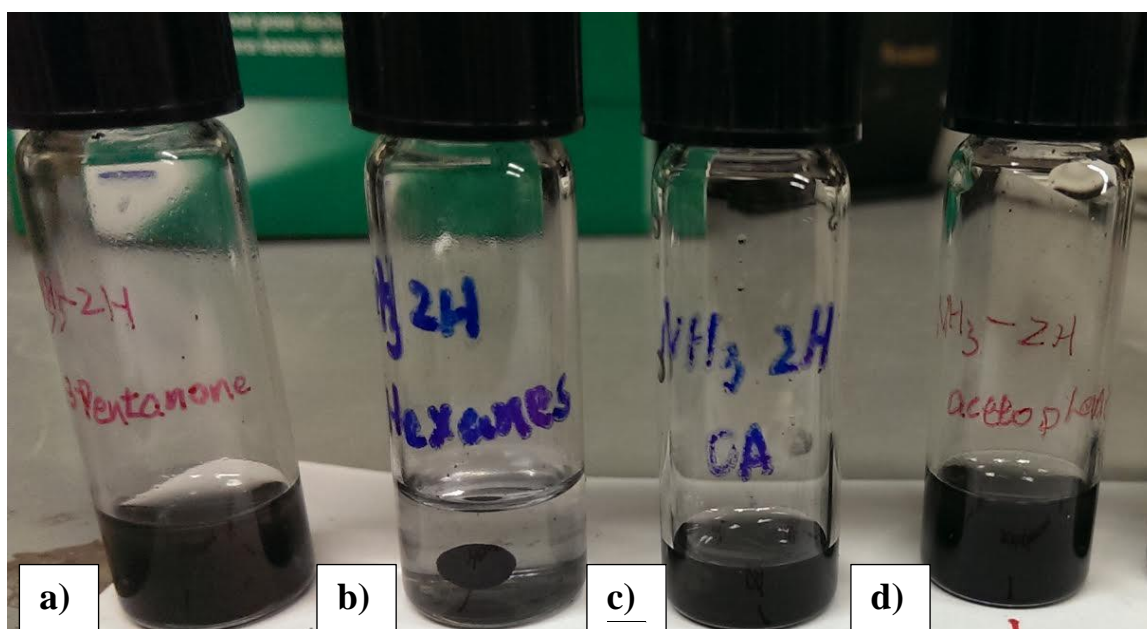


Fig. S5 Image of ketone functionalized, ammonia milled aluminum nanoparticles suspensions a) 3-pentanone functionalized, ammonia milled particles in hexanes b) as-milled ammonia milled particles in hexanes c) oleic acid functionalized, ammonia milled particles in hexanes d) acetophenone functionalized, ammonia milled particles

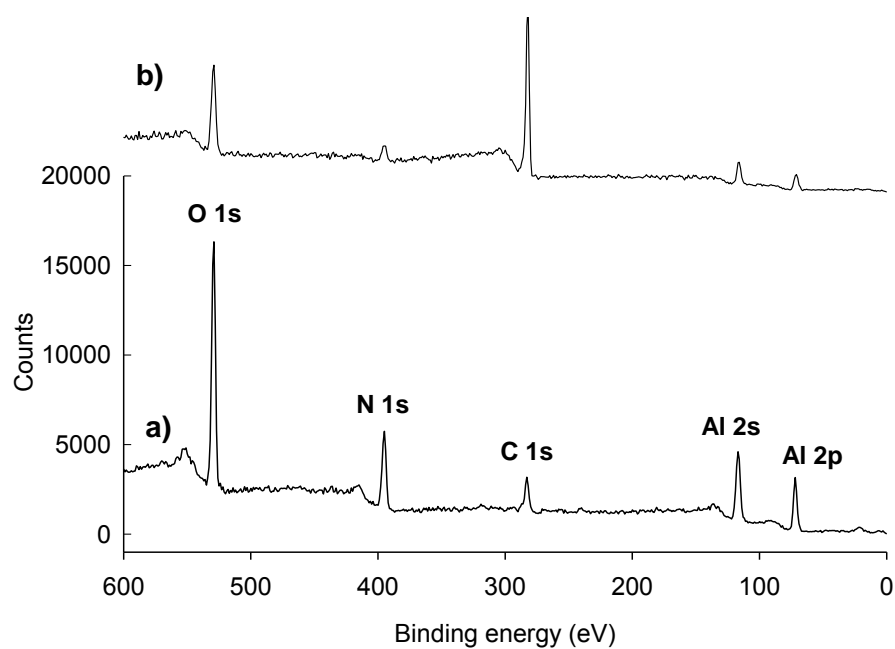


Fig. S6. X-ray photoelectron survey spectrum of ammonia milled aluminum nanoparticles functionalized with acetophenone Note: this survey scan has not been argon sputtered

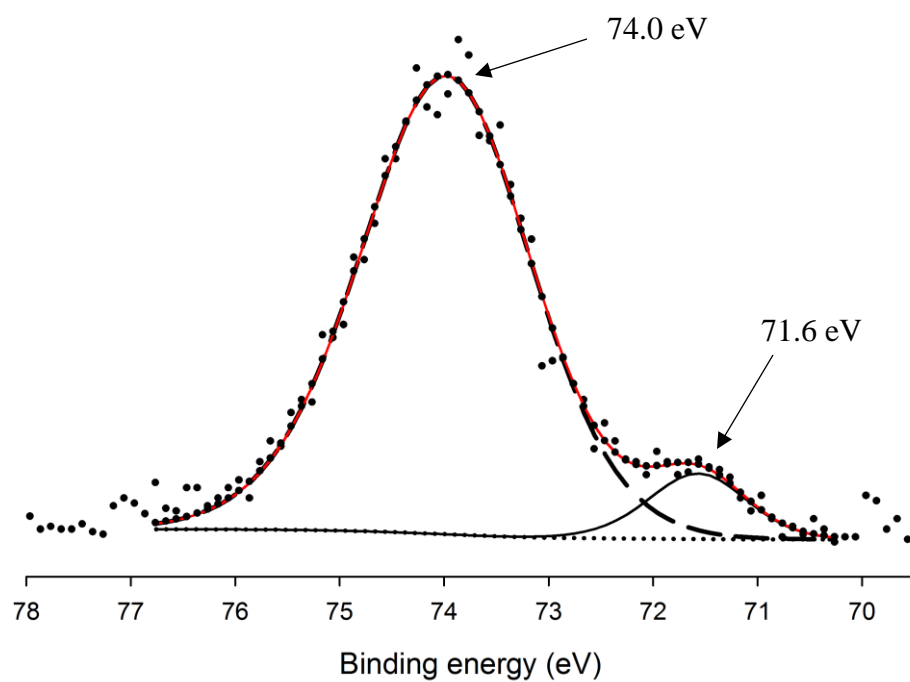


Fig. S7 High resolution X-Ray photoelectron Al 2p region scan of particles milled in ammonia for 5 hours and subsequently functionalized with acetophenone

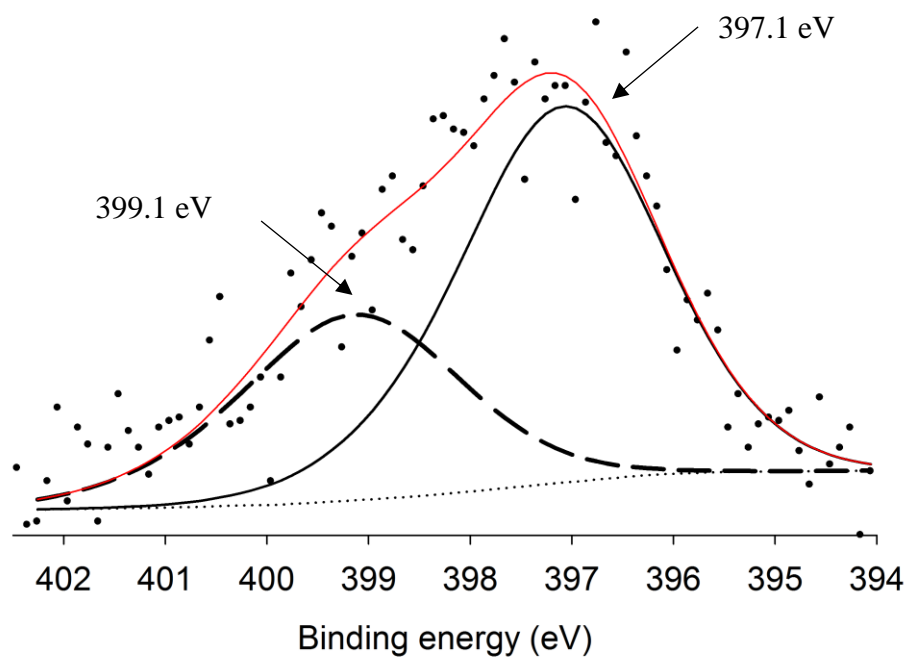


Fig. S8 High resolution X-Ray photoelectron N 1s region scan of particles milled in ammonia for 5 hours and subsequently functionalized with acetophenone

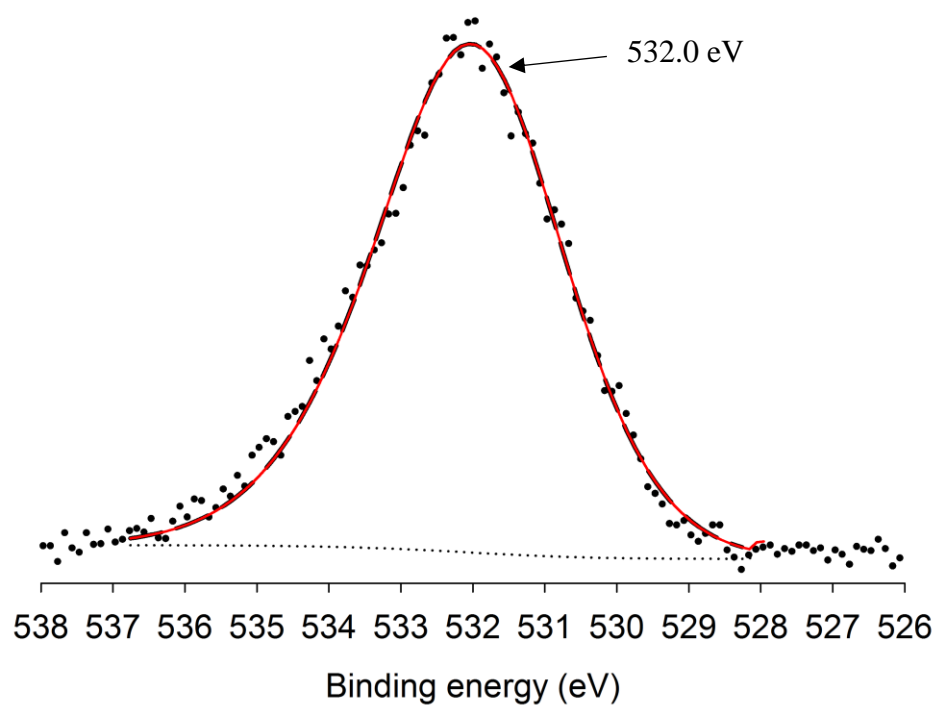


Fig. S9 High resolution X-Ray photoelectron O 1s region scan of particles milled in ammonia for 5 hours and subsequently functionalized with acetophenone

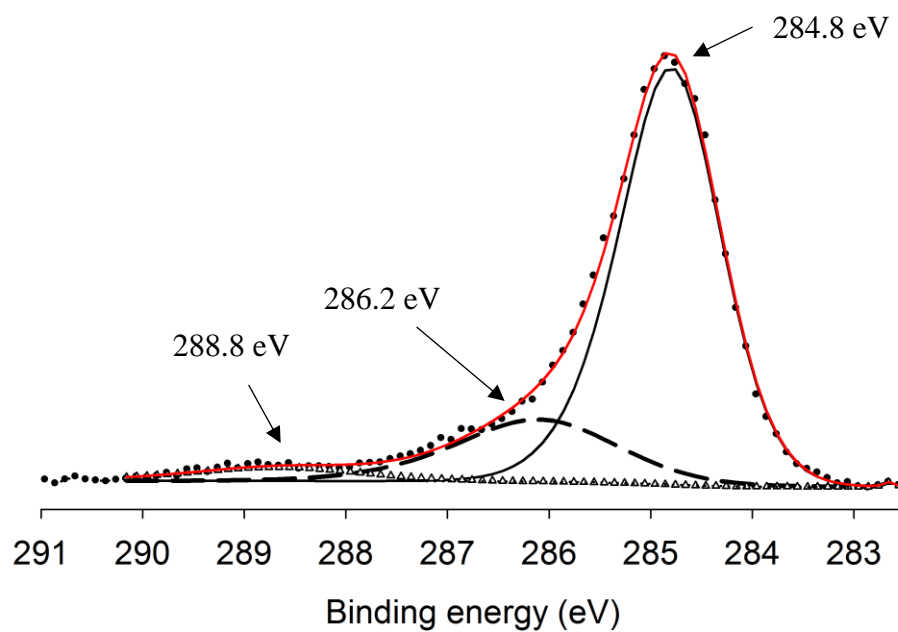


Fig. S10 High resolution X-Ray photoelectron C 1s region scan of particles milled in ammonia for 5 hours and subsequently functionalized with acetophenone

Description of DFT results for $\text{NH}_3 + \text{Al}_{80}$: Ammonia forms a weak dative bond to the surface of the Al_{80} cluster, henceforth denoted as $\text{H}_3\text{N}:\text{Al}_{80}$. In order to assess the variability of the dative binding energies as a function of specific binding site, four distinct configurations of NH_3 chemisorbed to Al_{80} were computed. These local minima have binding energies ranging from 8 to 16 kcal mol⁻¹, relative to separated $\text{Al}_{80} + \text{NH}_3$, and are shown in Figure S11.

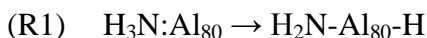
As an initial investigation into the potential chemical reactivity of $\text{H}_3\text{N}:\text{Al}_{80}$, the energetics of N-H bond dissociation and subsequent covalent binding of the resulting NH_2 and H fragments to Al_{80} , denoted as $\text{NH}_2\text{-Al}_{80}\text{-H}$, were computed. Several local minima in which the NH_2 and H moieties are chemisorbed on the surface of Al_{80} were calculated and found to be bound by 17 to 30 kcal mol⁻¹, relative to separated $\text{NH}_3 + \text{Al}_{80}$, and are shown in Figure S12. The greater stability of $\text{NH}_2\text{-Al}_{80}\text{-H}$ (17 to 30 kcal mol⁻¹) relative to $\text{H}_3\text{N}:\text{Al}_{80}$ (8 to 16 kcal mol⁻¹) indicates that dissociation of an N-H bond in chemisorbed NH_3 to form $\text{NH}_2\text{-Al}_{80}\text{-H}$ is thermodynamically favorable.

Seven local minima obtained by fragmentation of an N-H bond in $\text{NH}_2\text{-Al}_{80}\text{-H}$ to form three chemisorbed fragments NH and 2H ($\text{NH-Al}_{80}\text{-}2\text{H}$) were found and are shown in Figure S13. The broad range of binding energies, from 11 to 35 kcal mol⁻¹, shows that fragmentation of a second N-H bond to form $\text{NH-Al}_{80}\text{-}2\text{H}$ can be endothermic or exothermic relative to $\text{NH}_2\text{-Al}_{80}\text{-H}$, depending upon the structural details and specific fragment binding sites on the aluminum cluster. For example, the least stable $\text{NH-Al}_{80}\text{-}2\text{H}$ conformer, with a binding energy of 11 kcal mol⁻¹, is higher in energy than each of the ten $\text{NH}_2\text{-Al}_{80}\text{-H}$ local minima shown in Figure S12. In contrast, the most stable $\text{NH-Al}_{80}\text{-}2\text{H}$ minimum, with a binding energy of 35 kcal mol⁻¹, is lower in energy than each of the ten $\text{NH}_2\text{-Al}_{80}\text{-H}$ local minima. Therefore, relative to $\text{NH}_2\text{-Al}_{80}\text{-H}$, formation of $\text{NH-Al}_{80}\text{-}2\text{H}$ may be exothermic, though not necessarily in all instances.

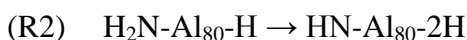
Two structures corresponding to the final fragmentation step, dissociation of NH in $\text{NH-Al}_{80}\text{-}2\text{H}$ to form $\text{N-Al}_{80}\text{-}3\text{H}$, were found and are shown in Figure S14. The binding energies, which range from 13 to 15 kcal mol⁻¹, are similar to that of the most stable conformer of $\text{H}_3\text{N}:\text{Al}_{80}$ (16 kcal mol⁻¹), but are significantly smaller than the most stable isomers of $\text{NH}_2\text{-Al}_{80}\text{-H}$ (30 kcal mol⁻¹) and $\text{NH-Al}_{80}\text{-}2\text{H}$ (35 kcal mol⁻¹). Therefore, from a purely thermodynamic perspective, fragmentation of chemisorbed NH_3 is likely to stop at $\text{NH-Al}_{80}\text{-}2\text{H}$ rather than proceed to complete dissociation to $\text{N-Al}_{80}\text{-}3\text{H}$.

In order to determine the reaction barriers for the fragmentation steps discussed above, saddle point calculations to find the fragmentation transition states were performed, followed by IRC calculations to trace the minimum energy reaction path from the transition state to reactants and products. As shown in Figure S15a, a saddle point for N-H fragmentation of chemisorbed NH_3 leading to $\text{NH}_2\text{-Al}_{80}\text{-H}$ (reaction R1 shown below) was located and is 17 kcal mol⁻¹ higher in energy than separated $\text{NH}_3 + \text{Al}_{80}$. The corresponding reactant, product, and IRC are also displayed in Figure S15a, which shows that the overall reaction is exothermic by 2 kcal mol⁻¹ but traverses a barrier of 31 kcal mol⁻¹. In contrast, the energy required for simple desorption of ammonia from $\text{H}_3\text{N}:\text{Al}_{80}$ is only 14 kcal mol⁻¹. Therefore, N-H dissociation via this saddle point is unlikely to occur, even though the overall process is slightly exothermic. Similar conclusions can be

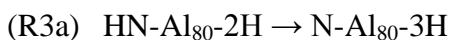
drawn in regard to a structurally distinct but energetically similar saddle point and IRC for N-H fragmentation of chemisorbed NH_3 , for which the reaction barrier and enthalpy are 30 and -6 kcal mol⁻¹, respectively, as illustrated in Figure S15b.



Likewise, two saddle points were located for the second fragmentation step, in which $\text{NH}_2-\text{Al}_{80}-\text{H}$ undergoes N-H bond dissociation to form $\text{NH}-\text{Al}_{80}-2\text{H}$ (reaction R2.) One of these transition states has a reaction barrier of 39 kcal mol⁻¹ and an exothermicity of 7 kcal mol⁻¹, as depicted in Figure S16a. The 39 kcal mol⁻¹ barrier to form $\text{NH}-\text{Al}_{80}-2\text{H}$ is slightly larger than the 33-35 kcal mol⁻¹ barrier of the reverse of reaction R1; i.e., $\text{NH}_2-\text{Al}_{80}-\text{H} \rightarrow \text{H}_3\text{N}:\text{Al}_{80}$, as shown in Figure S15. An additional saddle point for reaction R2, with a barrier of 45 kcal mol⁻¹, is shown in Figure S16b.



A saddle point for the final fragmentation step, dissociation of the remaining N-H bond in $\text{NH}-\text{Al}_{80}-2\text{H}$ to form $\text{N}-\text{Al}_{80}-3\text{H}$ (reaction R3a)



is shown in Figure S17a. Reaction R3a has a barrier of 62 kcal mol⁻¹, which is significantly higher than the 45 kcal mol⁻¹ of the reverse of reaction R2. A saddle point was also located for reaction R3b, which is similar to reaction R3a, but lacks the two “spectator” chemisorbed hydrogen atoms.



This saddle point, shown in Figure S17b, has a corresponding reaction barrier of 62 kcal mol⁻¹.

Formation of H_2 : The relative energies of all stationary points are summarized in Figure S18. As seen in this figure, the transition state energies become larger with increasing number of N-H bond fragmentations. The reaction enthalpy and barrier for recombination of two chemisorbed H atoms to form H_2 were calculated, with the saddle point and IRC shown in Figure S19. This reaction is endothermic by 4 kcal mol⁻¹ and has a barrier of 25 kcal mol⁻¹. Furthermore, in order to assess the mobility of chemisorbed hydrogen atoms on the cluster surface, two reaction paths and barriers for migration of a hydrogen atom between aluminum atom binding sites were computed and are shown in Figure S20. The barriers for H atom migration, which range from 2 to 17 kcal mol⁻¹, are less than the barrier for recombination (25 kcal mol⁻¹), indicating that migration is more facile than formation of H_2 .

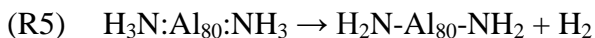
Several unsuccessful attempts were made to locate the saddle point for 1,1 elimination of H₂ from H₃N:Al₈₀ to form NH-Al₈₀ + H₂. However, three distinct local minima corresponding to the products formed via this process (NH-Al₈₀ + H₂) were located, with binding energies ranging from 7 to 24 kcal mol⁻¹ relative to NH₃ + Al₈₀ (see Figure S21.) Therefore, with respect to H₃N:Al₈₀, both endothermic and exothermic pathways for 1,1 elimination of H₂ are possible, although the barriers are unknown.

The lowest barrier pathway to formation of molecular hydrogen was found for reaction R4, the elimination of H₂ from chemisorbed NH₃ and atomic hydrogen:



The calculated barrier and reaction enthalpy are +12 and +1 kcal mol⁻¹, respectively, as illustrated in Figure S22.

Reaction R5, an alternative pathway for the formation of molecular hydrogen in which adjacent chemisorbed NH₃ molecules undergo “biomolecular” H₂ elimination, was also considered.



As illustrated in Figure S23, this reaction is exothermic by 18 kcal mol⁻¹. A saddle point has been located, presumably for reaction R4, and is also shown in Figure S23. Because the saddle point lies 28 kcal mol⁻¹ above the 2NH₃ + Al₈₀ energy asymptote, simple desorption of NH₃ is an energetically more favorable process. Therefore, formation of H₂ via this saddle point is unlikely and thus IRC calculations to confirm the corresponding reactants and products were not performed.

Formation of N₂, N₂H₂, and N₂H₄: Assuming the existence of NH₂ fragments on the nanoparticle surface, recombination of adjacent chemisorbed NH₂ moieties to form hydrazine might be expected to occur. However, as seen in Figure S24c, this process is calculated to be endothermic by 70 to 90 kcal mol⁻¹ and thus unlikely to take place. Similarly, recombination of neighboring chemisorbed NH fragments (see Figure S24b,) formed via reaction R2, to form diimine (HN-Al₈₀-NH → Al₈₀ + HN=NH) is endothermic by 102-105 kcal mol⁻¹ and thus unlikely to occur. Finally, formation of N₂ via recombination of neighboring chemisorbed N atoms, the product of reactions R3a,b, (N-Al₈₀-N → Al₈₀ + N₂) is endothermic by 42-43 kcal mol⁻¹ (Figure S24a.) Therefore, the energetics of these reactions are qualitatively consistent with the predominant formation of H₂ with minimal production of N₂, and the absence of N₂H₂ and NH₂NH₂.

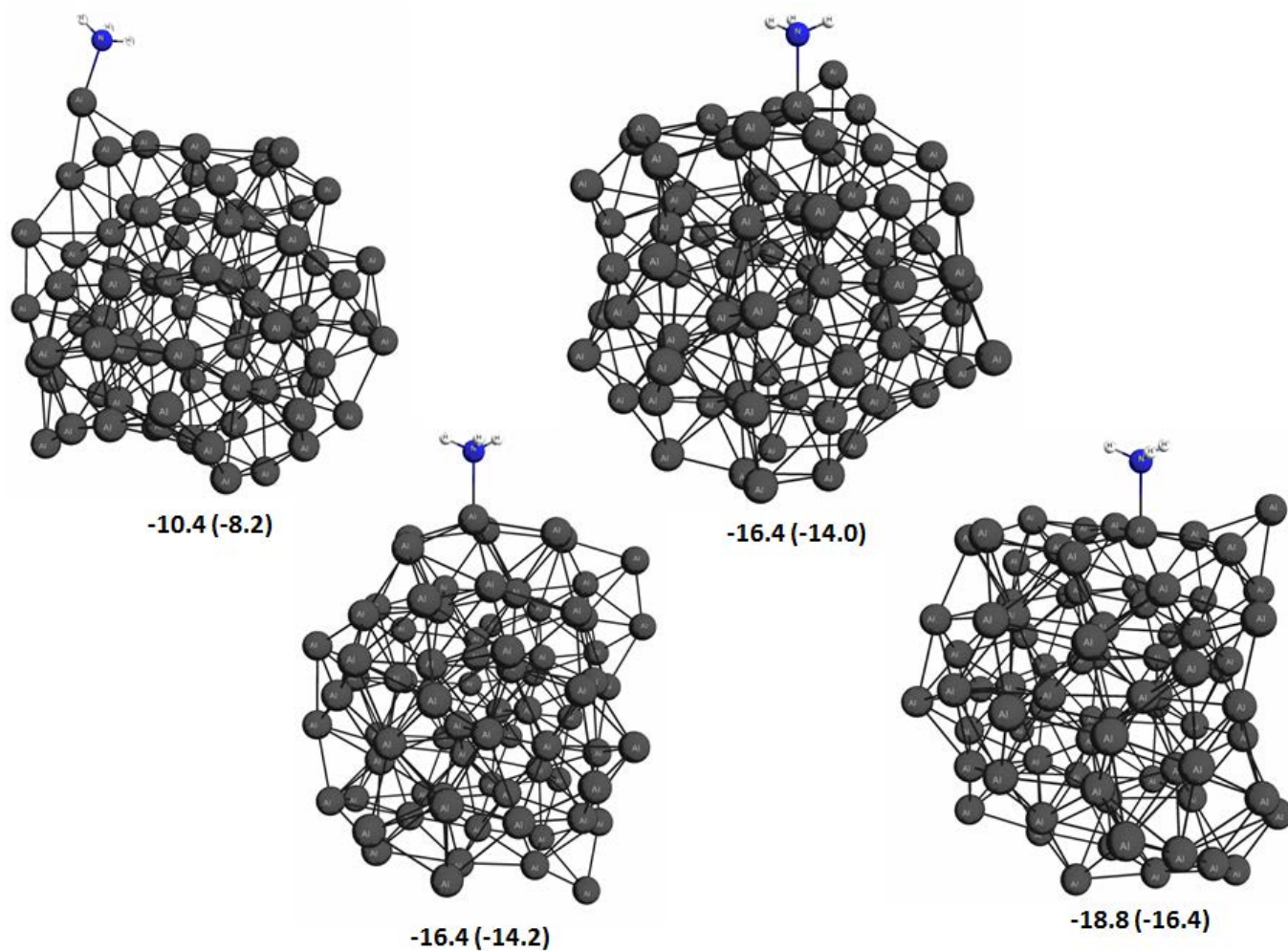


Figure S11. DFT optimized structures of ammonia chemisorbed on Al_{80} . Energies (in kcal mol^{-1}) are relative to separated $\text{NH}_3 + \text{Al}_{80}$. ZPE-corrected energies are given in parentheses.

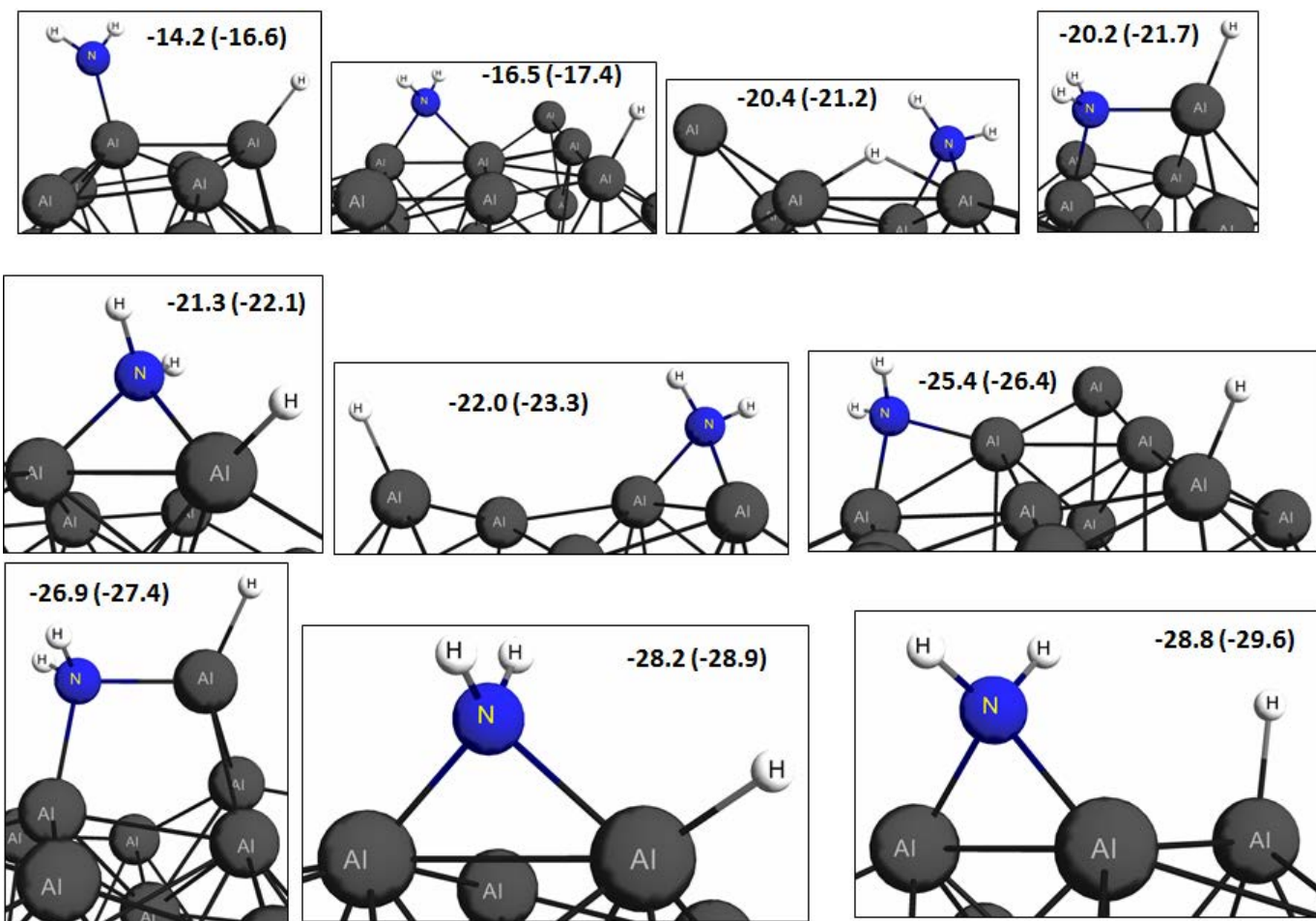


Fig. S12. DFT optimized structures of NH₂ and H fragments chemisorbed on Al₈₀. Energies (in kcal mol⁻¹) are relative to separated NH₃ + Al₈₀. ZPE-corrected energies are given in parentheses. A portion of the Al₈₀ substrate has been cropped to show the chemisorbed fragments in greater detail.

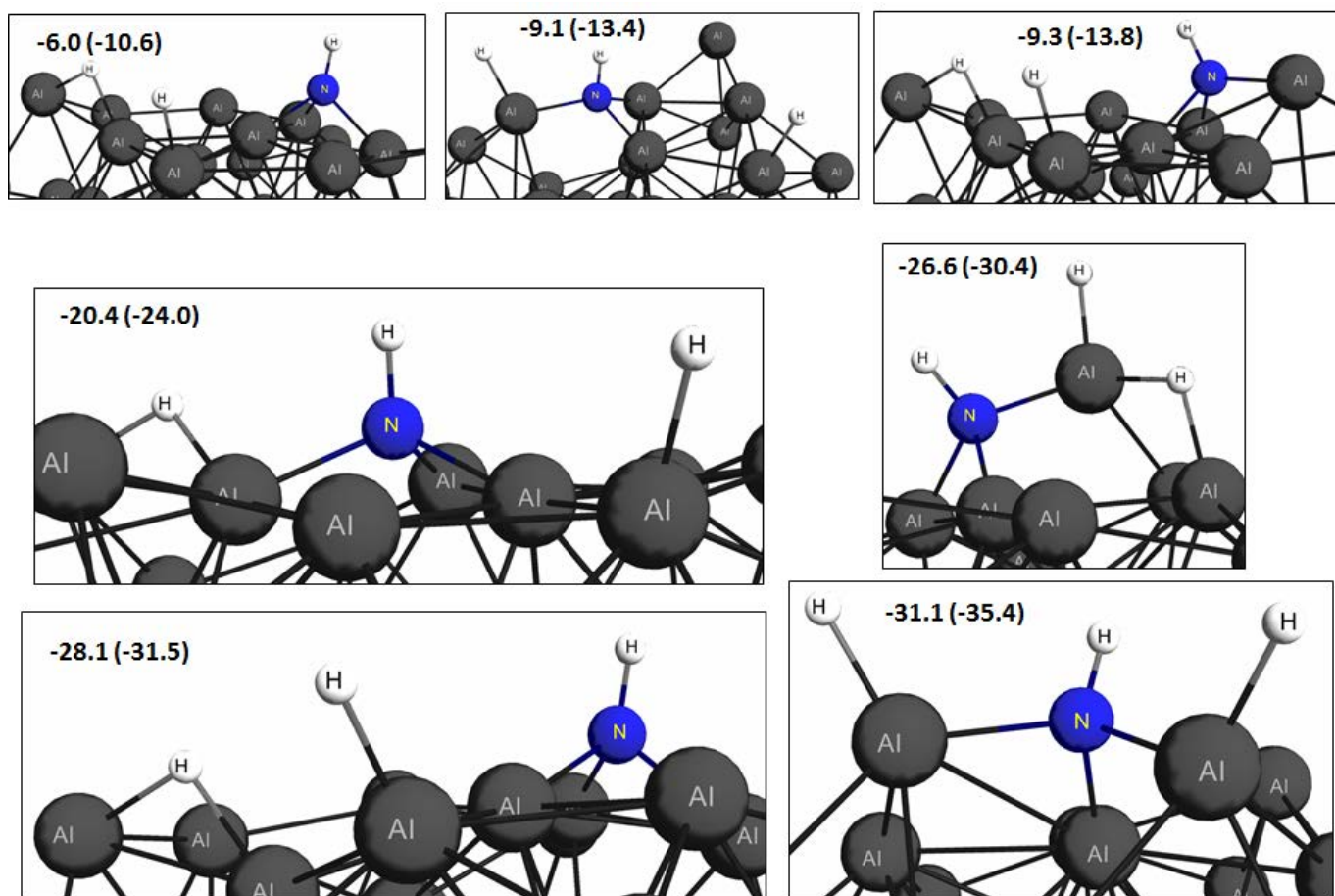


Fig. S13. DFT optimized structures of $\text{NH} + 2\text{H}$ fragments chemisorbed on Al_{80} . Energies (in kcal mol^{-1}) are relative to separated $\text{NH}_3 + \text{Al}_{80}$. ZPE-corrected energies are given in parentheses. A portion of the Al_{80} substrate has been cropped to show the chemisorbed fragments in greater detail.

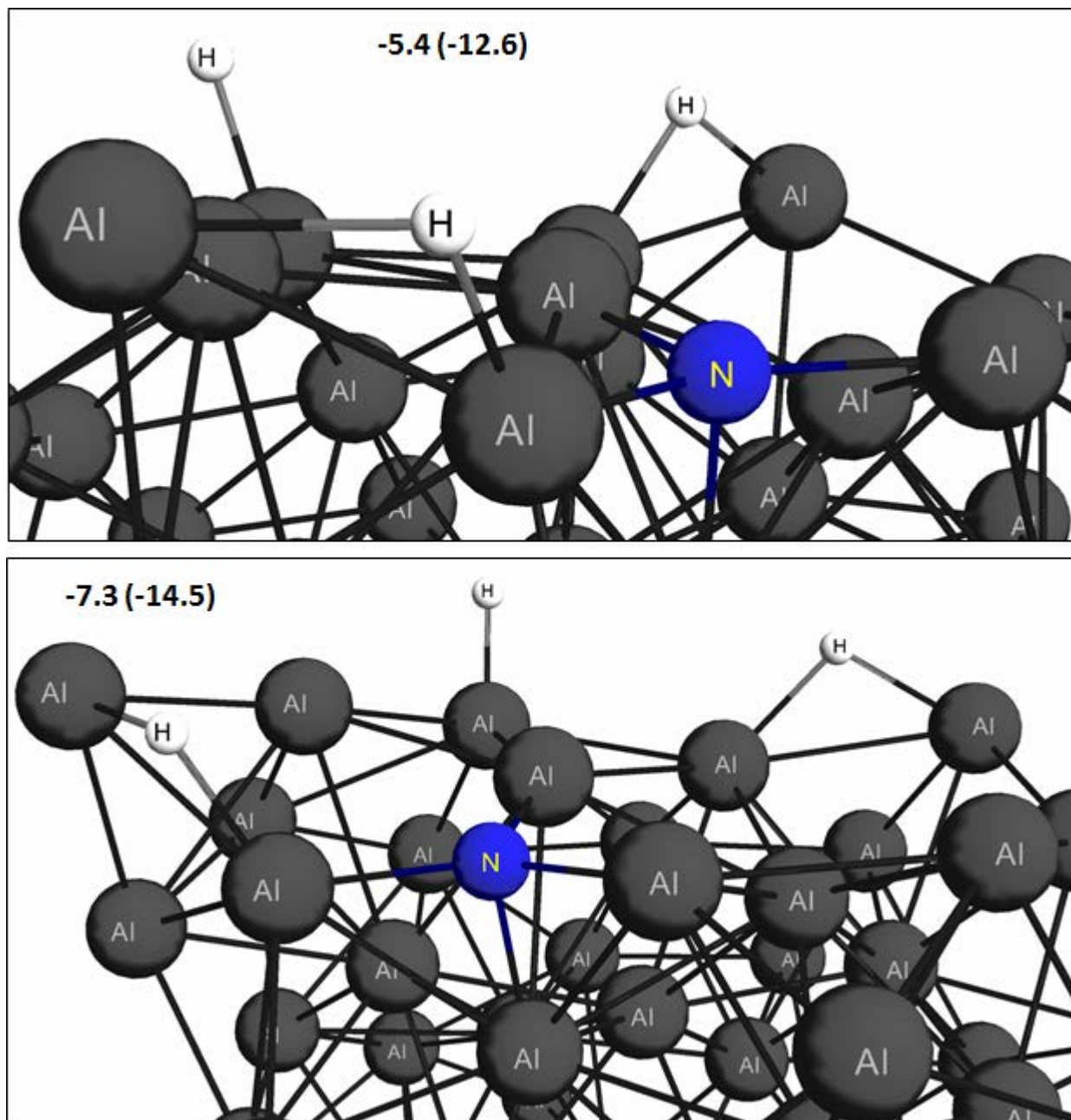


Fig. S14. DFT optimized structures of N + 3H fragments chemisorbed on Al₈₀. Energies (in kcal mol⁻¹) are relative to separated NH₃ + Al₈₀. ZPE-corrected energies are given in parentheses. A portion of the Al₈₀ substrate has been cropped to show the chemisorbed fragments in greater detail.

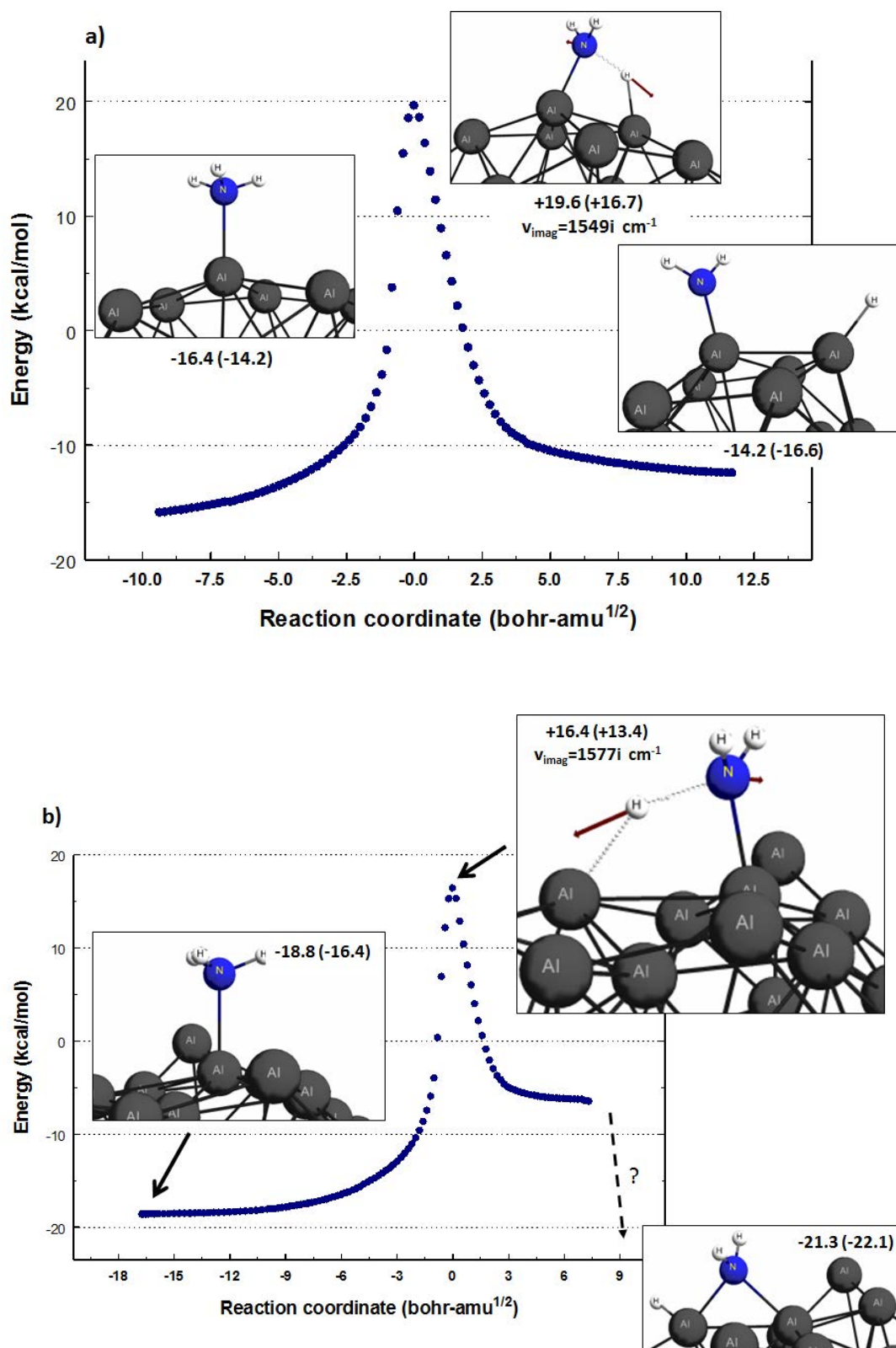


Figure S15. Two transition states and IRCs (blue circles) of chemisorbed NH_3 undergoing N-H fragmentation to form chemisorbed $\text{NH}_2 + \text{H}$, excluding zero point energy (ZPE) corrections. The energies, in kcal mol⁻¹, of the stationary points (reactant, saddle point, and product) are relative to separated $\text{NH}_3 + \text{Al}_{80}$. ZPE-corrected energies are given in parentheses. In panel (b), IRC calculations from the saddle point toward the product were unable to proceed past the rightmost point on the IRC plot. However, a geometry optimization starting at this point led to the fully optimized structure shown in the lower right corner of the figure. A portion of the Al_{80} substrate has been cropped to show the chemisorbed fragments in greater detail.

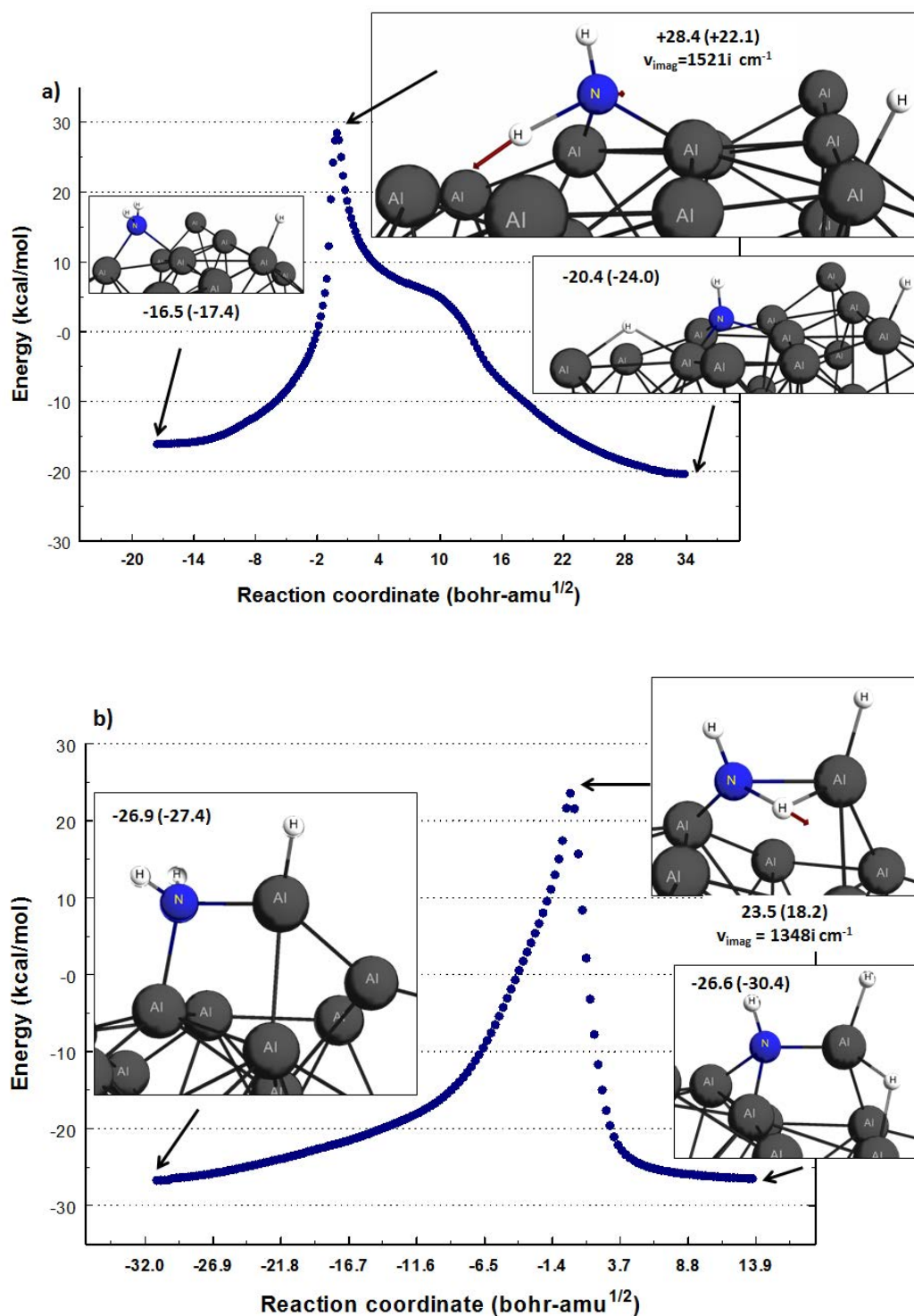


Figure S16. Two transition states and IRCs (blue circles) of chemisorbed NH_2 undergoing N-H fragmentation to form chemisorbed $\text{NH} + 2\text{H}$. The energies (in kcal mol^{-1}) of the stationary points (reactant, saddle point, and product) are relative to separated $\text{NH}_3 + \text{Al}_{80}$. ZPE-corrected energies are given in parentheses. A portion of the Al_{80} substrate has been cropped to show the chemisorbed fragments in greater detail.

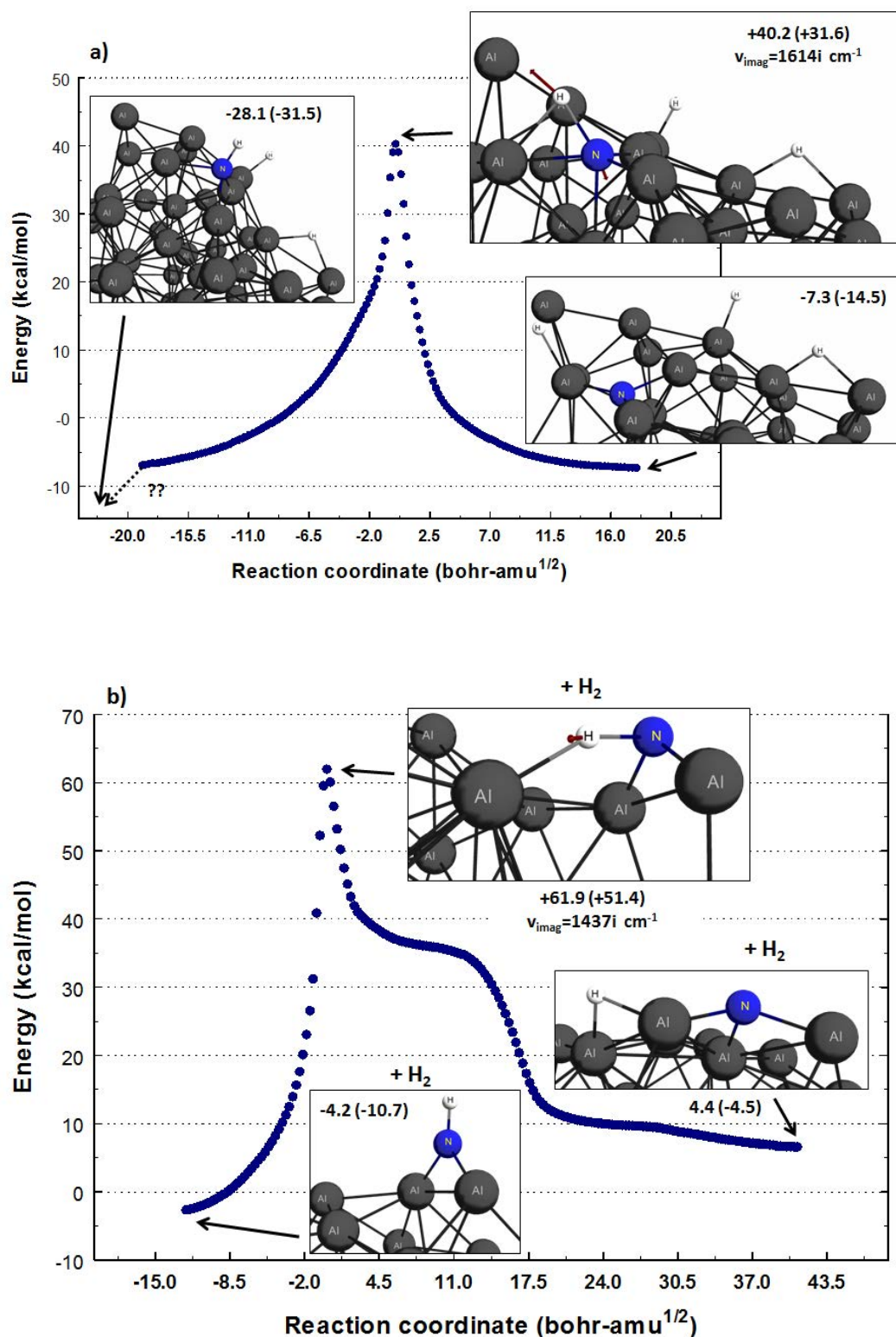


Figure S17. Two transition states and IRCs (blue circles) of chemisorbed NH undergoing N-H fragmentation to form chemisorbed N + H, excluding zero point energy (ZPE) corrections. The energies (in kcal mol⁻¹) of the stationary points (reactant, saddle point, and product) are relative to separated NH₃ + Al₈₀. ZPE-corrected energies are given in parentheses. In panel a), IRC calculations from the saddle point toward the reactant were unable to proceed past the leftmost point on the IRC plot. However, a geometry optimization starting at this point led to the fully optimized structure shown in the upper left corner of the figure. A portion of the Al₈₀ substrate has been cropped to show the chemisorbed fragments in greater detail.

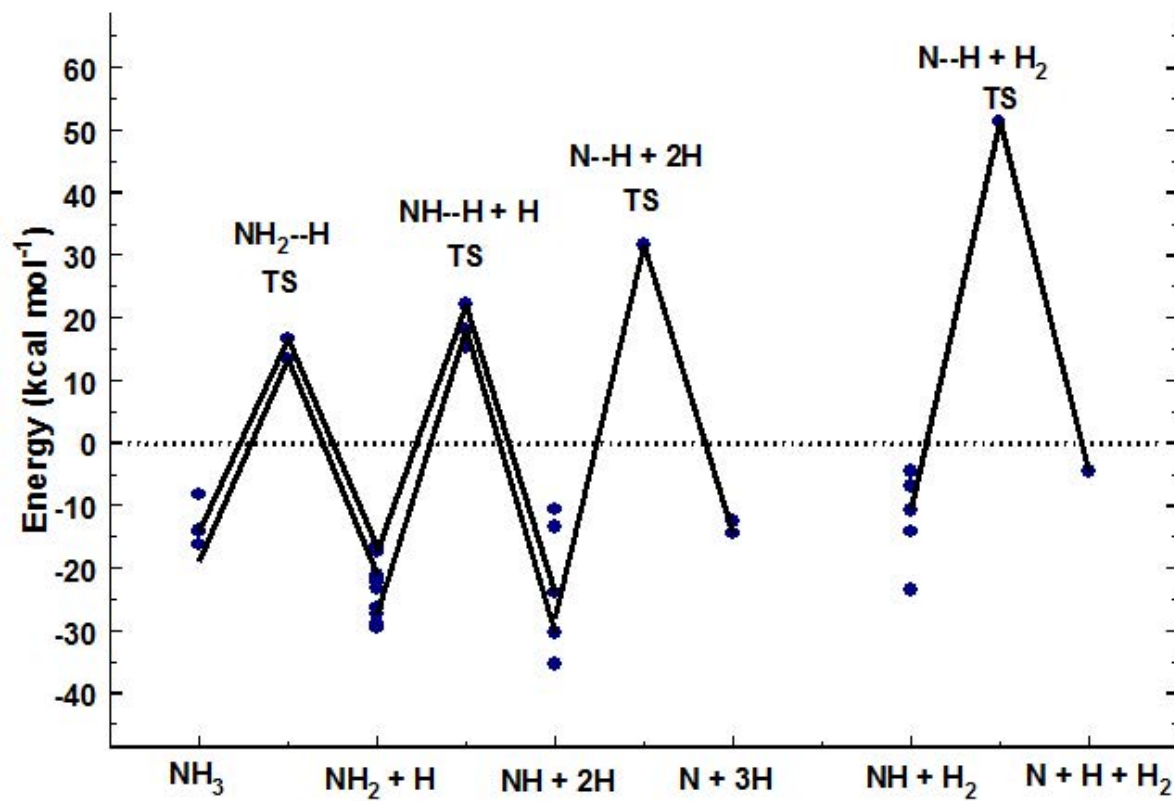


Figure S18. Energies of chemisorbed NH_3 , $\text{NH}_2 + \text{H}$, $\text{NH} + 2\text{H}$, $\text{N} + 3\text{H}$, $\text{NH} + \text{H}_2$, $\text{N} + \text{H} + \text{H}_2$, and connecting saddle points, relative to separated $\text{NH}_3 + \text{Al}_{80}$. Solid lines denote completed IRC calculations.

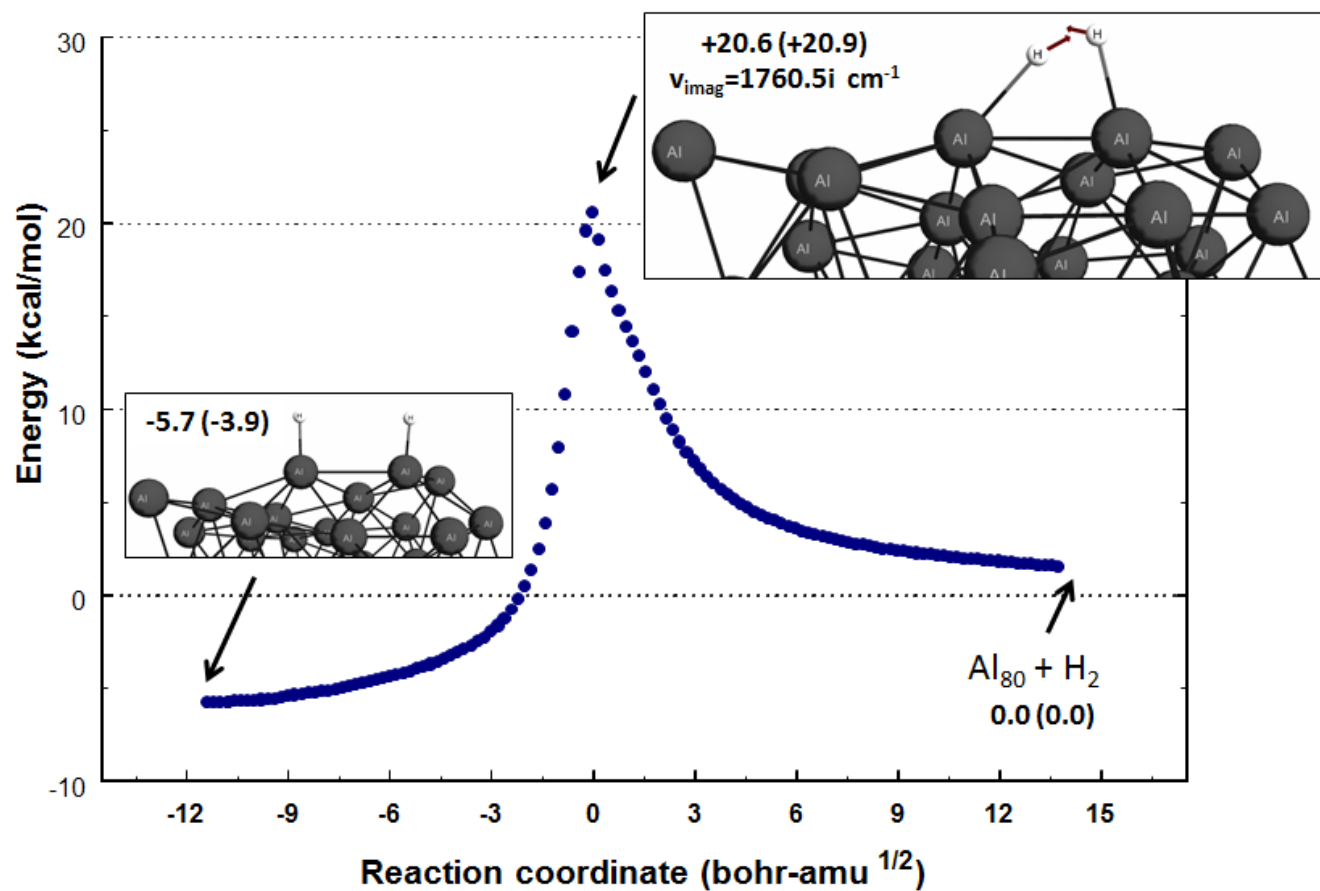


Figure S19. Transition state and IRC (blue circles) for recombination of two chemisorbed H atoms to form H_2 , excluding zero point energy (ZPE) corrections. Energies (in kcal mol⁻¹) of the stationary points (reactant, saddle point, and product) are relative to separated $\text{H}_2 + \text{Al}_{80}$. ZPE-corrected energies are given in parentheses. A portion of the Al_{80} substrate has been cropped to show the chemisorbed fragments in greater detail.

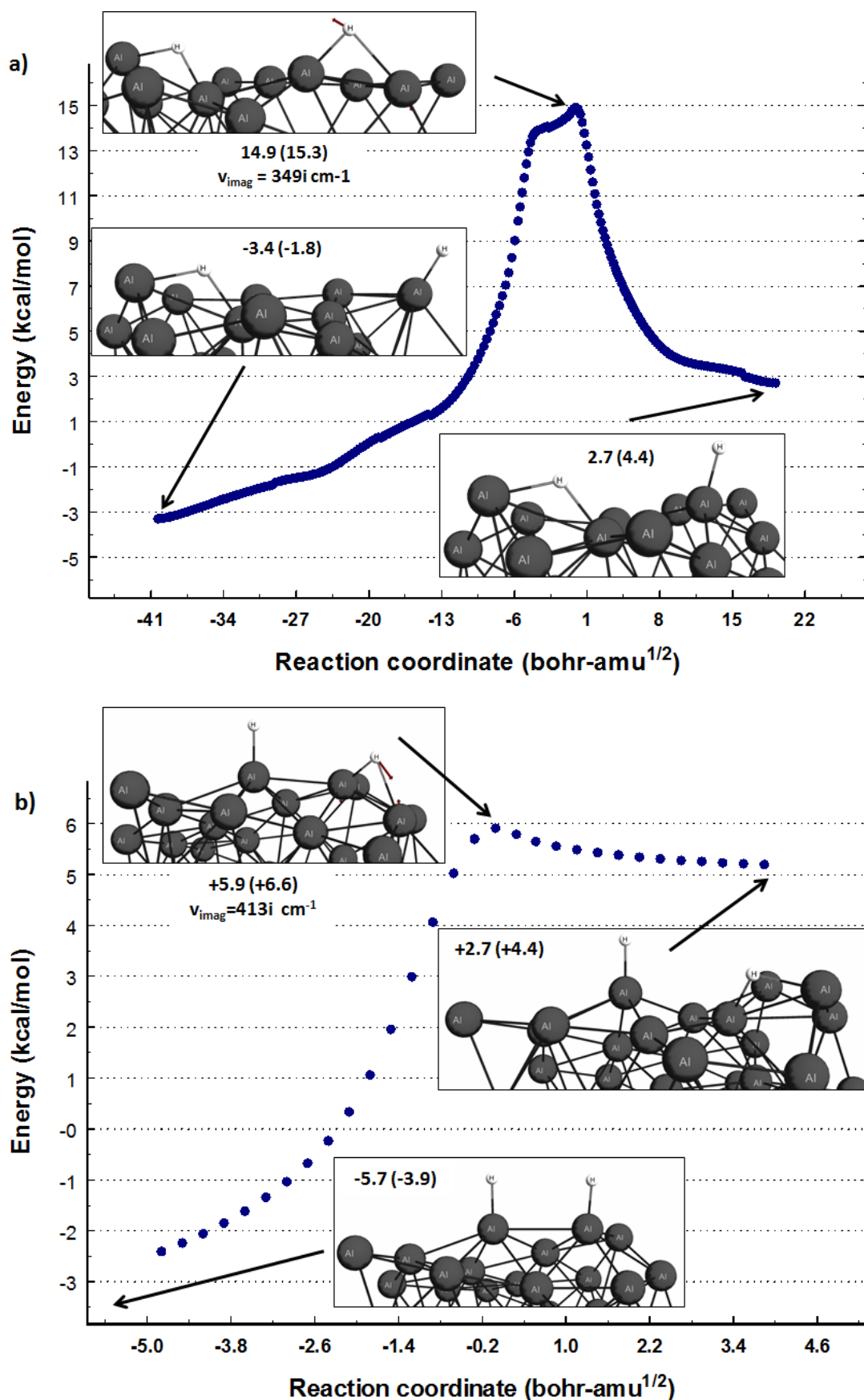


Figure S20. Transition states and IRCs (blue circles) for migration of a chemisorbed H atom along the surface of Al_{80} , excluding zero point energy (ZPE) corrections. The energies (in kcal mol^{-1}) of the stationary points (reactant, saddle point, and product) are relative to separated $\text{H}_2 + \text{Al}_{80}$. ZPE-corrected energies are given in parentheses. A portion of the Al_{80} substrate has been cropped to show the chemisorbed fragments in greater detail. In panel (a) (panel (b)), the forward and reverse barriers are 17 and 11 (11 and 2) kcal mol^{-1} , respectively.

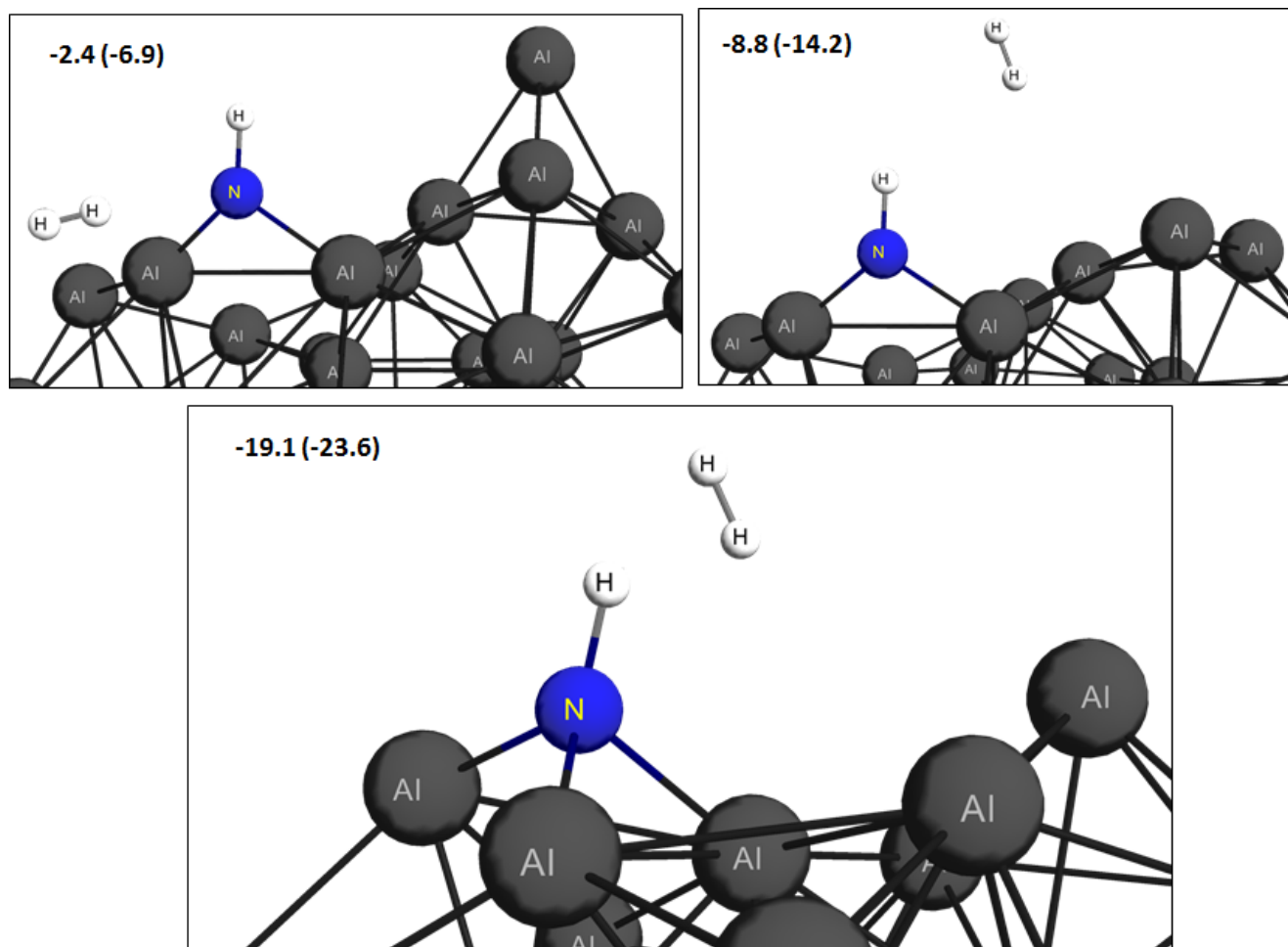


Figure S21. DFT optimized structures of H_2 plus chemisorbed NH_3 . Energies (in kcal mol^{-1}) are relative to separated $\text{NH}_3 + \text{Al}_{80}$. ZPE-corrected energies are given in parentheses. A portion of the Al_{80} substrate has been cropped to show the chemisorbed fragments in greater detail.

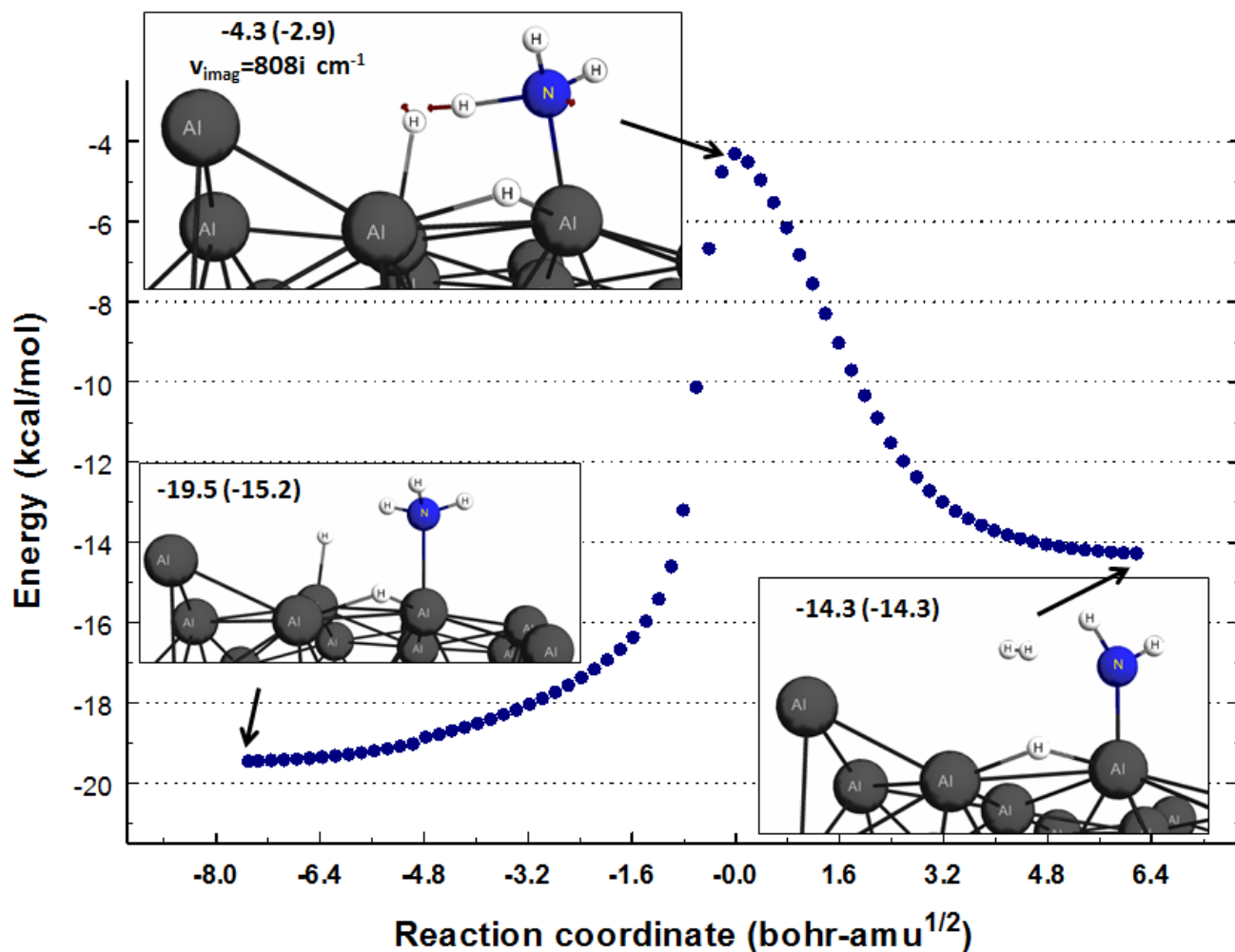


Figure S22 . Transition state and IRC (blue circles) for elimination of H_2 from chemisorbed NH_3 and H , excluding zero point energy (ZPE) corrections. The energies (in kcal mol⁻¹) of the stationary points (reactant, saddle point, and product) are relative to separated $\text{H}_2 + \text{Al}_{80}$. ZPE-corrected energies are given in parentheses. A portion of the Al_{80} substrate has been cropped to show the chemisorbed fragments in greater detail.

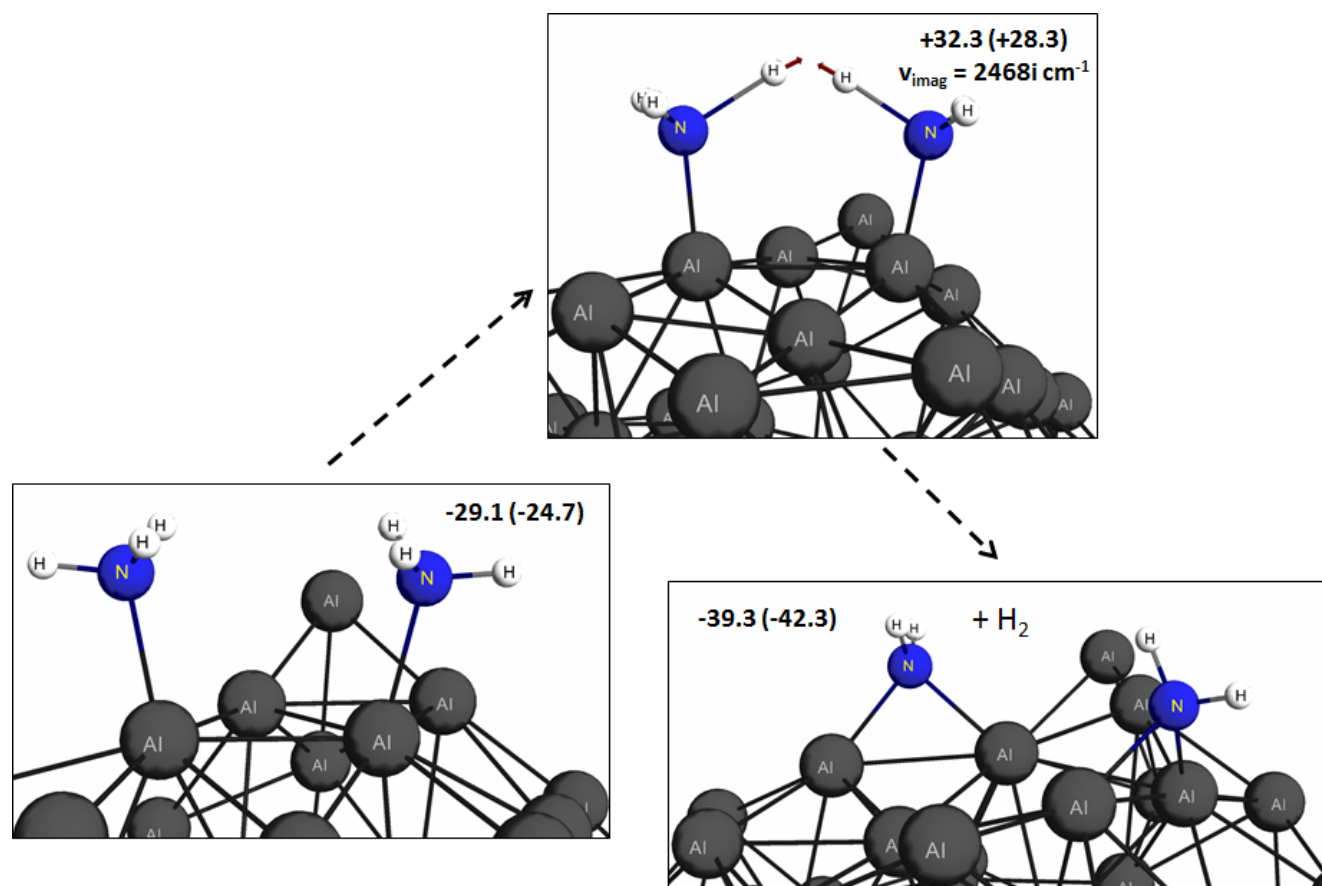


Figure S23. Transition state and presumed reactants and products for “bimolecular” elimination of H_2 from neighboring chemisorbed NH_3 molecules. The energies (in kcal mol^{-1}) of the stationary points (reactant, saddle point, and product) are relative to separated $2\text{NH}_3 + \text{Al}_{80}$. ZPE-corrected energies are given in parentheses. A portion of the Al_{80} substrate has been cropped to show the chemisorbed fragments in greater detail.

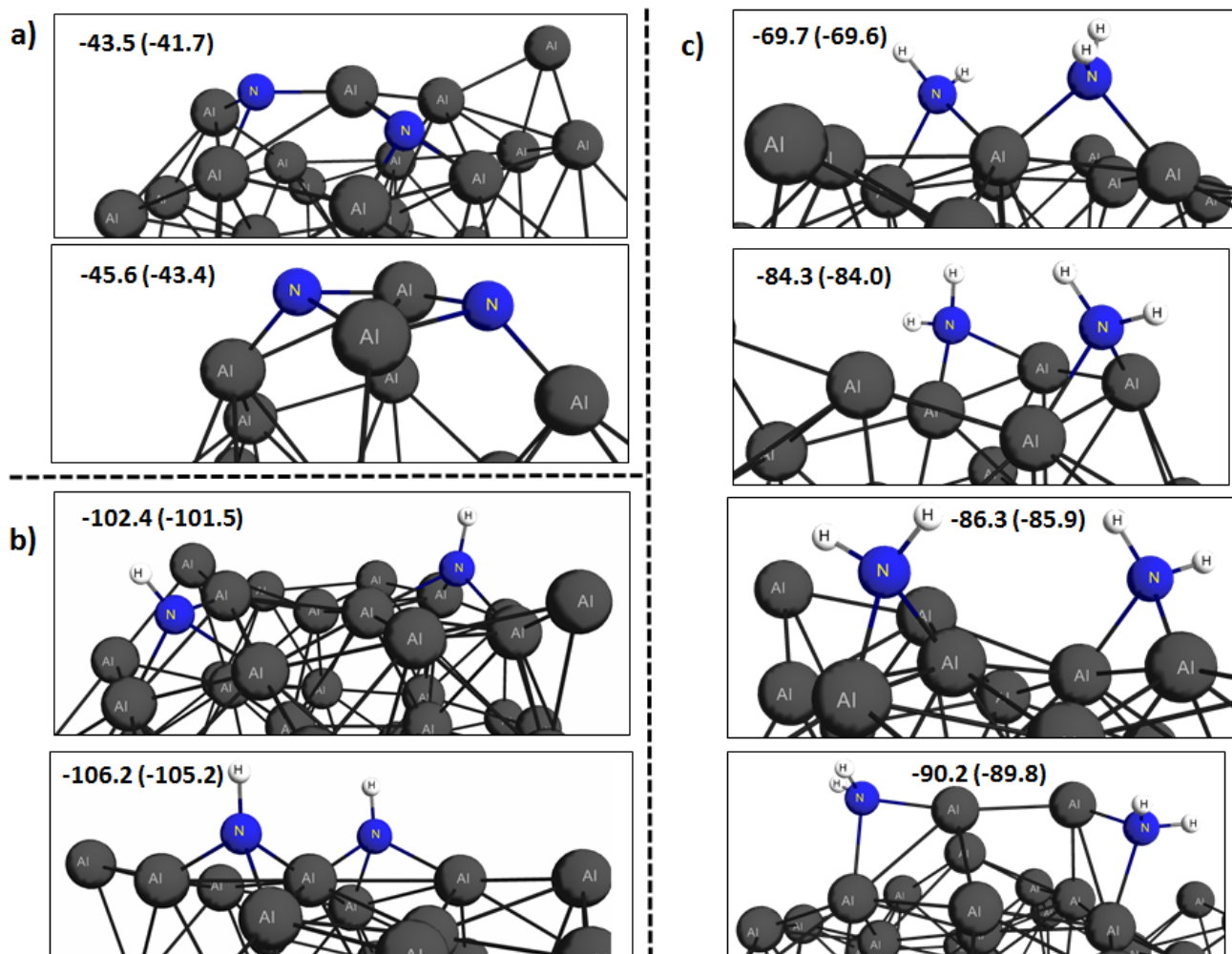


Figure S24. DFT optimized structures of chemisorbed N atoms (N-Al₈₀-N, panel a), NH groups (HN-Al₈₀-NH, panel b), and NH₂ groups (H₂N-Al₈₀-NH₂, panel c.) Energies (in kcal mol⁻¹) are relative to separated Al₈₀ + N₂, N₂H₂, and N₂H₄, respectively. ZPE-corrected energies are given in parentheses. A portion of the Al₈₀ substrate has been cropped to show the chemisorbed fragments in greater detail.

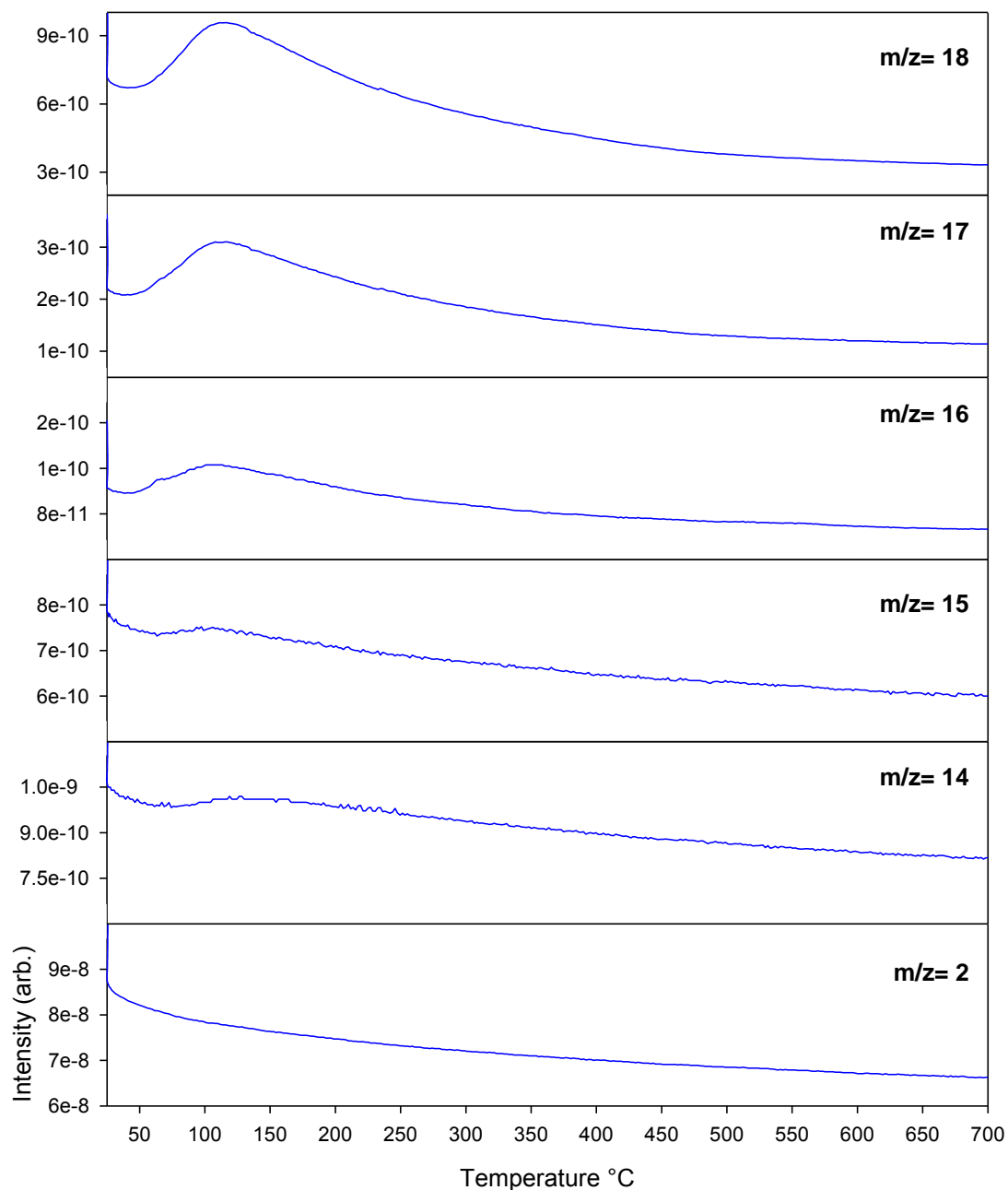


Fig. S25 Tandem MS-TGA, mass-to-charge channels for methylamine-milled aluminum nanoparticles, which were transferred under argon to a TGA instrument housed in a N₂ glove box. Note: Because of differences in background signal the intensity scale varies and is labeled for each spectrum

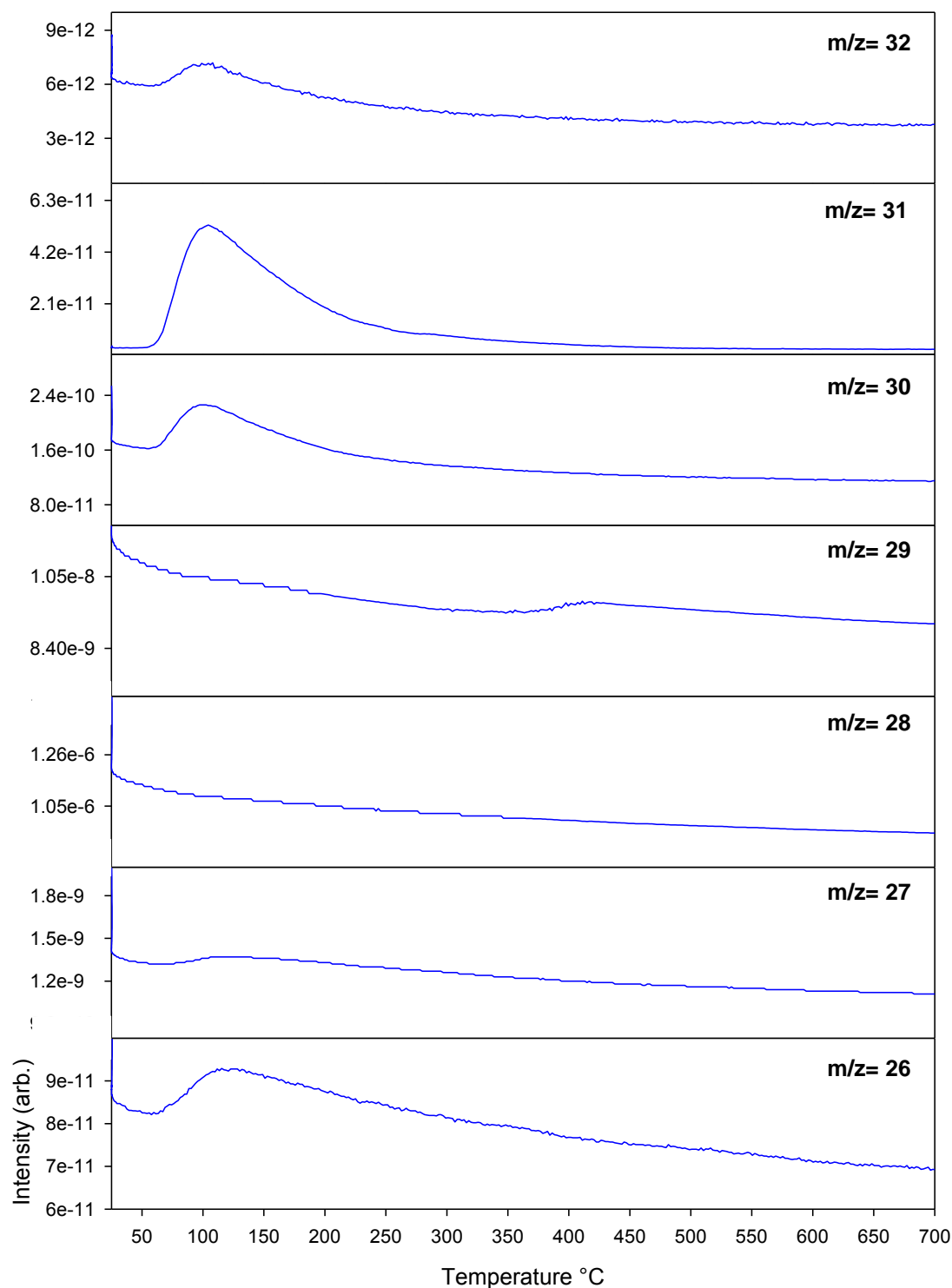


Fig. S 26. Tandem MS-TGA, mass-to-charge channels for methylamine-milled aluminum nanoparticles, which were transferred under argon to a TGA instrument housed in a N_2 glove box. Note: Because of differences in background signal the intensity scale varies and is labeled for each spectrum

The carbon 1s spectra for the sputtered and non-sputtered sample is shown in Figure C32. It is not surprising, that the largest peak for the air exposed sample is at 284.8 eV, which is typically assigned to adventitious carbon.¹ The low binding energy peak for the exposed sample is representative of a peak that could potentially be assigned to a metal carbide.² However, the only explanation for why the peak increases upon exposure to air, is a reaction of uncapped surface atoms reacting with adventitious carbon species. Evidence of hydrocarbons dissociating on metal defect sites has been reported, and therefore this must be considered.³ The most probable source for the large C 1s component of the inert transfer is physisorbed methylamine, and evidence for this physisorbed species detected TGA-MS.

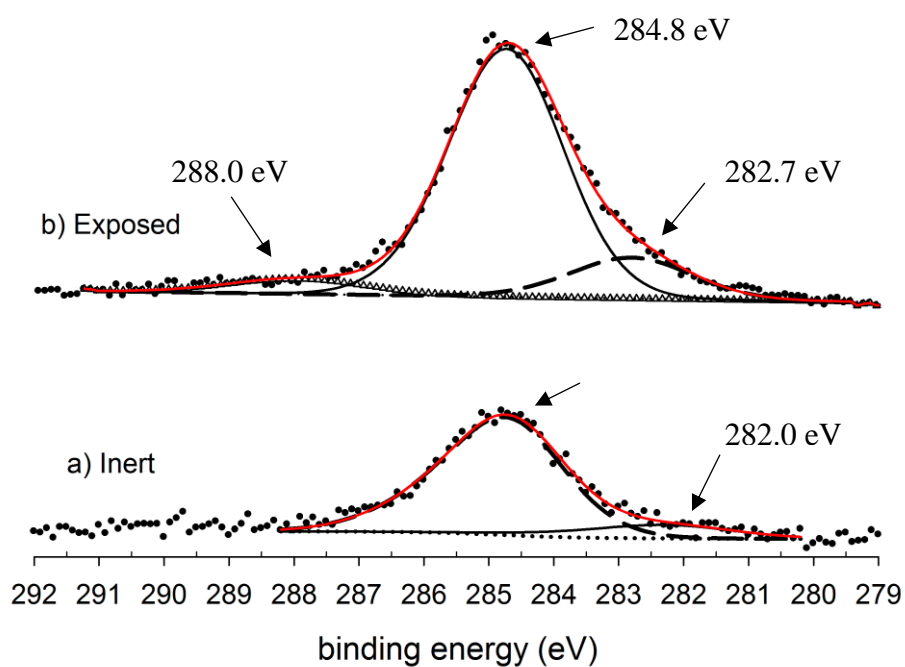


Fig. S27. High resolution X-Ray photoelectron C 1s region scan of particles milled in methylamine for 4 hours, pressed into a pellet, and transferred to the XPS instrument under argon. a) As-transferred b) exposed to air

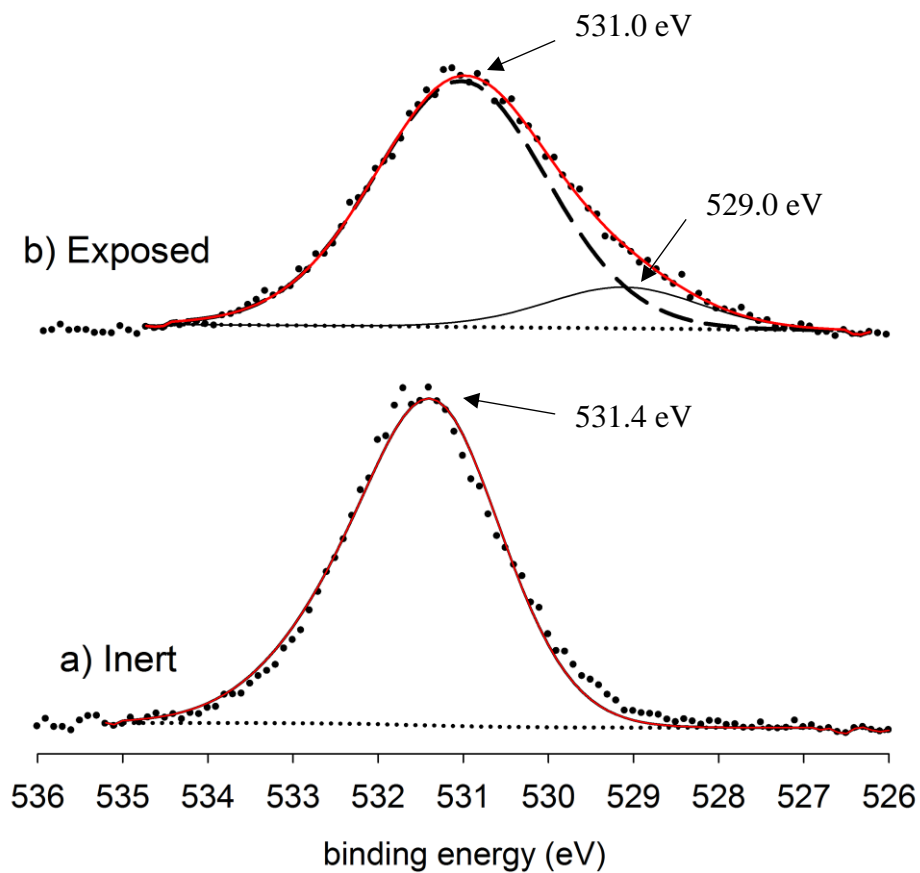


Fig. S28. High resolution X-Ray photoelectron O 1s region scan of particles milled in methylamine for 4 hours, pressed into a pellet, and transferred to the XPS instrument under argon. a) As-transferred b) exposed to air

CH₃NH₂ + Al₈₀: Similar to the case of ammonia, monomethylamine forms a weak dative bond to the surface of the Al₈₀ cluster with a binding energy of 18 kcal/mol, as illustrated in Figure S29. Starting from this structure, three bond dissociation pathways (N-H, C-H, and C-N bond scissions) of chemisorbed monomethylamine, denoted henceforth as MMA:Al₈₀, are considered. The final products of these three reactions are shown in Figure 13. Dissociation of an N-H bond to form chemisorbed CH₃NH and H (CH₃NH-Al₈₀-H; see Figure 13a) is exothermic by 8 kcal mol⁻¹ relative to MMA:Al₈₀. C-H bond dissociation leading to formation of (CH₂NH₂)-Al₈₀-H (Figure 13b) is endothermic by 2 kcal mol⁻¹ with respect to MMA:Al₈₀. In contrast, cleavage of the C-N bond to form CH₃-Al₈₀-NH₂ (Figure 13c) is exothermic by 26 kcal mol⁻¹ and therefore the most thermodynamically favorable of the three bond dissociation reactions. Note that additional isomers of CH₃NH-Al₈₀-H, (CH₂NH₂)-Al₈₀-H, and CH₃-Al₈₀-NH₂ are shown in Figure S30.

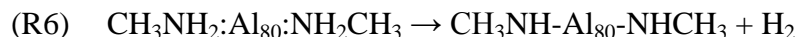
A saddle point corresponding to N-H fragmentation in MMA:Al₈₀ leading to formation of CH₃NH-Al₈₀-H was located and is shown in Figure S31, which also indicates that the overall reaction is exothermic by 8 kcal mol⁻¹ but has a barrier of 26 kcal mol⁻¹. Furthermore, the energy of the saddle point is 8 kcal mol⁻¹ higher than separated MMA + Al₈₀, indicating that simple desorption of CH₃NH₂ from MMA:Al₈₀ is a more favorable process than N-H fragmentation. Similarly, a C-H fragmentation saddle point has also been located and is illustrated in Figure S32, which shows that this process is endothermic by 2 kcal mol⁻¹ and encounters a large barrier of 50 kcal mol⁻¹. Since the saddle point is over 30 kcal mol⁻¹ higher in energy than separated MMA + Al₈₀, IRC calculations to confirm the identities of the reactants and products were not performed. Calculations to locate the saddle point for C-N bond fragmentation in MMA:Al₈₀ to produce CH₃-Al₈₀-NH₂ were unsuccessful. However, a saddle point leading to formation of the latter from chemisorbed H and (CH₂NH₂) was found and is shown in Figure S33. This pathway is exothermic by 35 kcal mol⁻¹ and has a barrier of 36 kcal mol⁻¹.

Formation of H₂: Since C-N bond dissociation of MMA to form chemisorbed CH₃ and NH₂ is the most thermodynamically favorable fragmentation pathway, bimolecular elimination of H₂ from the three possible pairings of CH₃ and NH₂ was considered (not shown.) As stated previously, the H₂ elimination reaction H₂N-Al₈₀-NH₂ → HN-Al₈₀-NH + H₂ is endothermic by 10 kcal mol⁻¹. Similarly, H₃C-Al₈₀-CH₃ → H₂C-Al₈₀-CH₂ + H₂ is endothermic by 28 kcal mol⁻¹ and H₃C-Al₈₀-NH₂ → H₂C-Al₈₀-NH + H₂ is endothermic by 13 kcal mol⁻¹. Saddle point searches for these three H₂ elimination reactions were unsuccessful.

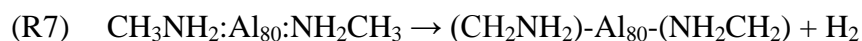
The 1,1 elimination of H₂ from the amino group in MMA:Al₈₀, resulting in formation of CH₃N-Al₈₀ + H₂ (see Figure S34a,) is endothermic by 9 kcal mol⁻¹. Since the final products are more stable than MMA + Al₈₀, attempts were made to locate the saddle point for this reaction, but were unsuccessful. The 1,2 elimination of H₂ from MMA:Al₈₀ to form chemisorbed methanimine (CH₂=NH:Al₈₀) + H₂ (Figure S34b) is endothermic by 28 kcal mol⁻¹. Since the products are less stable than separated MMA + Al₈₀, this pathway is excluded from further consideration as a possible source of molecular hydrogen.

Next, formation of H₂ via single-step elimination reactions involving neighboring chemisorbed methylamine molecules (MMA:Al₈₀:MMA) is considered. One such pathway is shown by reaction R6 and is depicted in Figure S35 (panels a and b) in which two amino hydrogen atoms,

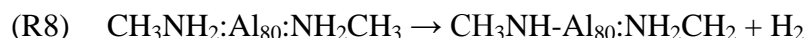
one from each chemisorbed methylamine, are eliminated and subsequently combine to form H₂, as shown in reaction R6.



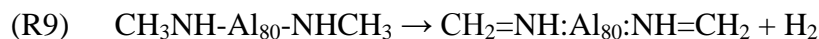
This reaction is exothermic by 17 kcal mol⁻¹ and thus is an energetically favorable pathway to formation of H₂, to the extent that the reaction barrier is less than the energy required to desorb a molecule of methylamine (~18 kcal mol⁻¹.) The analogous reaction (R7) involving elimination of hydrogen atoms from the methyl groups in chemisorbed MMA (Figure S35d) is endothermic by 16 kcal mol⁻¹.



The cross-elimination reaction R8, involving a hydrogen atom from an amino group and the other from a methyl group (Figure S35c,) is exothermic by 3 kcal mol⁻¹. Thus, the latter two bimolecular elimination pathways R7 and R8 are deemed to be less likely sources of H₂ than the first (R6.)



In principle, many secondary H₂ elimination reactions originating from the chemisorbed products of reactions R6-R8 are likewise possible. However, only one such reaction (R9, shown below) is considered in the present work, since this pathway can also account for the formation of CH₂=NH. The reaction enthalpy is 65 kcal mol⁻¹ (**estimated**), and thus unlikely to occur.



In summary, formation of H₂ via elimination reactions of hydrogen from chemisorbed CH₃ and NH₂ is endothermic, as is unimolecular elimination of H₂ from MMA:Al₈₀. However, two exothermic pathways for the formation of molecular hydrogen involving bimolecular elimination of H₂ from neighboring chemisorbed MMA molecules have been identified, although the corresponding barriers are unknown.

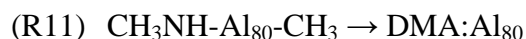
Formation of CH₂=NH: One possible pathway leading to formation of chemisorbed methanimine (Figure S34b) is by unimolecular 1,2 elimination of H₂ from MMA:Al₈₀. However, as discussed previously, this reaction is energetically unfavorable and thus unlikely to occur to a significant extent. An alternative, two-step mechanism (reaction R10a) involving stepwise dissociation of a C-H bond in MMA:Al₈₀, with subsequent chemisorption of both fragments (CH₂NH₂ and H), followed by N-H bond dissociation to form CH₂=NH:Al₈₀-2H, is found to be endothermic by 17 kcal mol⁻¹. Of course, the order of C-H and N-H bond scissions can be reversed (reaction R10b.) The structures and relative energies of the reactants, intermediates, and products of reaction R10 are illustrated in Figure S36.



The binding energies of the intermediates in reactions R10a and R10b are 16 and 18 kcal mol⁻¹, respectively, which are comparable to that of the reactant (MMA:Al₈₀), 18 kcal mol⁻¹. The final product is marginally more stable than separated MMA + Al₈₀, by 1 kcal mol⁻¹.

The “bimolecular” pathway, reaction R9 above is another potential route to the formation of methanimine, but has a large endothermicity of 65 kcal mol⁻¹ (excluding ZPE corrections.)

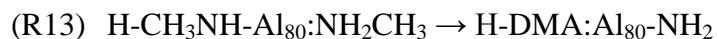
Formation of CH₃NHCH₃: Several elementary reactions leading to the formation of dimethylamine (DMA) are possible. The first to be considered here is reaction R11, the recombination of chemisorbed CH₃ and CH₃NH (CH₃-Al₈₀-NHCH₃) leading directly to DMA:Al₈₀, as shown in Figure S37. This reaction is endothermic by 9 kcal mol⁻¹.



Similarly, DMA may also be formed in the transfer of a methyl group from one chemisorbed NHCH₃ ligand to another, resulting in formation of chemisorbed DMA plus an NH ligand, as shown in reaction R12 and Figure S38. This reaction is endothermic by 16 kcal mol⁻¹.



The final DMA-generating reaction to be considered in this study is the migration of a methyl group between neighboring chemisorbed monomethylamine and CH₃NH, leading to formation of chemisorbed DMA and NH₂ ligands, as shown in Figure S39 and reaction R13. This reaction is exothermic by 17 kcal mol⁻¹ and therefore is the most favorable pathway to formation of DMA.



(A “spectator” chemisorbed hydrogen atom is included in reaction R13 to maintain closed shell singlet electronic states for computational consistency and convenience.)

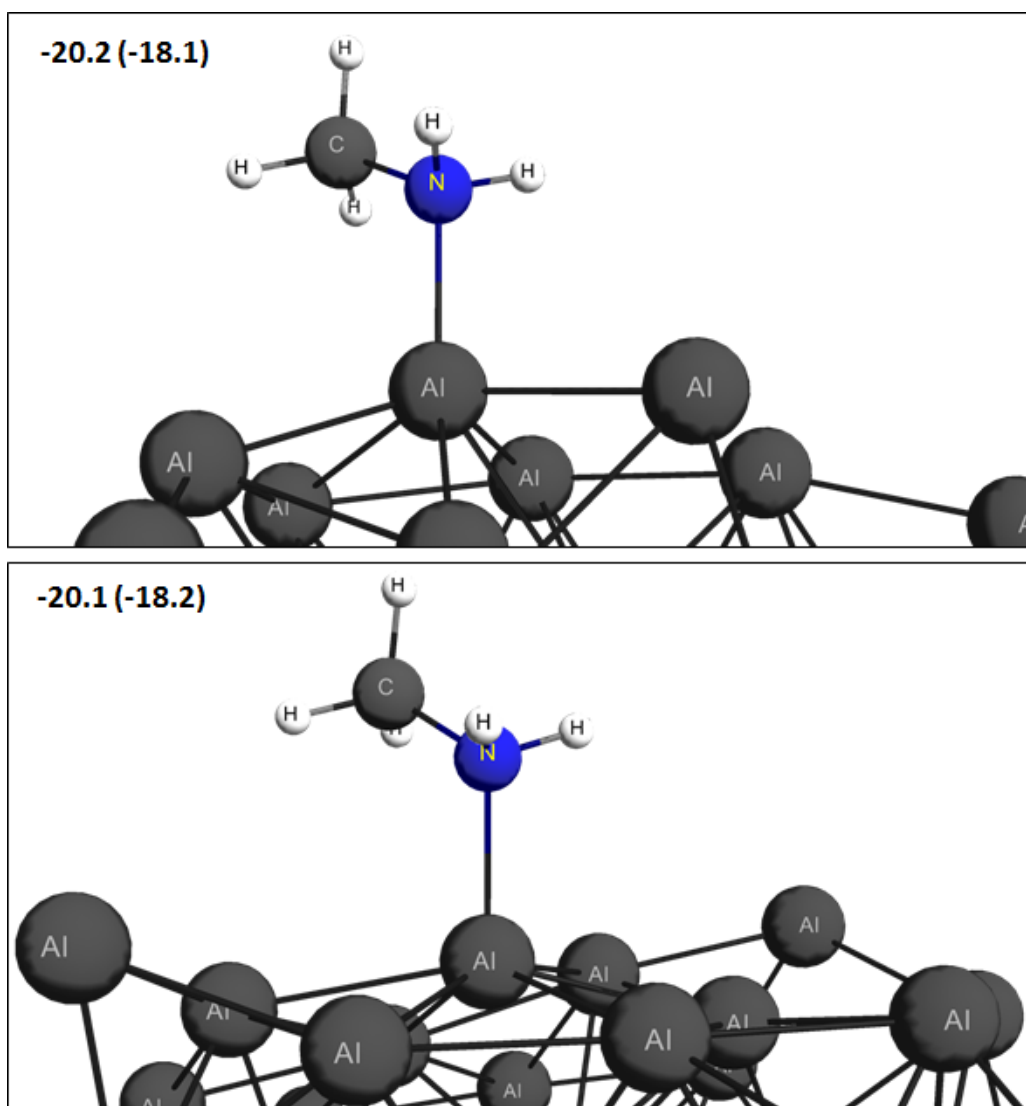


Fig. S29. DFT optimized structures of monomethylamine chemisorbed on Al_{80} . The binding energies (in kcal mol^{-1}) are relative to $\text{CH}_3\text{NH}_2 + \text{Al}_{80}$. ZPE-corrected energies are given in parentheses. A portion of the Al_{80} substrate has been cropped to show the chemisorbed fragments in greater detail.

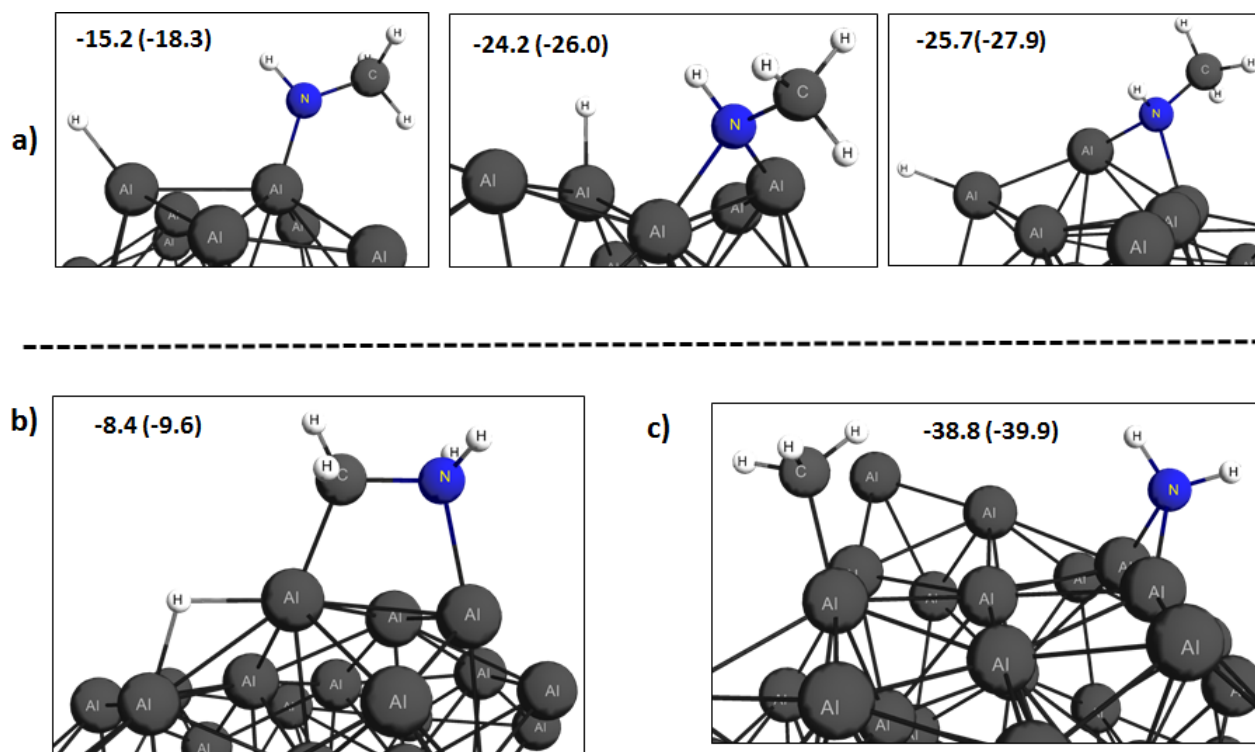


Fig. S30. Additional isomers of $\text{CH}_3\text{NH}-\text{Al}_{80}-\text{H}$ (panel a); $(\text{CH}_2\text{NH}_2)-\text{Al}_{80}-\text{H}$ (panel b); and $\text{CH}_3-\text{Al}_{80}-\text{NH}_2$ (panel c.) Energies (in kcal mol^{-1}) are relative to separated $\text{CH}_3\text{NH}_2 + \text{Al}_{80}$. ZPE-corrected energies are given in parentheses. A portion of the Al_{80} substrate has been cropped to show the chemisorbed fragments in greater detail.

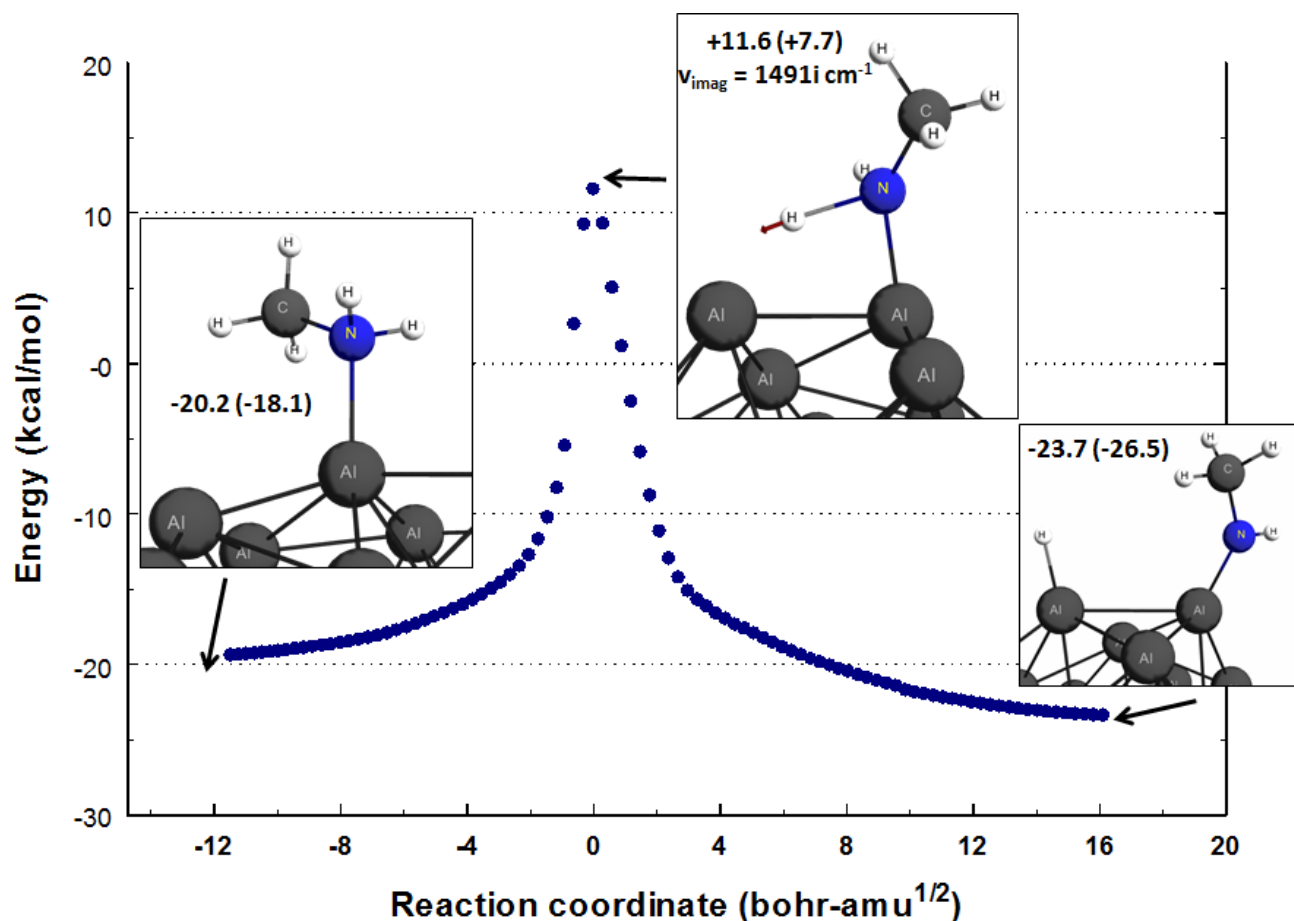


Fig. S31. IRC (blue circles) of chemisorbed CH_3NH_2 undergoing N-H fragmentation to form chemisorbed $\text{CH}_3\text{NH} + \text{H}$, excluding zero point energy (ZPE) corrections. The energies (in kcal mol⁻¹) of the stationary points (reactant, saddle point, and product) are relative to separated $\text{CH}_3\text{NH}_2 + \text{Al}_{80}$. ZPE-corrected energies are given in parentheses. A portion of the Al_{80} substrate has been cropped to show the chemisorbed fragments in greater detail.

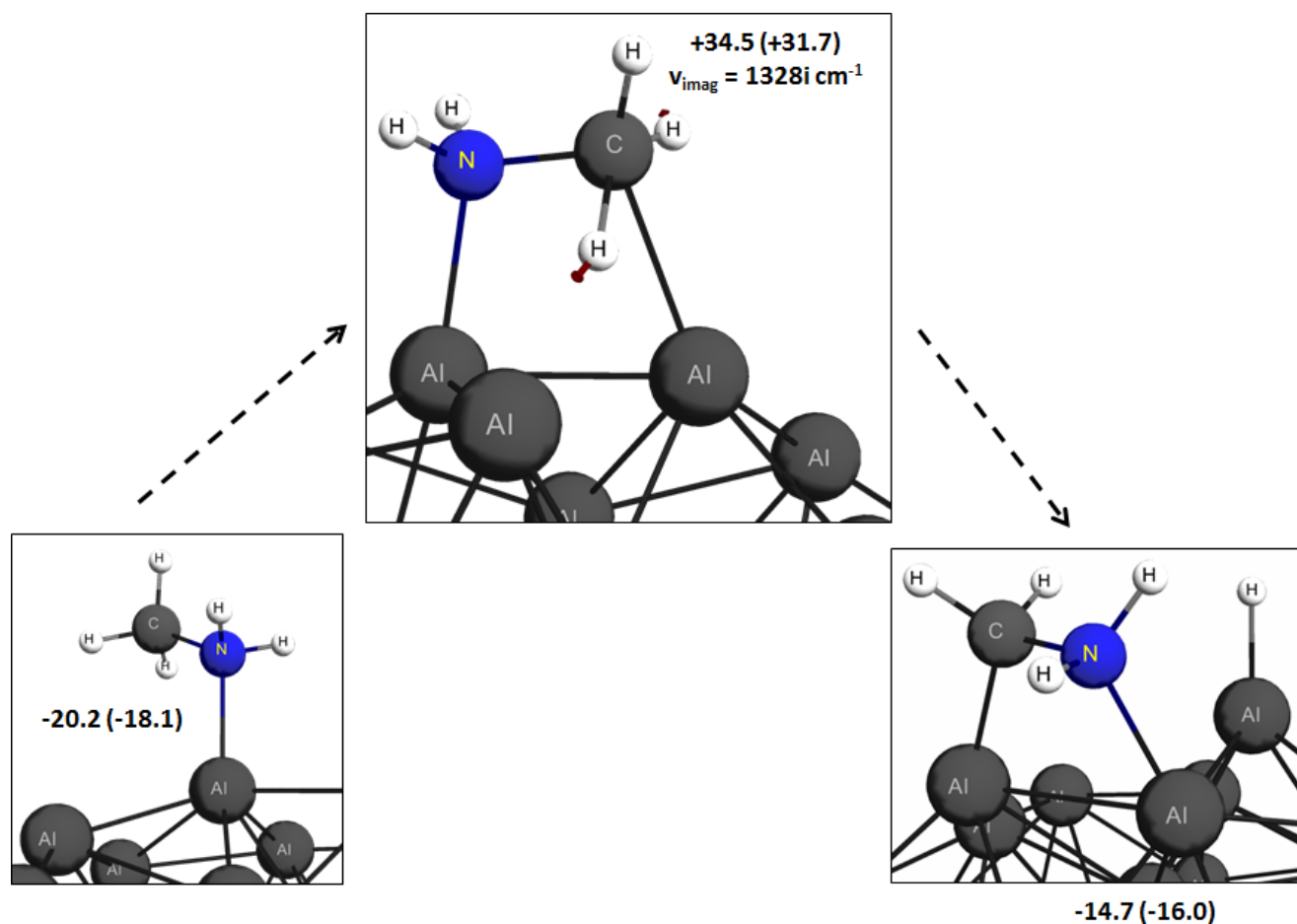


Fig. S32. Transition state and presumed reactants and products for C-H fragmentation in chemisorbed MMA. The energies (in kcal mol⁻¹) of the stationary points (reactant, saddle point, and product) are relative to separated MMA + Al₈₀. ZPE-corrected energies are given in parentheses. A portion of the Al₈₀ substrate has been cropped to show the chemisorbed fragments in greater detail.

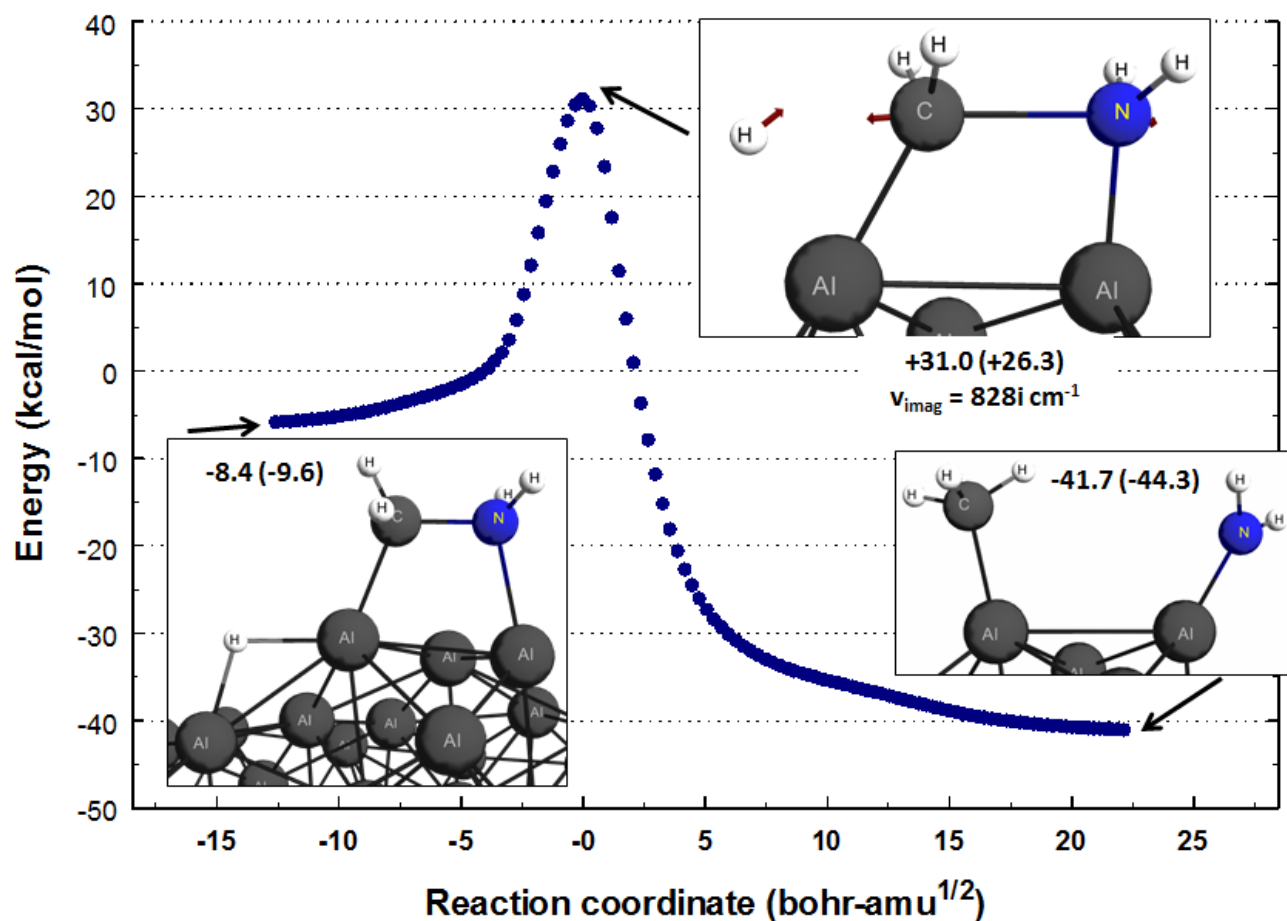


Fig. S33. IRC (blue circles) of chemisorbed H and (CH₂NH₂) undergoing concerted C-H recombination and C-N scission to form chemisorbed CH₃ + NH₂, excluding zero point energy (ZPE) corrections. The energies (in kcal mol⁻¹) of the stationary points (reactant, saddle point, and product) are relative to separated CH₃NH₂ + Al₈₀. ZPE-corrected energies are given in parentheses. A portion of the Al₈₀ substrate has been cropped to show the chemisorbed fragments in greater detail.

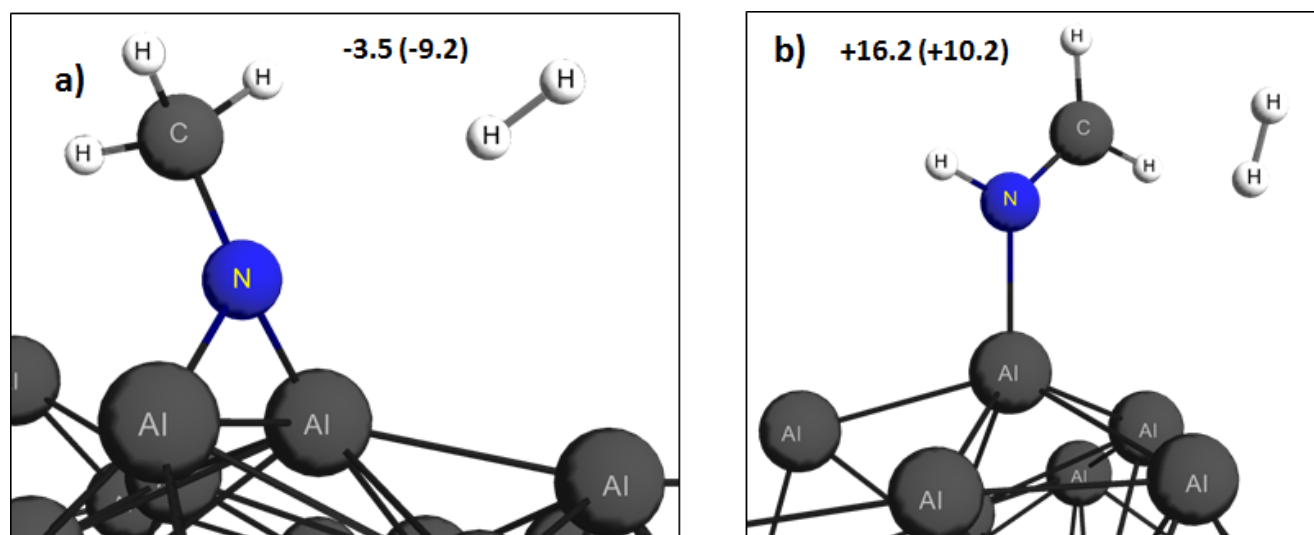


Fig. S34. DFT optimized structures of $\text{CH}_3\text{N}-\text{Al}_{80} + \text{H}_2$ (panel a) and $\text{CH}_2=\text{NH}-\text{Al}_{80} + \text{H}_2$ (panel b.) Energies (in kcal mol^{-1}) are relative to separated $\text{CH}_3\text{NH}_2 + \text{Al}_{80}$. ZPE-corrected energies are given in parentheses. A portion of the Al_{80} substrate has been cropped to show the chemisorbed fragments in greater detail.

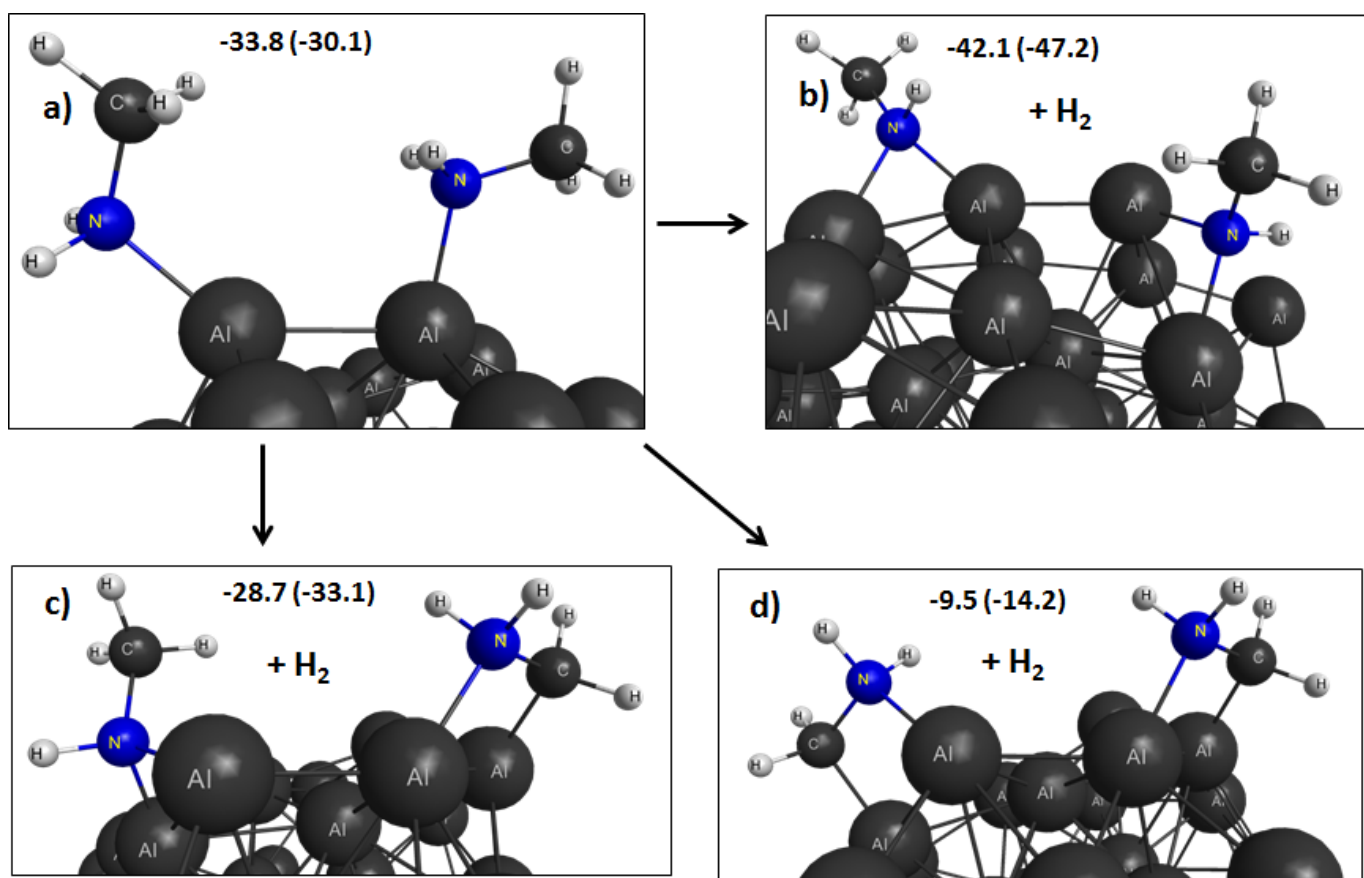


Fig. S35. DFT optimized structures of $\text{CH}_3\text{NH}_2:\text{Al}_{80}:\text{NH}_2\text{CH}_3$ (panel a,) $\text{CH}_3\text{NH}-\text{Al}_{80}-\text{NHCH}_3$ (panel b,) $\text{CH}_3\text{NH}-\text{Al}_{80}-(\text{NH}_2\text{CH}_2)$ (panel c,) and $(\text{CH}_2\text{NH}_2)-\text{Al}_{80}-(\text{NH}_2\text{CH}_2)$ (panel d.) Energies (in kcal mol^{-1}) are relative to separated $2\text{CH}_3\text{NH}_2 + \text{Al}_{80}$. ZPE-corrected energies are given in parentheses. A portion of the Al_{80} substrate has been cropped to show the chemisorbed fragments in greater detail.

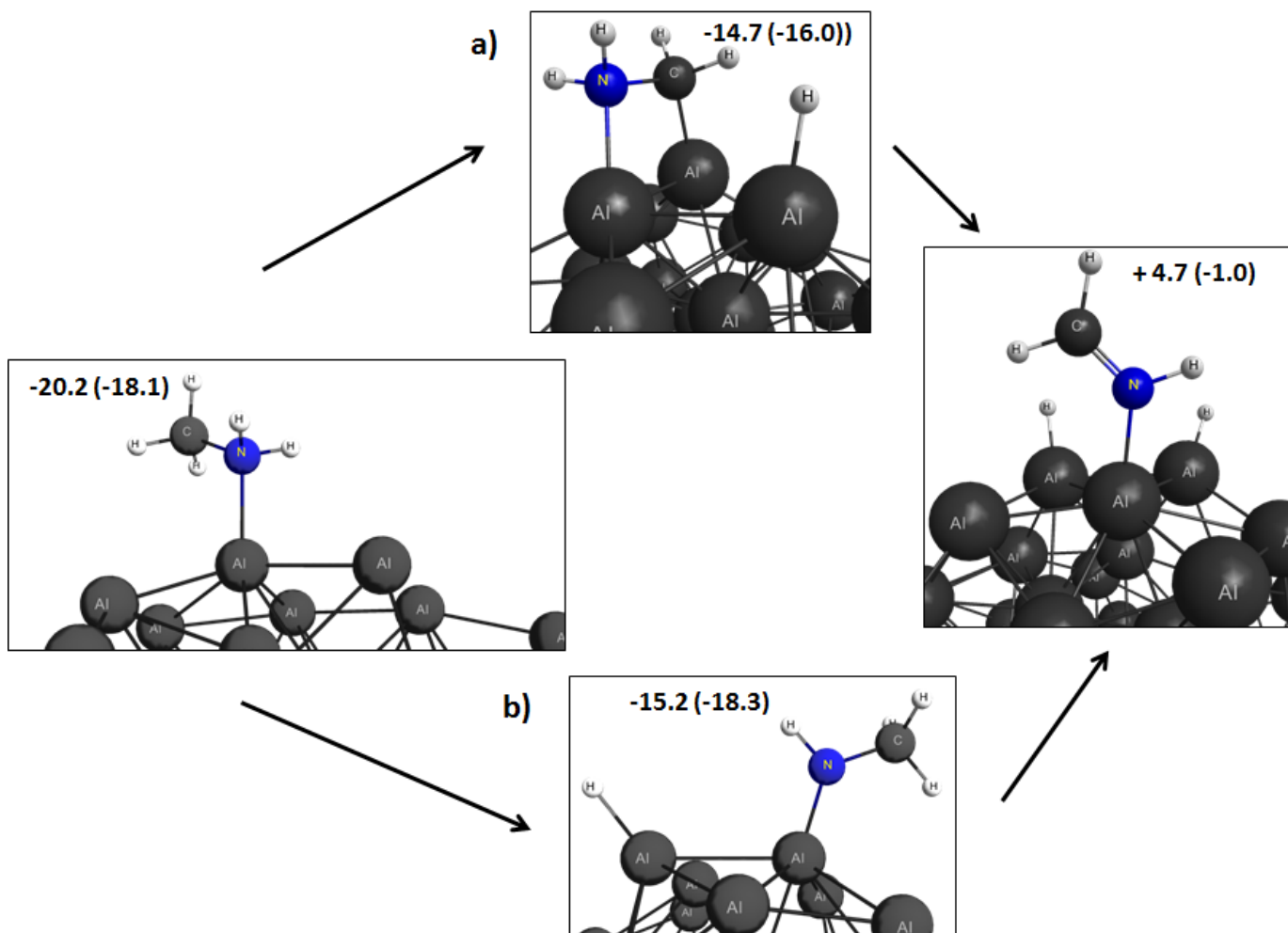


Fig. S36. DFT optimized structures of $\text{CH}_3\text{NH}_2:\text{Al}_{80} \rightarrow (\text{CH}_2\text{NH}_2)\text{Al}_{80}\text{-H} \rightarrow \text{CH}_2=\text{NH}:\text{Al}_{80}\text{-2H}$ (panel a) and $\text{CH}_3\text{NH}_2:\text{Al}_{80} \rightarrow \text{CH}_3\text{NH-Al}_{80}\text{-H} \rightarrow \text{CH}_2=\text{NH}:\text{Al}_{80}\text{-2H}$ (panel b.) Energies (in kcal mol^{-1}) are relative to separated $\text{CH}_3\text{NH}_2 + \text{Al}_{80}$. ZPE-corrected energies are given in parentheses. A portion of the Al_{80} substrate has been cropped to show the chemisorbed fragments in greater detail.

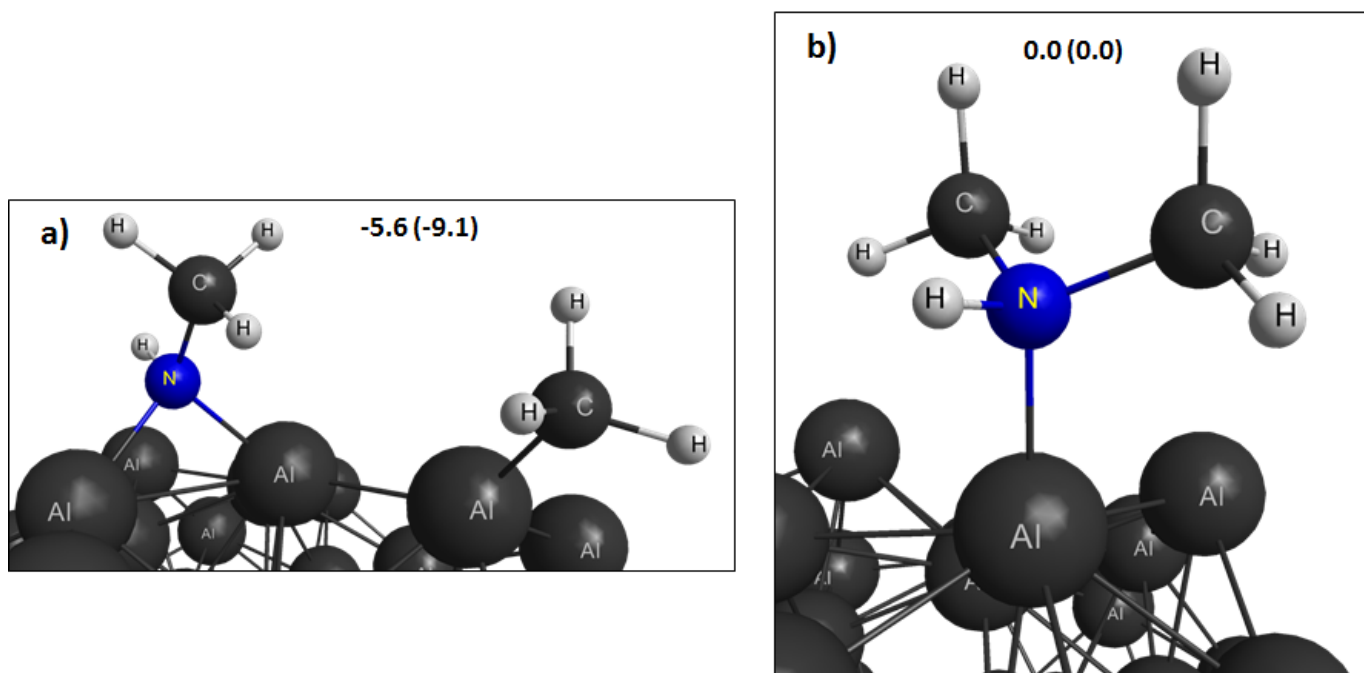


Fig. S37. DFT optimized structures of $\text{CH}_3\text{NH}-\text{Al}_{80}-\text{CH}_3$ (panel a) and $\text{DMA}:\text{Al}_{80}$ (panel b.) Energies (in kcal mol^{-1}) are relative to $\text{DMA}:\text{Al}_{80}$. ZPE-corrected energies are given in parentheses. A portion of the Al_{80} substrate has been cropped to show the chemisorbed fragments in greater detail.

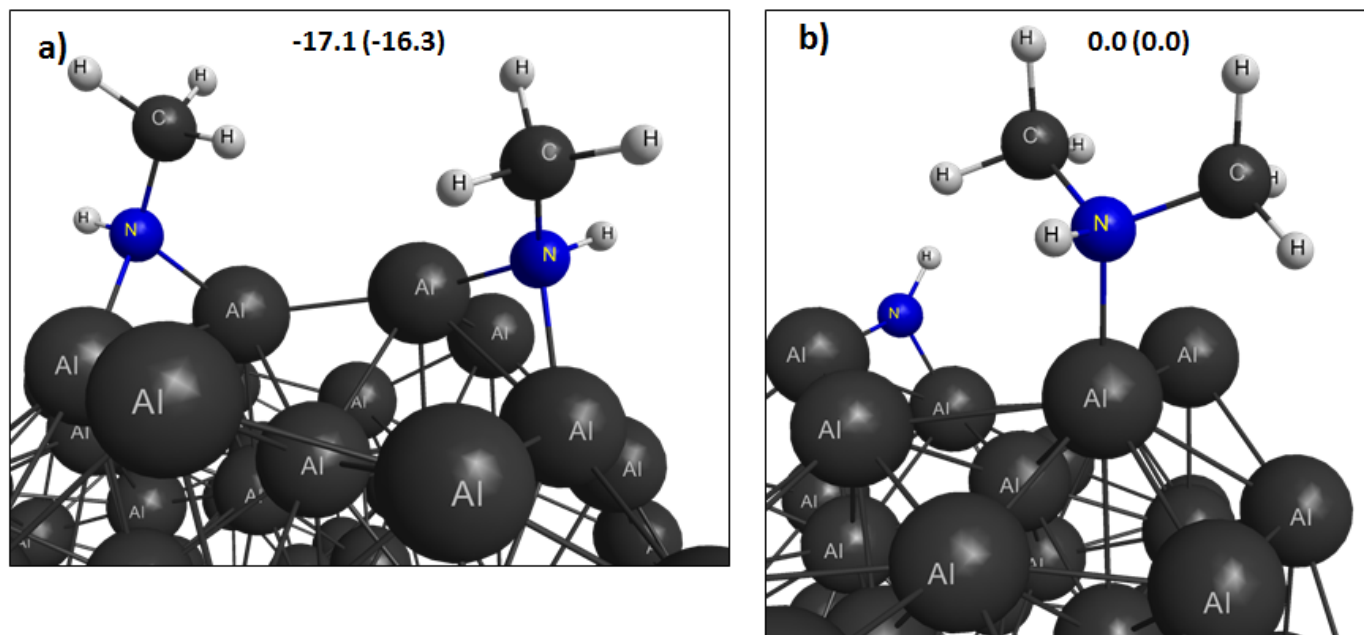


Fig. S38. DFT optimized structures of $\text{CH}_3\text{NH}-\text{Al}_{80}-\text{NHCH}_3$ (panel a) and $\text{DMA}:\text{Al}_{80}-\text{NH}$ (panel b.) Energies (in kcal mol $^{-1}$) are relative to $\text{DMA}:\text{Al}_{80}-\text{NH}$. ZPE-corrected energies are given in parentheses. A portion of the Al_{80} substrate has been cropped to show the chemisorbed fragments in greater detail.

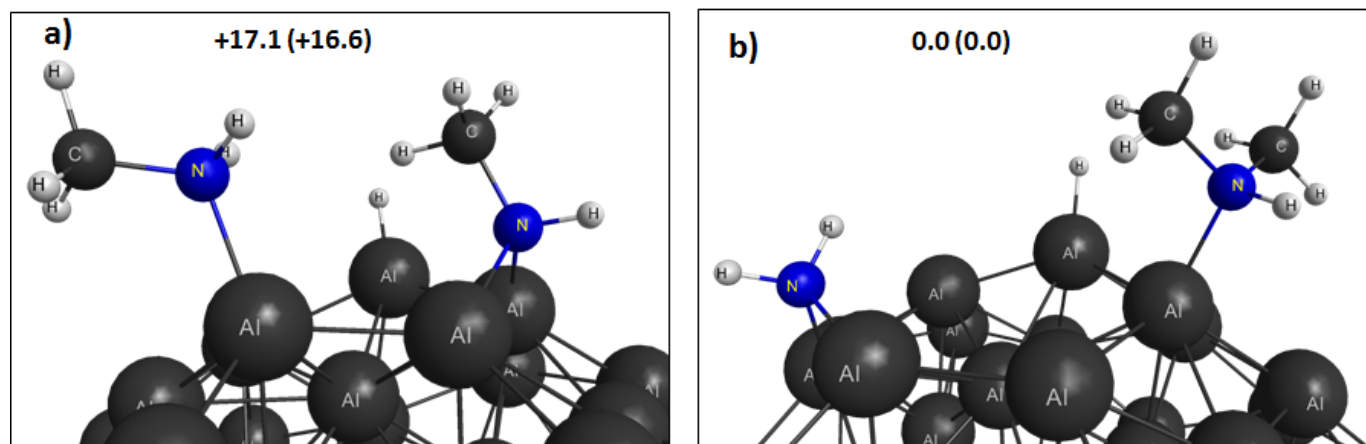


Fig. S39. DFT optimized structures of $\text{H-CH}_3\text{NH-Al}_{80}\text{:NH}_2\text{CH}_3$ (panel a) and $\text{H-DMA:Al}_{80}\text{-NH}_2$ (panel b.) Energies (in kcal mol⁻¹) are relative to $\text{H-DMA:Al}_{80}\text{-NH}_2$. ZPE-corrected energies are given in parentheses. A portion of the Al_{80} substrate has been cropped to show the chemisorbed fragments in greater detail.

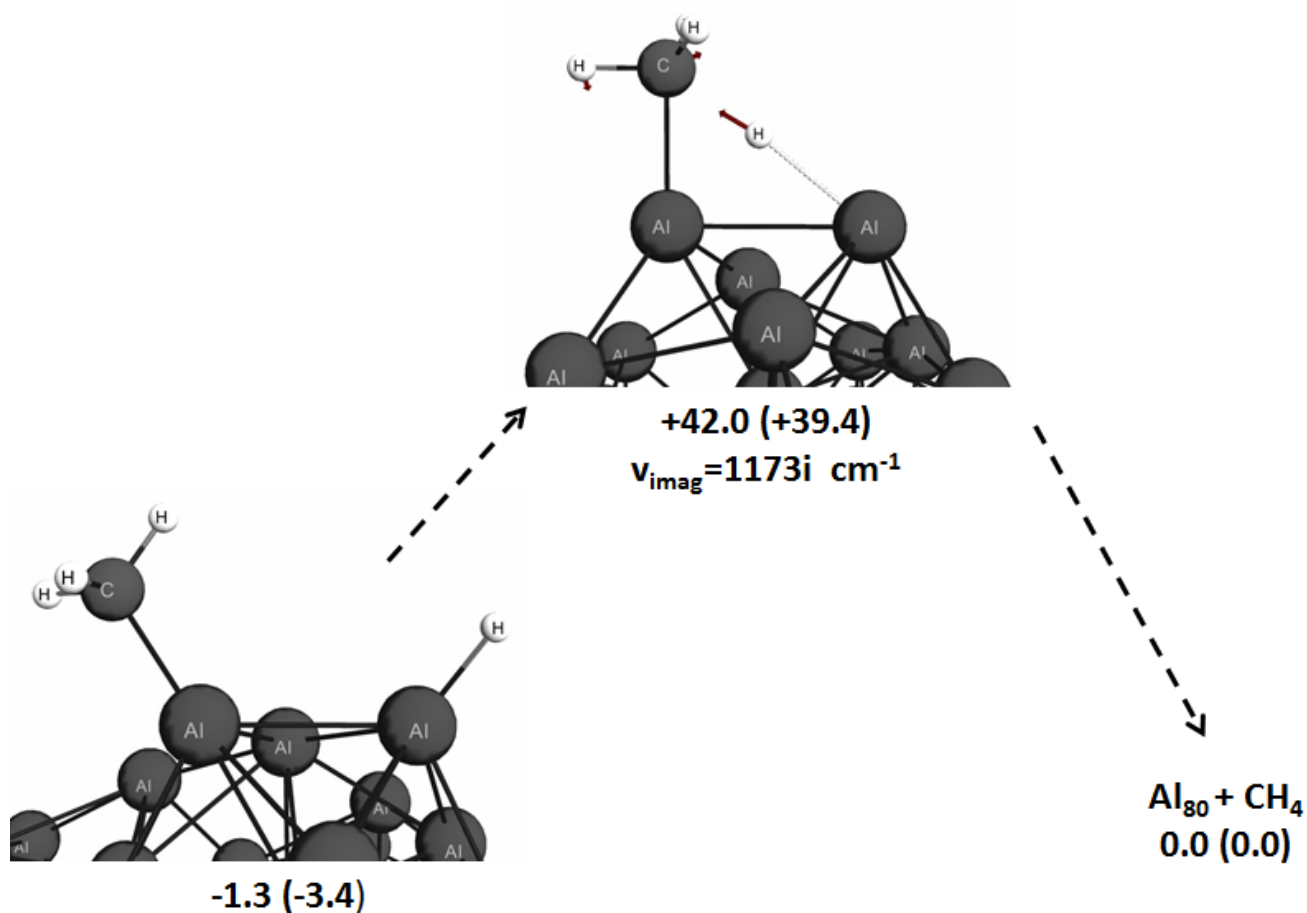


Fig. S40. Transition state and presumed reactants and products for recombination of chemisorbed H and CH₃ to form methane. The energies of the stationary points (reactant, saddle point, and product) are relative to separated CH₄ + Al₈₀. ZPE-corrected energies are given in parentheses. A portion of the Al₈₀ substrate has been cropped to show the chemisorbed fragments in greater detail.

(1) Moulder, J. F.; Stickle, W. F.; Sobol, P. E.; Bomben, K. D., *Handbook of X-Ray Photoelectron Spectroscopy*. Perkin-Elmer Corporation Eden Prairie, 1992; p 261.

(2) Miller, D. J.; Biesinger, M. C.; McIntyre, N. S., Interactions of Co₂ and Co at Fractional Atmosphere Pressures with Iron and Iron Oxide Surfaces: One Possible Mechanism for Surface Contamination? *Surface and Interface Analysis* **2002**, 33, 299-305.

(3) Yates, J. T., Surface Chemistry at Metallic Step Defect Sites. *Journal of Vacuum Science & Technology A: Vacuum, Surfaces, and Films* **1995**, 13, 1359.